Martine Furnes Pettersen

Effect of a Non-Ideal Power Take-Off System on the Electrical Power Output of a Wave Energy Converter under Passive Control

Master's thesis in Energy and Environmental Engineering

June 2020

NTNU
Norwegian University of
Science and Technology

Martine Furnes Pettersen

Effect of a Non-Ideal Power Take-Off System on the Electrical Power Output of a Wave Energy Converter under Passive Control

NTNU

Norwegian University of
Science and Technology

Abstract

Real ocean waves are non-stationary by nature, which gives a challenge when designing and controlling wave energy converters (WECs). Many different control strategies have been proposed to increase the energy absorption of WECs under a variety of operating conditions. The performance of these control schemes have been verified through the use of hydrodynamic models, with the assumption that the power take-off (PTO) system is ideal. Generally, the PTO system can either be tuned on a constant frequency characterized by a local spectrum or continuously tuned after the wave frequency. Recent studies with a passive control (PC) method based on the Hilbert-Huang transform (HHT), that tunes the PTO on a wave-by-wave basis, have shown promising results with an ideal PTO for increasing the energy absorption from the waves. In this thesis, these studies have been extended to include a fully-coupled wave-to-wire model that includes the physical limitations and efficiency of an electrical PTO system. Through numerical simulations and comparisons with a passive loading (PL) method tuned at the mean centroid frequency of the excitation force spectrum and the case when only the hydrodynamic model is considered, the effect of the PC strategy on the electrical power output of the WEC is studied. Simulations with the hydrodynamic model only showed that the PC scheme absorbs more energy from the waves than PL. For instance, for sea states characterized by a wideband spectra, PC obtained a performance improvement in the absorbed energy of up to 32% compared to PL. From the wave-to-wire results, it was observed that PC averagely generates 10% more electrical power than PL, supporting the results with an ideal PTO. However, PC also requires 84% more power from the grid compared to PL in order to operate correctly. Even though PL results in more average power losses than PC, PL still averagely give around 6% more electrical power output than PC. This shows that the physical limitations and non-linearity of the PTO reduces the benefit of a time-varying PTO damping.

Sammendrag

Fysiske havbølger er ikke-stasjonære av natur, noe som gir en utfordring når en bølgeomformer skal konstrueres og kontrolleres. Gjennom tidene er det foreslått mange forskjellige kontrollstrategier for å kunne øke mengden energi som absorberes av bølgeomformeren under ulike driftsforhold. Ytelsen til disse kontrollmetodene er bekreftet ved bruk av hydrodynamiske modeller, hvor ideelle elektriske kraftuttakssystemer (PTO) er antatt. Generelt kan de elektriske kraftuttakssystemene justeres enten etter en konstant frekvens karakterisert av et lokalt spektrum eller etter en kontinuerlig frekvens som følger bølgefrekvensen. Nyere studier med en passiv kontroll (PC) metode basert på Hilbert-Huang transform (HHT), som justerer PTO systemet fra bølge til bølge, har vist lovende resultater med en ideell PTO for å kunne øke mengden absorbert energi fra bølgene. I denne masteroppgaven har disse studiene blitt utvidet til å omfatte en modell som inkluderer de fysiske begrensningene og effektiviteten til det elektriske PTO systemet. Gjennom numeriske simuleringer og sammenligninger med en passiv belastningsmetode (PL) som bruker den gjennomsnittlige spektralsentroiden av energispekteret til kraften av den innkommende bølgen og tilfellet når bare den hydrodynamiske modellen er vurdert, blir effekten PC metoden har på mengden elektrisk generert effekt til bølgeomformeren studert. Simuleringene med kun den hydrodynamiske modellen viser at PC strategien absorberer mer energi fra bølgene enn PL. Ett eksempel er, for havtilstander karakterisert med et bredt frekvensspekter, oppnådde PC en ytelsesforbedring i den absorberte energien på opptil 32% sammenlignet med PL. Fra resultatene med modellen av bølgeomformeren med en ikke-ideell PTO, ble det observert at PC genererer i gjennomsnitt 10% mer elektrisk effekt enn PL, noe som støtter resultatene med en ideell PTO. Derimot krever PC 84% mer effekt fra nettet, sammenlignet med PL, for å kunne operere korrekt. Selv om PL resulterer i høyere gjennomsnittlige effekttap enn PC, vil PL i gjennomsnitt gi ut ca. 6% mer elektrisk effekt enn PC. Dette viser at de fysiske begrensningene og ikke-linearitetene til PTO systemet reduserer fordelen med en tidsvarierende PTO dempning.

Preface

The work on my thesis has been a semester full of many emotions and memories. There have been frustration when the simulation results do not make sense and happiness when the results finally makes sense. In March of 2020, covid-19 shut down Norway bringing on sadness because I had to leave NTNU and my fellow classmates, and the challenges of working from home. My time working with my thesis has tested my concentration, knowledge and patience, and I have learned a lot from it. It has been a very different time for all, which hopefully have made us appreciate the possibility of moving freely around more.

Table of contents

List of Tables

x

List of Figures

Nomenclature

Abbreviations

EKF	Extended Kalman filter
EMD	Empirical Mode Decomposition
HHT	Hilbert-Huang transform
HT	Hilbert transform
IMF	Intrinsic Mode Function
KF	Kalman filter
MMF	Magnetomotive force
OWC	Oscillating Water Column
PC	Passive control
PL	Passive loading
PTO	Power take-off
PWM	Pulse-Width Modulation
$SMPMSM$	Surface-Mounted Permanent Magnet Synchronous Machine
WEC	Wave Energy Converter

Variables

$\bar{P}_a(t)$	Average absorbed power [W]
$\bar{P}_e(t)$	Average electrical power [W]
$\bar{P}_l$	Average power loss [W]
$\ddot{x}(t)$	Acceleration of the WEC [m/s^2]
$\dot{x}(t)$	Velocity of the WEC [m/s]
$\dot{x}_{max}(t)$	PTO maximum speed [m/s]
Γ	Gamma function
$\hat{\omega}_d$	Instantaneous frequency of the dominant IMF component [rad/s]
$\hat{a}_d(t)$	Instantaneous amplitude of the dominant IMF component [N]

λ	Spectral shape parameter
ω	frequency [rad/s]
$\omega_{1,fe}$	Mean centroid frequency of the excitation force spectrum [rad/s]
ω_1	Mean centroid frequency [rad/s]
ω_{max}	Maximum generator speed [rpm]
ω_{mech}	Mechanical speed of the WEC [rad/s]
ω_m	Modal or peak frequency [rad/s]
ω_n	Angular frequency [rad/s]
ω_{rm}	Field weakening speed [rad/s]
ω_r	Rotor angular speed of the generator [rad/s]
ϕ_n	Phase shift [rad/s]
Ψ_{PM}	Flux linkage of the permanent magnets [Wb]
ρ_g	Angular to linear gear ratio [1/m]
$\zeta(t)$	Wave elevation [m]
$B_p(t)$	PTO damping [kg/s]
$B_r(\omega)$	Radiation damping [kg/s]
$c_d(t)$	Dominant IMF component
$c_i(t)$	i-th IMF component
$d\omega$	Step between the spectral frequencies
$E_{c_i}(t)$	Energy in each IMF component [W]
$f_e(t)$	Excitation force [N]
$f_p(t)$	Machinery or PTO force [N]
$f_r(t)$	Radiation force [N]
$f_s(t)$	Hydrostatic force [N]
$H_e(\omega)$	Excitation force transfer function
$h_e(t)$	Inverse Fourier transform of the excitation force transfer function
$h_o(s)$	Open loop transfer function
$h_r(t-\tau)$	Fluid memory term
H_s	Significant wave height [m]
$i_{d,ref}$	Reference d-axis current [A]
i_{dc}	center d-axis coordinate of the voltage limit circle [A]
i_d	Stator d-axis current [A]

I_{max}	DC-bus current [A]
$I_{q,max}$	Maximum q-axis current [A]
$I_{q,min}$	Minimum q-axis current [A]
$i_{q,ref}$	Reference q-axis current [A]
i_{qc}	center q-axis coordinate of the voltage limit circle [A]
i_q	Stator q-axis current [A]
K_p	PI-controller gain
L_{leak}	Leakage inductance [H]
L_m	Magnetizing inductance [H]
L_s	Synchronous or stator inductance [H]
m	Body mass [kg]
$M(s)$	Closed loop transfer function
m_n	Spectral moments
$m_r(\infty)$	Added mass coefficient at infinite frequency [kg]
n_p	Number of poles
P	Cauchy principal value
$P_a(t)$	Absorbed power [W]
$P_e(t)$	Instantaneous electrical power [W]
P_l	Power loss [W]
$P_{mech}(t)$	Instantaneous mechanical power [W]
R_s	Stator resistance [Ω]
S	Hydrostatic stiffness [N/m]
$S(\omega)$	Spectral density
T	time interval [s]
t	time [s]
T_{delay}	Time delay caused by the converter bridge [s]
$T_{e,ref}$	Reference torque [Nm]
T_e	Generator torque [Nm]
T_i	Time constant in the PI-controller [s]
u_d	Stator d-axis voltage [V]
U_{max}	DC-link or DC-bus voltage [V]
u_q	Stator q-axis voltage [V]

$v_{d,ref}$	Reference d-axis voltage [V]
$v_{q,ref}$	Reference q-axis voltage [V]
$x(t)$	Displacement of the WEC [m]

$v_{d,ref}$ Reference d-axis voltage [V]

Chapter 1

Introduction

The world is currently experiencing a climate crisis which has resulted in a growing interest in renewable energy. Over the last couple of years, the energy potential located offshore has received an increased amount of focus with offshore wind turbines in the lead. This has also resulted in a regained commercial interest in wave energy [1]. The wave energy resource has been estimated to be between 8 000 and 80 000 TWh in total worldwide [2]. Once existing wave energy converters (WECs) reach maturity, it is estimated that around 140-750 TWh can be commercially exploitable annually [3]. Furthermore, if all potential technology is realized, studies have shown that the total energy production can be as high as 2 000 TWh per year [4]. In comparison, the total energy production in 2018 was 23 031 TWh, where wind generated 1 265 TWh and hydro 4 303 TWh [5]. Potentially, wave energy can contribute with approximately 10% of the global electricity consumption.

The complexity of generating electrical power from waves has led to a numerous of different designs. Some of the most common working principles are: oscillating water column (OWC), oscillating body, and overtopping devices. These principles are defined following the first step of the energy conversion process, where the wave energy is either converted into air pressure (OWC), mechanical energy (oscillating body devices), or potential energy (overtopping devices). In this thesis, a point absorber is studied, which is classified as an oscillating body device.

The system converting the mechanical energy into electrical energy is called the power take-off (PTO) system. The performance objective of the PTO system is to maximize the energy absorption from the waves. To do this, different control strategies are implemented in the WEC. Various control algorithms have been proposed. A review of available control strategies can be found in [6]. In this thesis, the applied control method consists of tuning the PTO damping only, which can be referred to as passive control. Reactive control is another control scheme that tunes the PTO damping, but it also adjusts the stiffness of the system.

When tuning the PTO damping, knowledge of the incoming waves are usually required in order to find the optimal tuning frequency. For sinusoidal waves characterized by a single frequency, i.e., regular waves, the tuning frequency can easily be found. However, real ocean waves are non-stationary by nature. As a result, the tuning frequency is more challenging to define, and is, in general, either chosen to be a constant frequency representing the local wave spectrum or time-varying.

Theoretically, reactive control is the preferable control method as it manipulates the WEC into resonance, allowing the theoretical maximum power to be reached in irregular waves [7]. However, non-ideal efficiencies of PTO systems might limit the potential for increased power production by reactive control [8, 9, 10].

On the other hand, recent studies have shown that by using time-frequency estimations obtained from the Hilbert-Huang transform (HHT) to tune the PTO damping, the absorbed power from the waves is greater than by tuning the PTO to a constant frequency of the wave spectrum [11], or to time-frequency estimations from the Extended Kalman Filter or frequency-locked loop [12]. These studies [11, 12] have only focused on the hydrodynamic model, assuming a generic and ideal PTO system, where the performance of the WEC under passive and reactive control is measured in terms of the absorbed power and PTO rating. A non-ideal PTO system have not yet been considered for control schemes based on the HHT method.

1.1 Objective

This thesis investigates the effect a passive control scheme with HHT has on the electric power output of a WEC with a non-ideal PTO system. To do this, the hydrodynamic model of an oscillating cylinder is connected to an all-electric PTO system, like the system of the wave energy converter Lifesaver [10]. Hence, the analysis of the WEC performance under a control system using HHT is extended to include a fully-coupled wave-to-wire model with the physical limitations and efficiency of the PTO system. In [10], Sjolte et al. showed that the electric PTO system of Lifesaver has limited potential for increased power production using reactive control due to the large accumulated average losses and limited efficiency of the generator. Thus, this thesis investigates the potential of another control scheme for Lifesaver in order to increase the electrical power output. To identify the effect of the passive control method with HHT, the results are compared with (1) the results when running the hydrodynamic model only, and (2) the passive loading method when the PTO damping is tuned to a constant frequency. For any practical application study, an on-line estimation of the incident wave frequency is required. Here, the mean centroid frequency of the excitation force spectrum is considered. Simulation results in [12] have indicated that the Extended Kalman Filter is able to estimate this frequency.

A result of this work has been a conference paper "Effect of non-ideal power take-off on the electric output power of a wave energy converter under passive control". This paper has been submitted to the conference: **RENEW2020**, 4th International Conference on Renewable Energies Offshore, 12 - 15 October 2020, Lisbon, Portugal. The paper has preliminary been accepted and the final version is submitted. The notification of final acceptance is scheduled for July 1, 2020. The paper is included in Appendix A.2.

1.2 System description

The WEC considered is a single oscillating point absorber, moving only in a heaving motion. In this thesis, the considered oscillating body is the same vertical cylinder that is adopted in [11]. The oscillating body is connected to an electric PTO system, similar to the PTO system of the wave energy converter Lifesaver [10].

The electric PTO system generates power through a mooring line that is twined around a

winch. The winch is further connected to a gearbox which runs a generator. A conceptual illustration of the PTO system is shown in Figure 1.1. As the body of the WEC moves, the mooring line is either dragged in or out, resulting in a rotational motion of the winch. This is further exploited to generate power by the electrical machine. The electrical machine only operates as a generator, and hence produce power, during the upward motion of the body. When the body has a downward motion, the electrical machine operates as a motor, drawing power from the grid, in order to maintain tension in the mooring line.
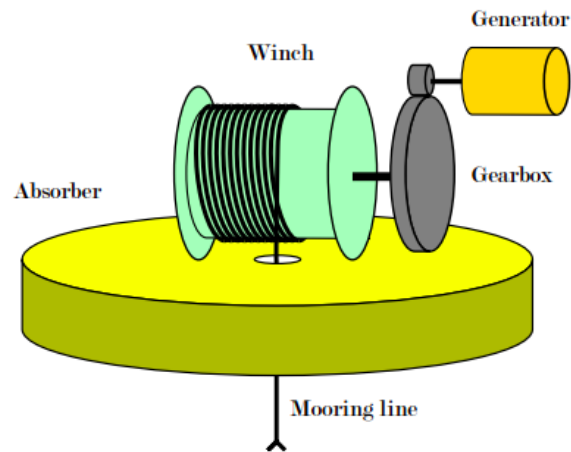
Figure 1.1: The concept behind the PTO of Lifesaver [10]

Chapter 2

Hydrodynamic model

2.1 Modelling of a sea state

Real ocean waves can mathematically be described as an infinite number of sinusoidal waves with different frequencies, amplitudes and phases. When modelling a sea state, an approximation of real ocean waves are generated by combining a large number of sinusoidal waves, referred to as an irregular wave.

A distribution of the total energy, of a given sea state, as a function of frequency can be estimated from the energy of each individual wave making up the irregular wave. This distribution is referred to as the wave spectrum, or energy spectrum of the sea.

Various spectral formulations can be used to characterize a sea state, presented in [13]. The spectra vary from using only one parameter in its formulation ("fully developed sea") to using six parameters (combined sea and swell). In this thesis, the six parameter Ochi-Hubble spectrum is considered.

2.1.1 Ochi-Hubble spectrum

The Ochi-Hubble spectrum is a two set combination of a three-parameter spectrum, where one set primarily contains the lower frequency components of the wave energy (remotely generated swells) and the second set includes the higher frequency components of the wave energy (local wind-generated waves) [14]. It is a double-peak spectra, which typically is used to represent moderate sea conditions. More intense seas are usually represented by a single, sharply peaked three-parameter formulation [13]. The spectral formulation of the Ochi-Hubble spectrum can be expressed as [15]

$$S(\omega) = \frac{1}{4} \sum_{j=1}^{2} \frac{\left[\left(\lambda_j + 0.25 \right) \omega_{m_j} \right]^{\lambda_j}}{\Gamma(\lambda_j)} \frac{H_{s_j}^2}{\omega^{4\lambda_j + 1}} e^{-\frac{\left(\lambda_j + 0.25 \right) \omega_{m_j}^4}{\omega^4}}, \qquad (2.1)$$

where Γ is the gamma function, and the variables from each set is combined. Each set consists of a significant wave height (average of the one-third highest wave) H_{s_j}, a spectral shape parameter λ_j and a modal or peak frequency ω_{m_j}.

In the Ochi-Hubble spectrum, both swells and wind-generated waves are included in the final wave spectrum. Swells are waves created by a storm that can travel long distances with little energy loss. The energy in swells increase with their height, as can be seen in Figure 2.1b. Wind-generated waves are created through an energy transmission between wind and water near the free surface. This means that the longer the local wind blows, the higher low frequency peaks are observed, as shown in Figure 2.1c. The spectral shape parameter λ controls the shape (sharpness) of the spectrum, as illustrated in Figure 2.1a.

(a) Variable λ, $H_s = 5$ and $\omega_m = 0.5$

(b) Variable H_s, $\lambda = 10$ and $\omega_m = 0.5$

(c) Variable ω_m, $\lambda = 10$ and $H_s = 5$
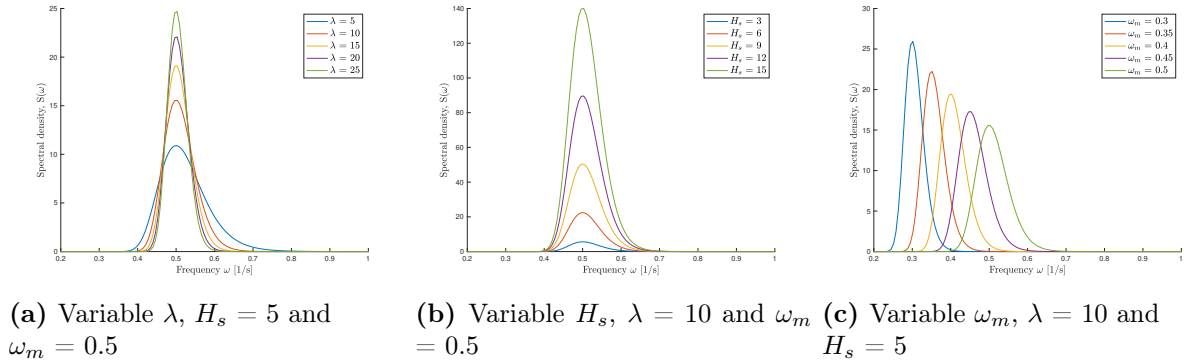
Figure 2.1: Three-parameter spectra with variable spectral shape parameter λ, significant wave height H_s and modal frequency ω_m

2.1.2 Time-series of the wave elevation

Irregular waves can be generated by adding a finite number of sinusoidal waves with different frequencies, amplitudes and random phases. The elevation of each one of the individual waves can be found by [16]

$$\zeta_n(t) = \sqrt{2S_\omega(\omega_n)d\omega}cos(\omega_n(t) + \phi_n) \,, \tag{2.2}$$

where ω_n is the angular frequency, $d\omega$ is the difference between the spectral frequencies, and ϕ_n is the random phase of the n-th wave component. The summation of N independent sinusoidal components (ideally, $N \rightarrow \infty$) results in the total elevation for an irregular wave [16, 17],

$$\zeta(t) = \sum_{n=1}^{N} \sqrt{2S_\omega(\omega_n)d\omega}cos(\omega_n(t) + \phi_n) \,. \tag{2.3}$$

2.2 Forces acting on the WEC

A floating body in a moving fluid will experience forces connected to gravity, buoyancy, incident waves, diffracted waves, generated waves, drag, drift, and currents. A WEC will experience forces from the machinery and mooring as well. For simplicity, the forces related to the drag, drift, currents, and mooring have been neglected in this thesis.

The WEC considered here is a single oscillating point absorber, only moving in a heaving motion, as shown in Figure 2.2.
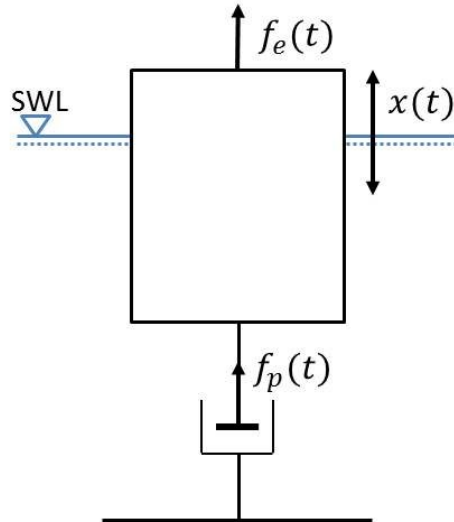
Figure 2.2: Schematic of the oscillating body [11]

Using Newton's second law of motion, the force balance of the WEC can be expressed as

$$m\ddot{x}(t) = f_e(t) + f_r(t) + f_s(t) + f_p(t)\,, \tag{2.4}$$

where m is the mass of the WEC, $\ddot{x}(t)$ is the body acceleration, $f_e(t)$ is the excitation force, $f_r(t)$ is the radiation force, $f_s(t)$ is the hydrostatic force, and $f_p(t)$ is the machinery or PTO force. Here, linear hydrodynamic theory is assumed.

2.2.1 Excitation force

The excitation force is the force acting on the body when it is held fixed in undisturbed incident waves. In the time domain, the excitation force can be expressed as

$$f_e(t) = \int_{-\infty}^{\infty} h_e(t - \tau)\zeta(\tau)d\tau\,, \tag{2.5}$$

where

$$h_e(t) = \frac{1}{2\pi} \int_{-\infty}^{\infty} H_e(\omega)e^{i\omega t}d\omega \tag{2.6}$$

is the inverse Fourier transform of the excitation force transfer function $H_e(\omega)$, which is characteristic for each WEC.

Generally, the excitation force is defined to be non-causal [18]. This means that the system output depends on future inputs, which physically is explained through the fact that the force is caused by the pressure distribution from the incident waves, and not by the actual incoming waves hitting the body [18].

2.2.2 Radiation force

The radiation force is the force due to waves generated by the motion of the body itself. Cummins [19] showed that the radiation force in the time domain can be expressed as

$$-f_r(t) = m_r(\infty)\ddot{x} + \int_0^t h_r(t-\tau)\dot{x}(\tau)\,d\tau\,, \qquad (2.7)$$

where $m_r(\infty)$ is the added mass coefficient for the floating body at infinite frequency and $h_r(t-\tau)$ is the integration kernel know as the fluid memory term [20], given by

$$h_r(t-\tau) = \frac{2}{\pi}\int_0^\infty B_r(\omega)\cos(\omega(t-\tau))d\omega\,, \qquad (2.8)$$

where $B_r(\omega)$ is the radiation damping. The memory term represents how previously generated waves still affect the fluid pressure, and hence the radiation force, for all subsequent times [20].

2.2.3 Machinery force

The machinery force, or PTO force, is the force applied to the system by the PTO, including friction. Here, the machinery force is defined as

$$f_p(t) = -B_p(t)\dot{x}(t), \qquad (2.9)$$

where $\dot{x}(t)$ is the velocity of the WEC and $B_p \in \mathbb{R}_+$ represents the PTO damping. The magnitude of the PTO force, and how it is applied, influences the WEC's capability to extract power from the incident waves. This will further be explained in Chapter 4.

2.2.4 Hydrostatic force

The hydrostatic force is related to the change in the hydrostatic pressure on the surface of the WEC as it moves from its equilibrium position [21]. As a result, the hydrostatic force becomes a function of the displacement of the device $x(t)$. Commonly, the hydrostatic stiffness S is considered to be constant since the displacement of the WEC from equilibrium is assumed to be small [22]. Hence, the hydrostatic force can be found by

$$f_s = -Sx(t)\,. \qquad (2.10)$$

2.3 Absorbed power

The absorbed power is defined as the power the WEC is able to extract from the incoming waves. As previously mentioned, the absorbed power depends on the PTO force, where the instantaneous absorbed power can be expressed as

$$P_a(t) = -f_p(t)\dot{x}(t)\,. \qquad (2.11)$$

The average absorbed power can hence be found for a time interval T as

$$\bar{P}_a(t) = -\frac{1}{T} \int_0^T f_p(t)\dot{x}(t)dt \,. \qquad (2.12)$$

2.4 Electrical analogy

For readers with a background in electrical circuits, the oscillating system can easier be understood in comparison with a RLC circuit [18]. The electric circuit is outlined on the basis of equation (2.4). The excitation force is represented by the voltage source, making the current analogous to the velocity of the WEC. Further, the machinery force is represented by the load voltage. From equation (2.9), the PTO damping becomes analogous to the load resistance. Thus, the radiation damping also becomes analogous to a resistance. Circuit theory defines the inductance as the tendency for an inductor to oppose a change in the current flowing through it, and capacitance as a capacitors ability to store electric charge. Relating these definitions to the mechanical system, the inductor can be seen analogous to the kinetic energy of the WEC while the capacitor is analogous to the potential energy of the WEC. The inductance can thus be related to the body mass and added mass at infinite frequency and the capacitance to the hydrostatic stiffness.
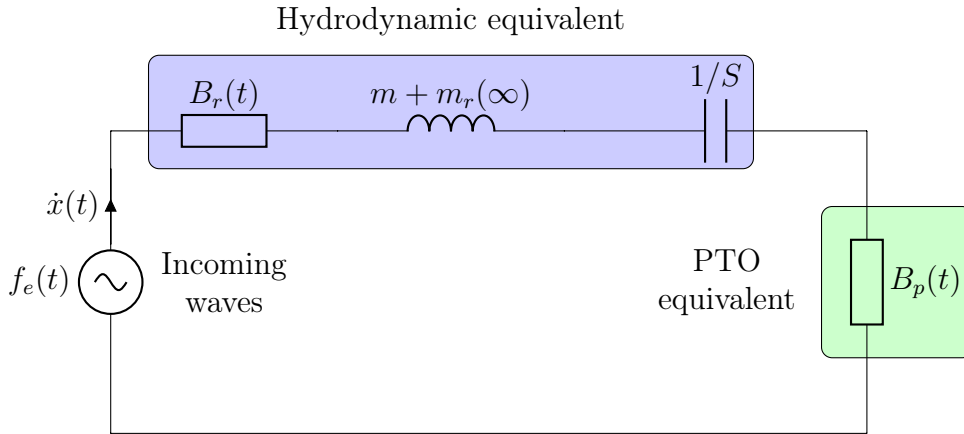
Figure 2.3: Equivalent circuit of the WEC

Applying Kirchhoffs law on the resulting electric circuit, shown in Figure 2.3, results in the following equation

$$f_e(t) = \ddot{x}(t)(m + m_r(\infty)) + \int_0^t h_r(t - \tau)\dot{x}(\tau)\,d\tau + Sx(t) + B_p\dot{x}(t) \,. \qquad (2.13)$$

Inserting all the defined expressions into the force balance in equation (2.4), the outcome will be equal to equation (2.13).

Chapter 3

Electric PTO system

The electric PTO system studied in this thesis is a mechanical system consisting of a winch, gearbox and electrical machine, as explained in Section 1.2. Electrical power is generated through the rotational motion of the winch caused by the heaving motion of the WEC. The gearbox gives flexibility to be able to utilize the speed capability of the generator. To optimize the energy absorption and not exceed the defined PTO specifications, a control system with current control and torque control is implemented. In this thesis, the PTO system is assumed to be connected to a stiff DC-link only, omitting the grid connected system and its challenges.

3.1 Linear reference frame

The purpose of the PTO system is to convert the linear motion of the oscillating body into electrical power. In this way, the PTO operates both in a linear and rotational motion, where the reference frame is selected to be linear [23]. The angular to linear gear ratio ρ_g is therefore introduced to describe the relationship between the linear motion of the WEC and the rotational motion of the generator,

$$\omega_{mech}(t) = \rho_g \dot{x}(t) \,. \tag{3.1}$$

This is further explained in [23].

3.2 Surface-Mounted Permanent Magnet Synchronous Machine

The electrical machine used in this WEC is a Surface-Mounted Permanent Magnet Synchronous Machine (SMPMSM). Compared to an induction machine, the PMSM has higher torque to inertia ratio, higher efficiency, more compact design, and higher power density, which has made the PMSM more preferable to use in several renewable energy technologies as wind power, wave power, and tidal power [24]. The induction machine has, on the other hand, a lower cost than the PMSM.

The advantage with PMSMs is that they do not need to magnetize the rotor externally, through either a magnetizing current in the stator or by directly magnetizing the rotor,

which results in no copper losses associated with the rotor and reduces the size of the machine [25]. In a SMPMSM, the rotor field is excited by the permanent magnets that are placed on the outside of the rotor. An illustration of a 4-pole SMPMSM is shown in Figure 3.1.
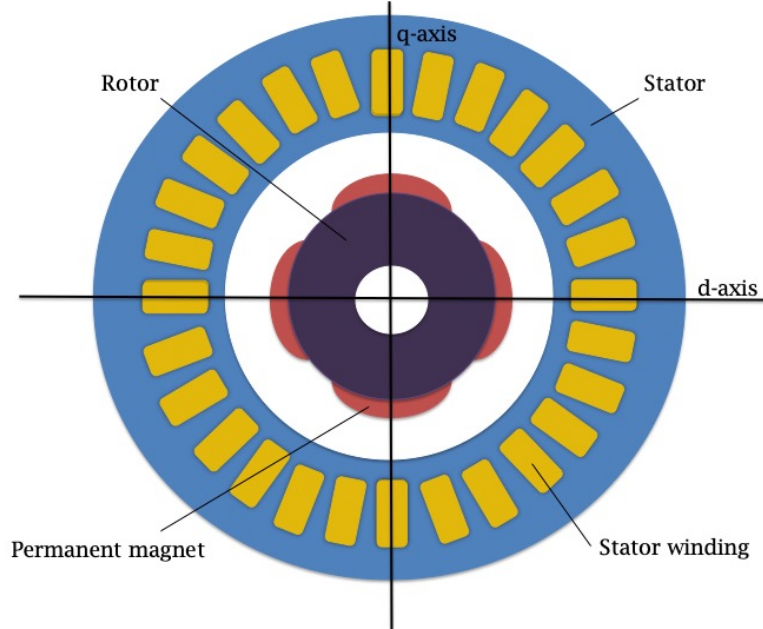
Figure 3.1: Illustration of a 4-pole SMPMSM

For dynamic analysis and control of AC machines, it is necessary to operate with two orthogonal windings (d- and q-windings) so that the torque and flux within the machine can be controlled independently [26]. In a synchronous machine, it is important that the new reference frame has the same electrical angular velocity as the rotor, hence the dq-reference frame is fixed to the rotor. The d-axis will then always be aligned with the rotor magnetic axis with the q-axis 90°ahead in the direction of the rotation (assumed to be counter-clockwise) [26], as illustrated in Figure 3.1. The equivalent circuit of the SMPMSM in the dq-reference frame is shown in Figures 3.2 and 3.3.
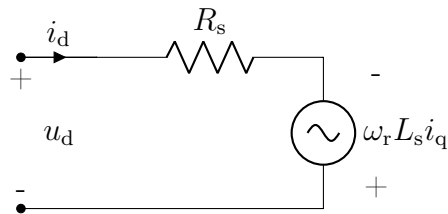
Figure 3.2: D-axis equivalent circuit
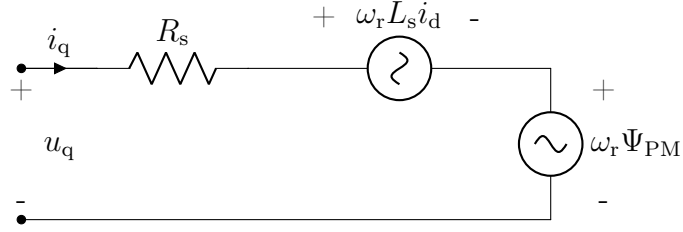
Figure 3.3: Q-axis equivalent circuit

The permanent magnets have high resistivity, hence the machine can be assumed to have a large effective air gap. Thus, the effects of saliency are negligible, and the magnetizing inductance is equal in both axes ($L_{md} = L_{mq} = L_m$). Another consequence of the large air gap is that the synchronous inductance ($L_s = L_{leak} + L_m$, where L_{leak} is the stator leakage inductance) becomes small and hence the effects of armature reaction are negligible [27].

Using Park's transformation [28], the dq-winding voltages can be expressed as [26, 27]

$$u_d = R_s i_d + \frac{d}{dt}\left(L_s i_d + \Psi_{PM}\right) - \omega_r L_s i_q \tag{3.2}$$

and

$$u_q = R_s i_q + \frac{d}{dt}\left(L_s i_q\right) + \omega_r \left(L_s i_d + \Psi_{PM}\right), \tag{3.3}$$

where u_d and u_q are the stator d- and q-axis voltages, i_d and i_q are the stator d- and q-axis currents, R_s denote the stator resistance, and Ψ_{PM} is the flux linkage of the permanent magnets. From the equivalent circuits in Figures 3.2 and 3.3 and the voltage expressions in equations (3.2) and (3.3), the steady-state equations can be obtained as

$$u_d = R_s i_d - \omega_r L_s i_q \tag{3.4}$$

and

$$u_q = R_s i_q + \omega_r \left(L_s i_d + \Psi_{PM}\right). \tag{3.5}$$

In order to keep the d-axis aligned with the rotor magnetic axis, the speed of the d-axis needs to be equal to the rotor angular speed of the generator ω_r [29]. It can be expressed as

$$\omega_r = \frac{n_p}{2}\omega_{mech}, \tag{3.6}$$

where ω_{mech} is the mechanical speed of the WEC given in equation (3.1) and n_p is the number of poles.

By considering that the electromagnetic torque of the SMPMSM is produced by the permanent magnets tendency to align themselves with the stator magnetomotive force (MMF), the generator torque can be expressed as

$$T_e = \frac{3}{2}\frac{n_p}{2}\Psi_{PM}i_q. \qquad (3.7)$$

3.2.1 Converter bridge with Pulse-Width Modulation

Converter bridges are used to control the magnitude and polarity of the output voltage [30]. It is commonly used in cooperation with Pulse-Width Modulation (PWM). Pulse-Width Modulation uses the comparison of an input reference voltage and a repetitive switching frequency triangular waveform to generate a switching signal. This switching signal is then used to control the switches in the converter bridge, and hence, the magnitude of the output voltage.

In control theory, the converter bridge is modelled as a time delay [31],

$$\frac{u_{ref}(s)}{u(s)} = \frac{1}{1 + T_{delay}s} , \qquad (3.8)$$

where the time delay T_{delay} depends on the PWM method used and the chosen switching frequency. A higher switching frequency will give a lower time delay.

In comparison to a slow wave energy system, T_{delay} can be considered to be equal to zero. This means that it is assumed that the output voltage follows the reference voltage perfectly. As a result, the simulation time is significantly reduced and no filter is needed in the system to handle the voltage harmonics caused by the power electronic converter.

3.2.2 Current control

The current controller regulates the armature current in order to generate the needed output voltage, and thus the desired electromagnetic torque. Here, the current controller is implemented in the synchronous reference frame. It is controlled by PI-controllers which ensure zero steady-state error and increased robustness of the closed loop system [32]. The PI-controller uses the stationary deviation between the reference d- and q-axis currents and the output d- and q-axis currents to calculate the reference voltage. A block diagram of the current controller is shown in Figure 3.4. The "PWM + converter"-block is set to unity, as discussed in Subsection 3.2.1.
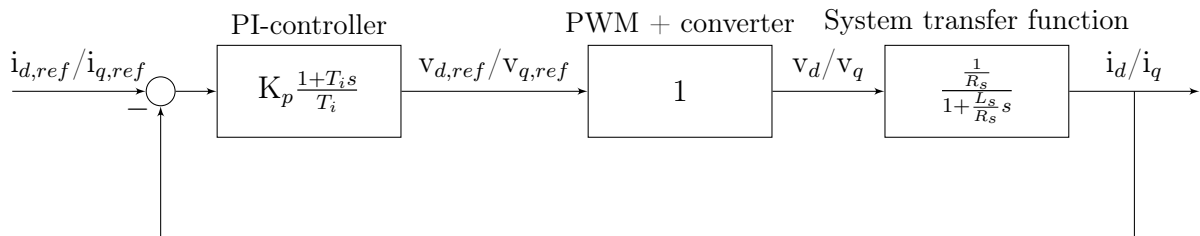
Figure 3.4: Block diagram of the current controller.

From equations (3.2) and (3.3), it can be seen that there is a cross coupling between the d- and q-axis voltages. This can be avoided by using a feed-forward technique where the reference voltages are defined as

$$v_{d,ref} = u_d + \omega_r L_s i_q \tag{3.9}$$

and

$$v_{q,ref} = u_q - \omega_r L_s i_d - \omega_r \Psi_{PM} . \tag{3.10}$$

Inserting equations (3.9) and (3.10) into equations (3.2) and (3.3) results in the two independent first-order equations given by

$$v_{d,ref} = R_s i_d + L_s \frac{di_d}{dt} \tag{3.11}$$

and

$$v_{q,ref} = R_s i_q + L_s \frac{di_q}{dt} . \tag{3.12}$$

Since the converter bridge with PWM is assumed to be ideal, the reference voltages will be equal to the output voltages, as seen in the block diagram in Figure 3.4. The system transfer function of the current controller can then be found by taking the Laplace transform of the first-order equations (3.11) and (3.12),

$$\frac{i(s)}{u(s)} = \frac{\dfrac{1}{R_s}}{1 + \dfrac{L_s}{R_s}s} . \tag{3.13}$$

Then, the open loop transfer function of the current controller can be expressed as

$$h_o(s) = K_p \frac{1 + T_i s}{T_i s} \frac{\dfrac{1}{R_s}}{1 + \dfrac{L_s}{R_s}s} . \tag{3.14}$$

The parameters of the PI-controller can be found through modulus optimum [33]. In a system where the open loop transfer function is of the form of equation (3.14), the time constant of the PI-controller is equal to the dominant time constant [31], which here is the armature time constant. Inserting $T_i = \dfrac{L_s}{R_s}$ into equation (3.14) gives the following open loop transfer function

$$h_o(s) = K_p \frac{1}{L_s s} . \tag{3.15}$$

It is desirable to have the closed loop transfer function as close to unity as possible because it describes how well the output signal follows the reference signal. A closed loop transfer function equal to 1 means that the output signal follows the reference signal perfectly [34]. The closed loop transfer function is given by

$$M(s) = \frac{h_o(s)}{1 + h_o(s)} \,. \tag{3.16}$$

As can be seen from equation (3.16), $M(s) = 1$ when $|h_o(s)| >> 1$. Substituting $j\omega$ for s, it can be shown that this happens when $K_p >> L_s\omega$.

3.2.3 Torque control

Torque control is required in order to ensure that the PTO limitations are not exceeded. The PTO limitations are related to the maximum torque and force the PTO system can withstand, the maximum current in the generator, the constant DC-link voltage and the maximum speed of the generator. For a fixed inverter capacity, the voltage and current constraints can be expressed as

$$i_q^2 + i_d^2 \leq I_{max}^2 \tag{3.17}$$

and

$$u_q^2 + u_d^2 \leq U_{max}^2 \,. \tag{3.18}$$

The maximum current can either be fixed to the current rating of the motor/inverter or be adaptive in case of an active thermal management [35]. Here, the maximum current is fixed to the inverter current rating. The maximum voltage depends on the DC-link voltage and the applied PWM method [35]. In this thesis, an ideal PWM is assumed, implying that the maximum voltage is limited to the constant DC-link only.

Inserting the steady-state expressions in equation (3.4) and (3.5) into the voltage constraint in equation (3.18) gives the voltage constraint in terms of the stator currents, as shown in the following expression,

$$\left(i_d + \frac{\omega_r^2 L_s \Psi_{PM}}{R_s^2 + \omega_r^2 L_s^2}\right)^2 + \left(i_q + \frac{\omega_r R_s \Psi_{PM}}{R_s^2 + \omega_r^2 L_s^2}\right)^2 \leq \frac{U_{max}^2}{R_s^2 + \omega_r^2 L_s^2} \,. \tag{3.19}$$

Since the SMPMSM is current controlled, it is convenient to define the operating range in the $i_d i_q$-plane, where the operating range is determined by the overlapping of the current limit circle and the voltage limit, plotted in Figure 3.5. As can be seen from equation (3.19), the voltage limit defines a circle with a center offset from the origin, where the size of the limit is inversely proportional to the generator speed and/or varying DC-link voltage. The center of the voltage limit circle is termed the infinite-speed operation point because at high speeds the operating point converge towards it [36]. From equation (3.7), it can be seen that a constant torque forms straight lines, parallel to the d-axis, in the $i_d i_q$-plane. The optimal operating region is enclosed by both the current limit circle and the voltage limit circle.
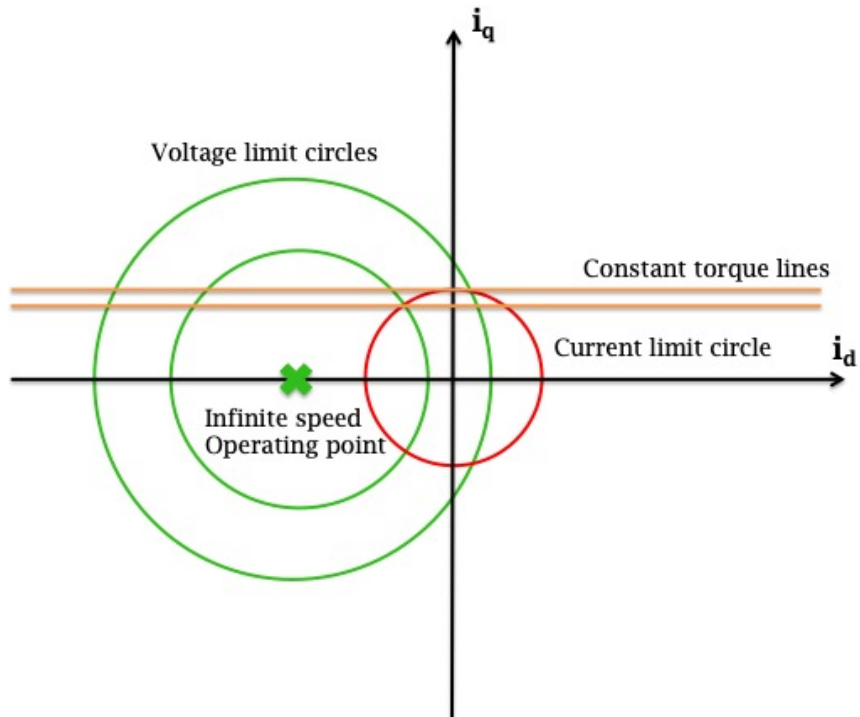
Figure 3.5: Circle diagram for a SMPMSM

Since the optimal operating region is determined by the current and voltage, where the voltage is dependent on the generator speed, the torque control will be defined by the current and the generator speed. From equation (3.7), the reference q-axis current can be expressed as

$$i_{q,ref} = \frac{T_{e,ref}}{\frac{3}{2}\frac{n_p}{2}\Psi_{PM}} \, , \tag{3.20}$$

where the reference torque $T_{e,ref}$ is calculated using the machinery force from the hydro-dynamic model,

$$T_{e,ref} = \frac{1}{\rho_g}f_p(t) \, . \tag{3.21}$$

Here, ρ_g is the angular to linear gear ratio and $f_p(t)$ is defined as shown in equation (2.9). The generator speed is calculated as shown in equation (3.6). Figure 3.6 shows an illustration of how torque control is implemented in this thesis [10].
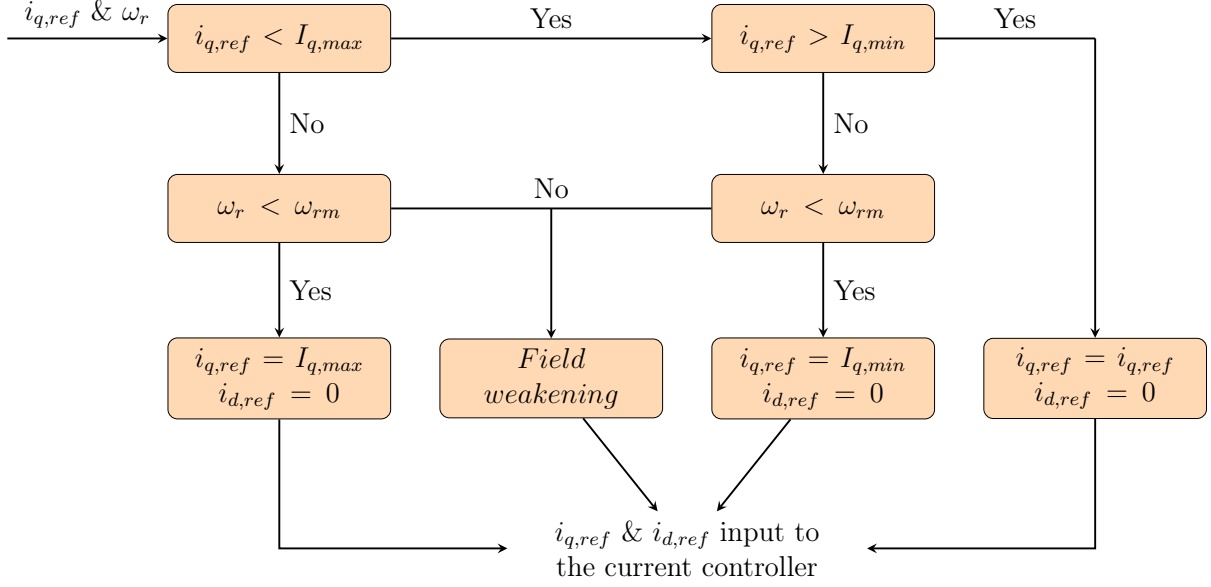
Figure 3.6: Illustration of the implementation of torque control

In Figure 3.6, $I_{q,max}$ refers to the maximum PTO torque the system can withstand and $I_{q,min}$ corresponds to the minimum torque constraint that is needed to maintain tension in the mooring line. Further, w_{rm} is the generator speed where field weakening is initiated, and it can be calculated using the generator characteristics as [37]

$$\omega_{rm} = \frac{-2R_s I_{max}\Psi_{PM} + \sqrt{(2R_s I_{max}\Psi_{PM})^2 - 4(\Psi_{PM}^2 + L_s^2 I_{max}^2)(R_s^2 I_{max}^2 - U_{max}^2)}}{2(\Psi_{PM}^2 + L_s^2 I_{max}^2)}.$$

(3.22)

Field weakening

Field weakening is applied to allow the SMPMSM to operate in generator speeds that are above the rated value, thus also limiting the voltage to not exceed the DC-link voltage U_{max}. Due to the construction of the permanent magnets, it is not possible to achieve direct field weakening [27]. In a SMPMSM, the effect of field weakening is obtained by introducing a negative d-axis current alongside the q-axis current. Note that by introducing a d-axis current, the magnitude of the q-axis current has to be decreased in order to not exceed the current constraint in equation (3.17). In this thesis, the method for determining the reference currents during field weakening is based on the robust field weakening control strategy described by Ching-Tsai Pan and Jenn-Horng Liaw [37].

First, the current and voltage constraints in equations (3.17) and (3.19) can be expressed as

$$f_1(i_{d,ref}, i_{q,ref}) = i_{d,ref}^2 + i_{q,ref}^2 - I_{max}^2 = 0$$

(3.23)

and

$$f_2(i_{d,ref}, i_{q,ref}, \omega_r) = (i_{d,ref} - i_{dc})^2 + (i_{q,ref} - i_{qc})^2 - \frac{U_{max}^2}{R_s^2 + \omega_r^2 L_s^2} = 0 \,, \tag{3.24}$$

where i_{dc} and i_{qc} represent the coordinates to the center of the voltage limit circle, defined as

$$i_{dc} \equiv -\frac{\omega_r^2 L_s \Psi_{PM}}{R_s^2 + \omega_r^2 L_s^2} \tag{3.25}$$

and

$$i_{qc} \equiv -\frac{\omega_r R_s \Psi_{PM}}{R_s^2 + \omega_r^2 L_s^2} \,. \tag{3.26}$$

From equation (3.23), the reference q-current can be expressed as

$$i_{q,ref} = \sqrt{I_{max}^2 - i_{d,ref}^2} \,. \tag{3.27}$$

Inserting equation (3.27) into equation (3.24) yields the following quadratic equation for the d-axis current,

$$a i_{d,ref}^2 + b i_{d,ref} + c = 0 \,, \tag{3.28}$$

where

$$
\begin{aligned}
a &\equiv 4(i_{dc}^2 + i_{qc}^2) \\
b &\equiv 4 i_{dc} \left[\frac{U_{max}^2}{R_s^2 + \omega_r^2 L_s^2} - \left(I_{max}^2 + i_{dc}^2 + i_{qc}^2 \right) \right] \\
c &\equiv \left[\left(I_{max}^2 + i_{dc}^2 + i_{qc}^2 \right) - \left(\frac{U_{max}^2}{R_s^2 + \omega_r^2 L_s^2} \right)^2 \right] - 4 i_{qc}^2 I_{max}^2 \,.
\end{aligned}
\tag{3.29}
$$

Solving the quadratic equation will result in two different solutions for the d-axis reference current. These solutions correspond to the two points where the current limit circle crosses the voltage limit circle. In other words,

$$i_{d1,ref} = \frac{-b + \sqrt{b^2 - 4ac}}{2a} \,, \omega_r > 0 \tag{3.30}$$

and

$$i_{d2,ref} = \frac{-b - \sqrt{b^2 - 4ac}}{2a} \,, \omega_r < 0 \,. \tag{3.31}$$

For this PTO system, the determinant $b^2 - 4ac$ is always positive [38]. It is also a requirement that $i_{d,ref}$ is always less than or equal to zero. After the d-axis reference current is found, the reference q-current can be found by solving equation (3.27).

3.3 Output electrical power

As described by Sjolte et al. [10], the detailed properties of the generator and converter bridge is not known. However, the efficiency of the generator and converter bridge at a number of operating points have been provided from the manufacturers. On the basis of these operating points, a polynomial expression for the power losses has been developed as a function of the generator torque T_e and the generator speed ω_r in rpm, and is given by [10]

$$|P_l| = a_1 T_e^4 + a_2 T_e^2 + a_3 |\omega_r| + a_4 \omega_r^2 + a_5 |\omega_r T_e| + a_6 |\omega_r| T_e^2 \,. \tag{3.32}$$

The resulting efficiency map is shown in Figure 3.7.
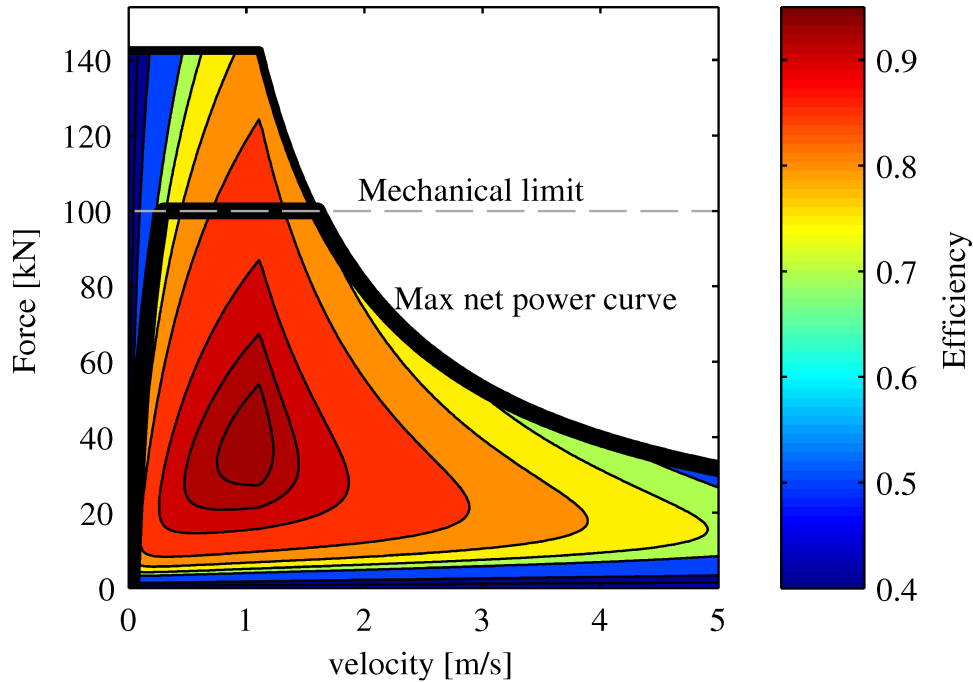
Figure 3.7: Generator and converter bridge efficiency map [10]

As a result of the development of the power losses expression (3.32), the stator copper losses needs to be removed from the voltage expressions (3.2) and (3.3), in order to not calculate the stator copper losses twice.

The output instantaneous electrical power can be found directly by,

$$P_e(t) = P_{mech}(t) - |P_l(t)| \,. \tag{3.33}$$

Since the power loss equation (3.32) is built on the basis of measured values, the mechanical power needs to be transformed into three-phase values before it can be used in

equation (3.33),

$$P_{mech} = \frac{3}{2} \left(i_a u_a + i_b u_b + i_c u_c \right) ,$$ (3.34)

where the currents and voltages, denoted by x, can be found by

$$\begin{bmatrix} x_a(t) \\ x_b(t) \\ x_c(t) \end{bmatrix} = \sqrt{\frac{2}{3}} \begin{bmatrix} cos(\theta) & -sin(\theta) \\ cos(\theta + \frac{4}{3}) & -sin(\theta + \frac{4}{3}) \\ cos(\theta + \frac{2}{3}) & -sin(\theta + \frac{4}{3}) \end{bmatrix} \begin{bmatrix} x_d \\ x_q \end{bmatrix} .$$ (3.35)

The average electrical and mechanical power can be found by

$$\bar{P}_e = \frac{1}{T} \int_0^T P_e(t) dt$$ (3.36)

and

$$\bar{P}_{mech} = \frac{1}{T} \int_0^T P_{mech}(t) dt .$$ (3.37)

Chapter 4

Control methods

The amount of energy the WEC is able to absorb from the waves depend on the frequency response of the floating body and the control method applied at the PTO. The control system aims to manipulate the PTO system into resonance damping and stiffness by, for instance, tuning the load impedance. In this thesis, two control methods are applied: passive loading (PL) with constant damping and a passive control (PC) scheme that tunes the PTO damping on a wave-to-wave basis.

4.1 Theoretical maximum absorbed energy

In order to absorb energy from the waves, energy needs to be removed from the waves. Hence, there must either be a cancellation or reduction of waves that are passing the WEC or are being reflected from it. This can be realised through an oscillating device that oscillates in counterphase with the waves, which means that the generated waves have to interfere destructively with the incident waves. An illustrative example is shown in Figure 4.1.
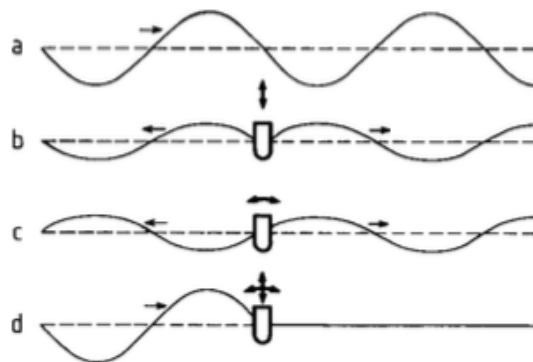
Figure 4.1: Curve a represents an undisturbed incident wave. Curve b illustrates symmetric wave generation (on calm water) by means of a floating body oscillating in heave. Curve c illustrates antisymmetric wave generation. Curve d represents the superposition of the above three waves and illustrate the complete absorption of the energy from the incident wave. [18]

In order to extract the maximum energy from the incident waves, the WEC needs to have

an optimum oscillation with an optimum phase and amplitude. Referring to Figure 4.1, the optimum amplitude for curve b and c is half of the amplitude of curve a. Additionally, curve b and c needs to have the same phase for the wave generated towards the right, resulting in that the waves generated to the left cancel each other out. With respect to the incident wave (curve a), the generated waves (curves b and c) have to oscillate so that the crests of the generated waves towards the right coincide with the troughs of the incident wave. The oscillating device needs to operate in more modes of freedom in order to be able to absorb most of the incident wave energy, as illustrated by curve d in Figure 4.1. In simplicity, it is this behavior the control strategy is trying to accomplish. [39]

4.2   Passive loading

Passive loading consists of setting the PTO damping to a constant value, i.e., $B_p(t) = B_p$, for any time t, where B_p is adjusted according to a chosen tuning frequency ω. For an incoming regular wave, the optimal PTO damping can be found by [18]

$$B_p = \sqrt{B_r(\omega)^2 + \left[\omega(m + m_r(\omega)) - \frac{S}{\omega} \right]^2} \,. \tag{4.1}$$

This expression is referred to as the optimum amplitude condition [18]. The optimum amplitude condition is related to the generated wave created by the oscillating body that interferes with the incoming wave.

It is also desirable that the oscillating velocity is in phase with the excitation force, which automatically happens when the WEC is in resonance with the incoming wave. This is referred to as the optimum phase condition and states that

$$\omega(m + m_r(\omega)) - \frac{S}{\omega} = 0 \,. \tag{4.2}$$

The maximum amount of absorbed power from the incident waves is obtained when both the optimum amplitude condition and optimum phase condition are satisfied. Then, the PTO damping becomes equal to the radiation damping coefficient, $B_p = B_r(\omega)$.

Real ocean waves do not consist of a single frequency in the time domain, making it challenging to select a tuning frequency when passive loading is applied. Usually, either the peak or energy frequency of the wave spectrum is selected as the tuning frequency. The PTO damping can be tuned on different time scales established by either variations in the sea state (hourly basis), seasonal variations (monthly basis) or on an annual basis [40].

The Kalman Filter (KF) is an algorithm used to predict the past, present and future states of the system by using prior knowledge of the system states. The Extended Kalman Filter (EKF) is an extension of the KF that is applied to non-linear systems, whereas KF is used on linear systems. In wave energy, EKF can be used to predict the incoming waves [41]. If EKF is applied in the control system of a WEC, it can be used to find a suitable tuning frequency for the incoming waves, and hence calculate a more optimal PTO damping. Simulation studies in [12] have indicated that the EKF estimates the mean centroid frequency of the excitation force spectrum $\omega_{1,fe}$. Thus, the mean centroid

frequency of the excitation force spectrum is used as the frequency for tuning the PTO damping in this thesis.

The mean centroid frequency (ω_1) is a statistical parameter of the wave spectrum. It is used in order to calculate characteristic wave periods of the sea state [42], and is given by

$$\omega_1 = \frac{m_1}{m_2}, \tag{4.3}$$

where the spectral moments of the n-th order are calculated as

$$m_n = \int_0^\infty \omega^n S(\omega) d\omega. \tag{4.4}$$

4.3 Passive control using the Hilbert-Huang transform

The passive control scheme presented here tunes the PTO damping on a wave-to-wave basis. Using equation (4.1), the PTO damping can be found by

$$B_p(t) = \sqrt{B_r(\hat{\omega}_d)^2 + \left[\hat{\omega}_d(m + m_r(\hat{\omega}_d)) - \frac{S}{\hat{\omega}_d}\right]^2}, \tag{4.5}$$

where $\hat{\omega}_d$ is the estimated dominant frequency of the excitation force. Here, the excitation force is used rather than the wave elevation because the excitation force transfer function $H_e(\omega)$ filters out some of the high frequency content of the wave elevation, and generally low-frequency waves have the highest power [6]. In this thesis, the frequency is estimated by using the Hilbert-Huang Transform (HHT), as done by Garcia-Rosa et al. [11].

The HHT is a two-step method used to analyze non-linear and non-stationary signals. First, it uses the Empirical Mode Decomposition (EMD) to decompose the original signal into Intrinsic Mode Functions (IMFs). Intrinsic Mode Functions are functions with a single frequency that varies over time. Secondly, the Hilbert Transform (HT) is applied on each IMF component in order to estimate the instantaneous amplitude and frequency [43]. The HT can only produce physically meaningful results for single frequency components [44].

The EMD empirically identifies, through a sifting process, the different frequency components (IMFs) that constitute the original signal. An IMF has the following characteristics [44]:

1. Mean value is zero

2. The number of local maxima and minima differs just by one

Here, EMD is applied to the excitation force, and the sifting process can be explained in the following algorithm:

0. Set $i = 1$ and $r(t) = f_e(t)$;

1. Locate all local minima and maxima in $r(t)$;

2. Using cubic spline interpolation, create lower and upper envelopes from the corresponding minima and maxima;

3. Calculate the mean of both envelopes $m(t)$;

4. Subtract the mean from the signal, $h(t) = r(t) - m(t)$;

5. If $h(t)$ can be classified as an IMF, go to the next step. Otherwise, set $r(t) = h(t)$ and repeat the process from 1;

6. Set $c_i(t) = r(t)$ and calculate $r(t) = r(t) - c_i(t)$.

7. Set $i = i + 1$ and repeat the process from 1. If $i = N$, define the IMF components as $c_1(t)$, ..., $c_N(t)$ and the residue as $r(t)$.

In the defined algorithm, N is the predetermined number of IMF components. When the EMD has been completed, the sum of the IMF components should result in the original signal,

$$f_e(t) = \sum_{i=1}^{N} c_i(t) + r(t) \,, \tag{4.6}$$

and the IMF components are given in a sequential order from the highest frequency component to the lowest. Figure 4.2, gives an illustration of how step 2 and 3 in the sifting process are determined.
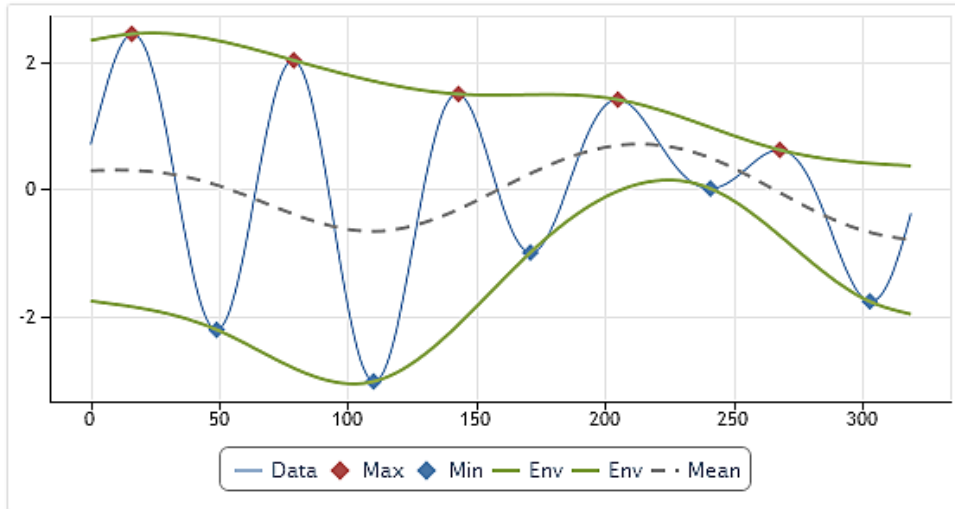
Figure 4.2: Illustration of the envelope concept in EMD [45]

In the PC strategy, the dominant frequency is defined as the IMF component with the highest energy content. The natural next step of the PC scheme is then to calculate the amount of energy in each IMF component,

$$E_{c_i} = \int_0^T |c_i(t)|^2 dt \,, \tag{4.7}$$

where $c_i(t)$ is the i-th IMF component. Then, the dominant IMF component $c_d(t)$ is located.

Subsequently, the HT is applied to the dominant IMF component. The HT calculates the conjugate pair of the dominant IMF component $c_d(t)$,

$$v_d(t) = \frac{1}{\pi} P \left\{ \int_{-\infty}^{\infty} \frac{c_d(\tau)}{t-\tau} d\tau \right\} , \tag{4.8}$$

where P is the Cauchy principal value. In this way, the dominant IMF component can be expressed as an analytical signal,

$$z_d(t) = c_d(t) + j v_d(t) = \hat{a}_d(t) e^{\int \hat{\omega}_d(t) dt} , \tag{4.9}$$

where the instantaneous amplitude $\hat{a}_d(t)$ and instantaneous frequency $\hat{\omega}_d(t)$ can be calculated as

$$\hat{a}_d(t) = \sqrt{c_d(t)^2 + v_d(t)^2} \tag{4.10}$$

and

$$\hat{\omega}_d(t) = \frac{d}{dt} \arctan \left[\frac{v_d(t)}{c_d(t)} \right] . \tag{4.11}$$

The instantaneous frequency found through the HT is then used as the input to a moving average filter in order to filter out unwanted noisy components from the calculated instantaneous frequency. Finally, the output is used as the tuning frequency when the PTO damping is calculated as shown in equation (4.5).

Chapter 5

Simulation parameters

5.1 Simulation parameters

In order to obtain meaningful statistical parameters for a wave field, a minimum time interval of 15 min is usually required. The simulation time has therefore been chosen as 30 min. The sampling frequency is chosen as 1.28 Hz, which is the sampling frequency usually used in real wave measurements. From the EMD simulation, one of the challenges is the end effects, which are induced by spline interpolation and appear at the boundaries of the signal. To eliminate these end effects, the first and last 20 s of the simulations have been excluded from the final results. In these simulations, there are 5 IMF components.

5.1.1 Wave data

In this thesis, the wave data used is based on the real wave data taken at the Belmullet wave energy test site as shown in [11]. In order to minimize the difference between the theoretical and observed wave spectra, the Ochi-Hubble spectrum is used. The spectral parameters are numerically set to mimic the following three sea states: S1, S2, and S6 (renamed to S3 here). In Table 5.1, the spectral parameters for each sea state are listed.

Table 5.1: Spectral parameters used in the Ochi-Hubble spectra

	H_{s_1}	H_{s_2}	ω_{m_1}	ω_{m_2}	λ_1	λ_2
S1	1.5 m	0 m	0.52 rad/s	0 rad/s	5	0
S2	1.1 m	1.5 m	0.59 rad/s	1.22 rad/s	2	2
S3	1.4 m	0.9 m	0.57 rad/s	1.934 rad/s	2	2

The resulting Ochi-Hubble spectra for each sea state are shown in Figure 5.1.
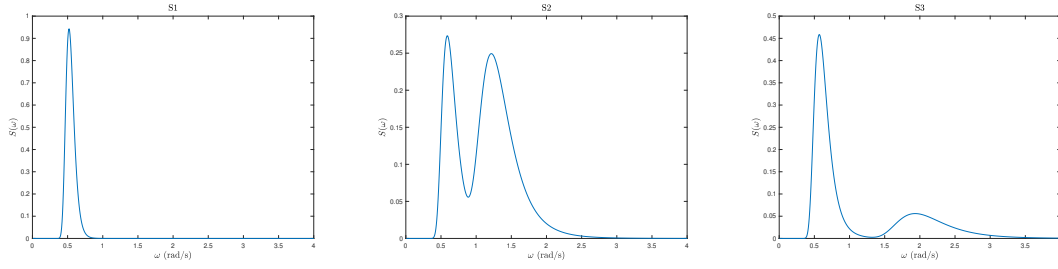
Figure 5.1: Ochi-Hubble spectra for all sea states

Inserting the Ochi-Hubble spectra from Figure 5.1 and $\pi/500$ for the step between each spectral frequency $d\omega$ into equation (2.3), the wave elevation can be calculated. Using Welch's method [46] and the found wave elevation, the simulated wave spectra and the spectral density of the excitation force can be found as shown in Figures 5.2 and 5.3.
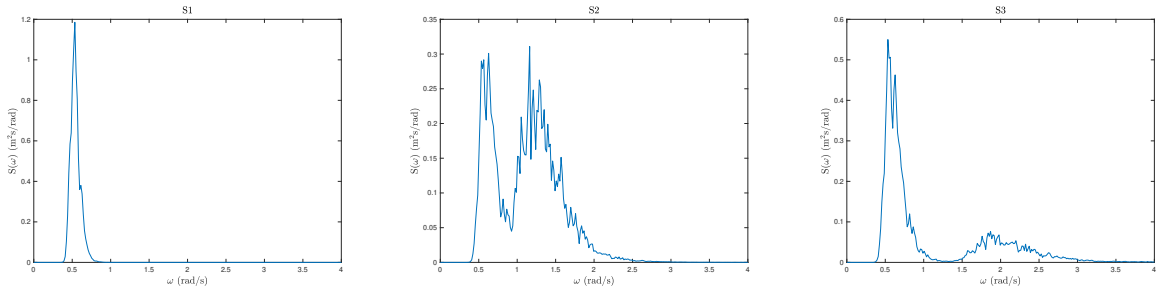
Figure 5.2: Simulated wave spectra for all sea states

Comparing the wave spectra with the excitation force spectra, it can be noticed that some of the higher frequencies in the wave spectra have been filtered out by the excitation force transfer function $H_e(\omega)$.
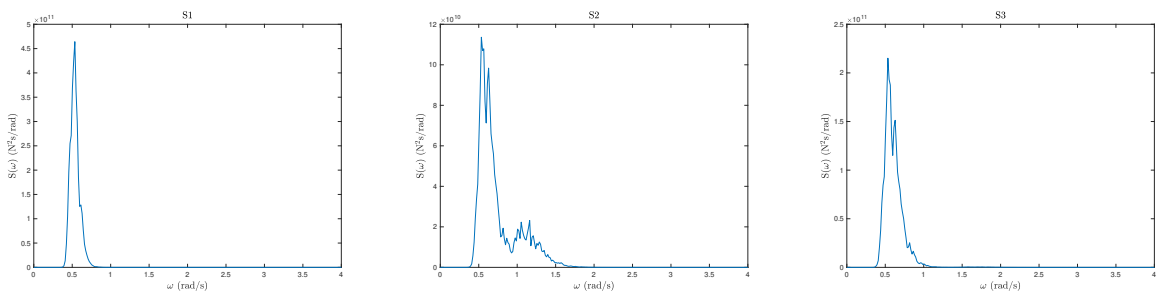
Figure 5.3: Spectral density of the excitation force for all sea states

5.1.2 Hydrodynamic data

The specifications of the heaving cylinder is presented in Table 5.2.

Table 5.2: Specifications of the oscillating body

Property	Value
Body mass, m	$3.2 \cdot 10^5$ kg
Radius	5 m
Draught	4 m
Hydrostatic stiffness, S	$7.9331 \cdot 10^5$ N/m
Added mass at infinite frequency, $m_r(\infty)$	$2.3325 \cdot 10^5$ kg
Resonance frequency	1.1936 rad/s

The cylinder is the same as used in [11], where the hydrodynamic coefficients were calculated using the boundary element solver WAMIT. Figure 5.4 shows the added mass, radiation damping and the excitation force frequency response of the cylinder.

(a) Added mass $m_r(\omega)$

(b) Radiation damping $B_r(\omega)$

(c) Magnitude of the excitation force frequency response $|H_e(\omega)|$

(d) Phase of the excitation force frequency response $\angle H_e(\omega)$
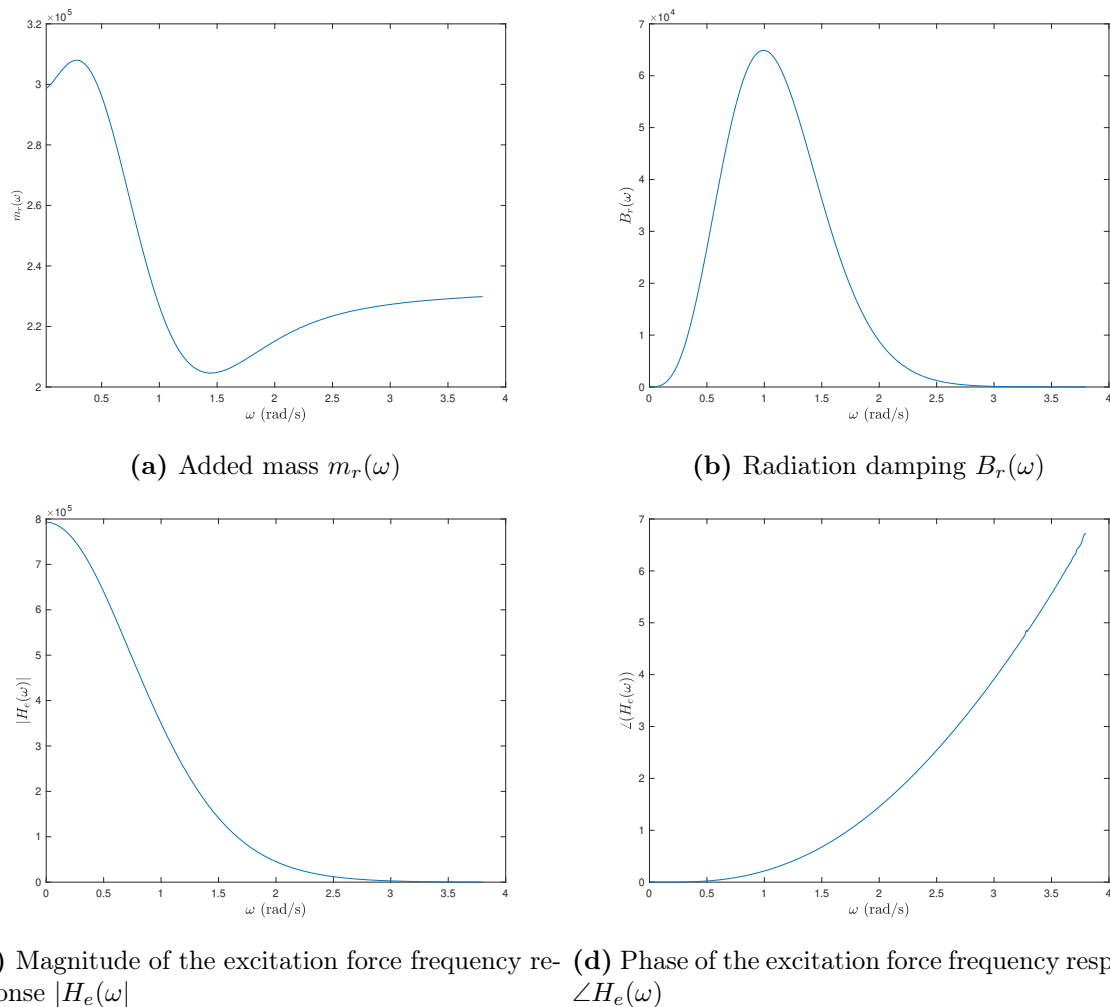
Figure 5.4: Hydrodynamic coefficients of the heaving cylinder

5.1.3 Electrical data

As previously mentioned, the electric PTO system considered here is based on the electric PTO system of the WEC Lifesaver in [10]. The stand-alone system consists of the following components [47]:

- Surface-mounted permanent magnet synchronous machine

- Inverter/Rectifier

- Ultra-capacitor bank

- DC-link charger

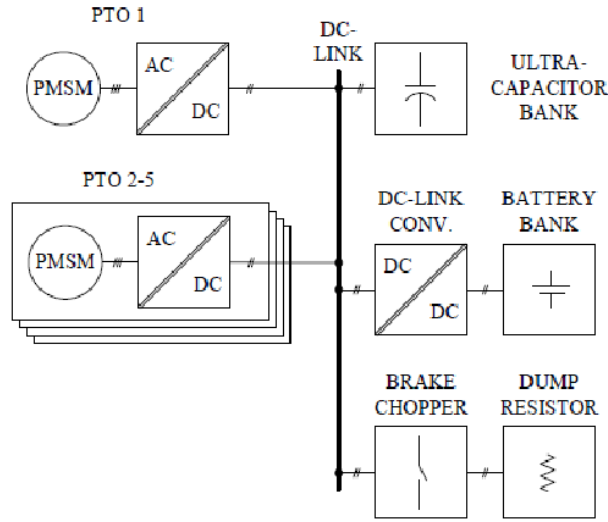- Battery charger

- Brake charger

- Dump resistor

The topology of the stand-alone system is shown in Figure 5.5. In this thesis, the system that connects the WEC to the grid is not considered, and thus the PTO system is only connected to the DC-link with no energy storage.

Figure 5.5: Topology of the stand-alone system in Lifesaver [47]

The main specifications of the electric PTO system, as defined in [10], are given in Table 5.3.

Table 5.3: Main specifications of the electric PTO

Property	Value
DC-bus voltage, U_{max}	600 V
DC-bus current, I_{max}	481.2679 A
Angular to linear gear ratio, ρ_g	38.5 1/m
PTO nominal speed	1.1 m/s
PTO maximum speed, $\dot{x}_{max}$	1.55 m/s
PTO maximum force	100 kN
PTO minimum force	10 kN
PTO nominal production power	15 kW
PTO maximum power	155 kW
PTO maximum torque	2.5974 kNm

The characteristics of the 28-pole SMPMSM used for this model are listed in Table 5.4.

Table 5.4: Generator characteristics

Property	Value
Nominal generator speed	400 rpm
Maximum generator speed, ω_{max}	1800 rpm
Field weakening speed, ω_{rm}	561.1284 rpm
Rated power	83.7 kW
Maximum torque	3700 Nm
Number of poles, n_p	28
Stator resistance, R_s	0.038 Ω
Stator inductance, L_s	1.4 mH
Permanent magnet flux linkage, Ψ_{PM}	0.257 Wb
Minimum q-current, $I_{q,min}$	48.1268 A
Maximum q-current, $I_{q,max}$	481.2679 A

As previously mentioned, the maximum $I_{q,max}$ and minimum $I_{q,min}$ q-current values in Table 5.4 refer to the maximum and minimum i_q with the given torque constraints.

PI-controller

In Subsection 3.2.2, the design of the current controller was presented. As the converter bridge with PWM is assumed ideal, it was concluded that $K_p >> L_s\omega$. Inserting the maximum velocity $\dot{x}_{max}$ of the PTO into equations (3.1) and (3.6) gives a maximum generator speed of 835.45 rad/s. From Table 5.4, the rated maximum generator speed is 1800 rpm or 188.5 rad/s. When the controller gain is chosen, the rated maximum generator speed is used since it is the limiting value for the generator speed in the system. The inequality then states,

$$K_p >> 1.4 \cdot 10^{-3} \cdot 1800 \cdot \frac{2\pi}{60} = 0.26 \,. \tag{5.1}$$

After running the simulations for both control methods, K_p was chosen to be equal to 0.8. The assessments around the choice of this value and the influence on the results are discussed in Subsection 6.2.10.

5.2 Wave-to-wire model

In this thesis, the Matlab and Simulink environment has been used for the simulations. The complete wave-to-wire model applied for the simulations is shown in Figure 5.6, where the scaling factor is set to unity since the dimensions of the heaving cylinder are of the same order of magnitude as the Lifesaver floating body. Lifesaver has 1 m height and is shaped as a toroid with an inner diameter of 10 m and an outer diameter of 16 m. The subsystems are included in Appendix A.1.
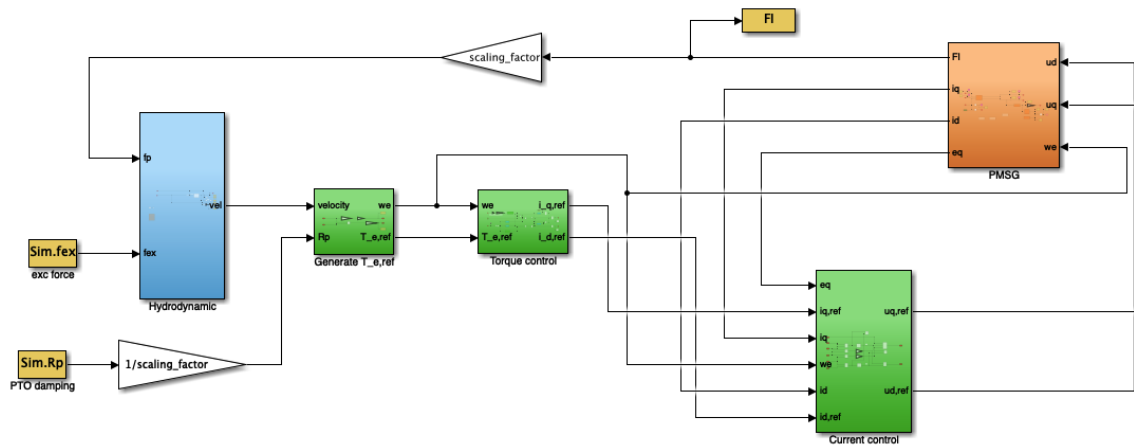
**Figure 5.6:** The full wave-to-wire model built in Simulink

Chapter 6

Simulation results

6.1 Hydrodynamic model

In order to study the effect PC has on a fully-coupled wave-to-wire model, the results, presented in Section 6.2, will be compared to the case when only the hydrodynamic model is considered. For simulations with only the hydrodynamic model, i.e., assuming ideal PTO system, the absorbed energy when the PTO damping is tuned with PL and PC is shown in Figure 6.1.
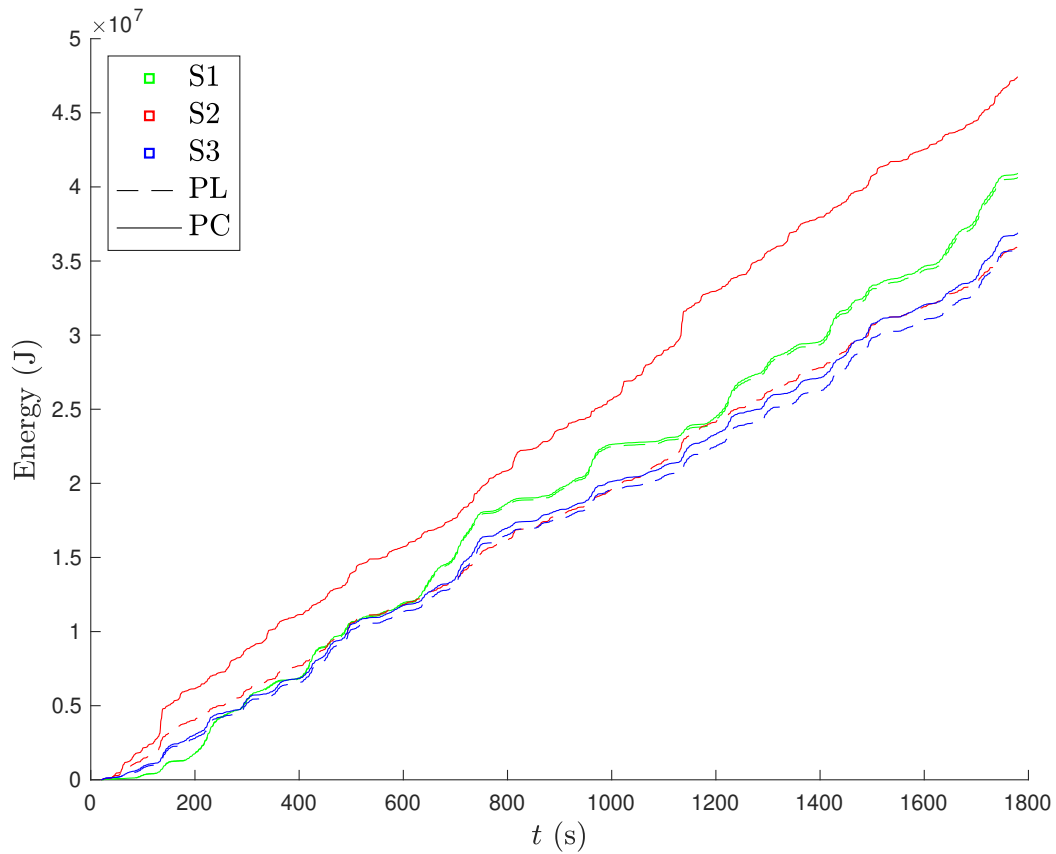
Figure 6.1: Absorbed energy over the entire simulation interval

From Figure 6.1, it can be seen that the absorbed energy for PC (i.e., PTO tuned with HHT frequencies) is higher than for PL tuned with $\omega_{1,fe}$. Using equation (2.12), the average absorbed power for each control method can be found as shown in Figure 6.2.
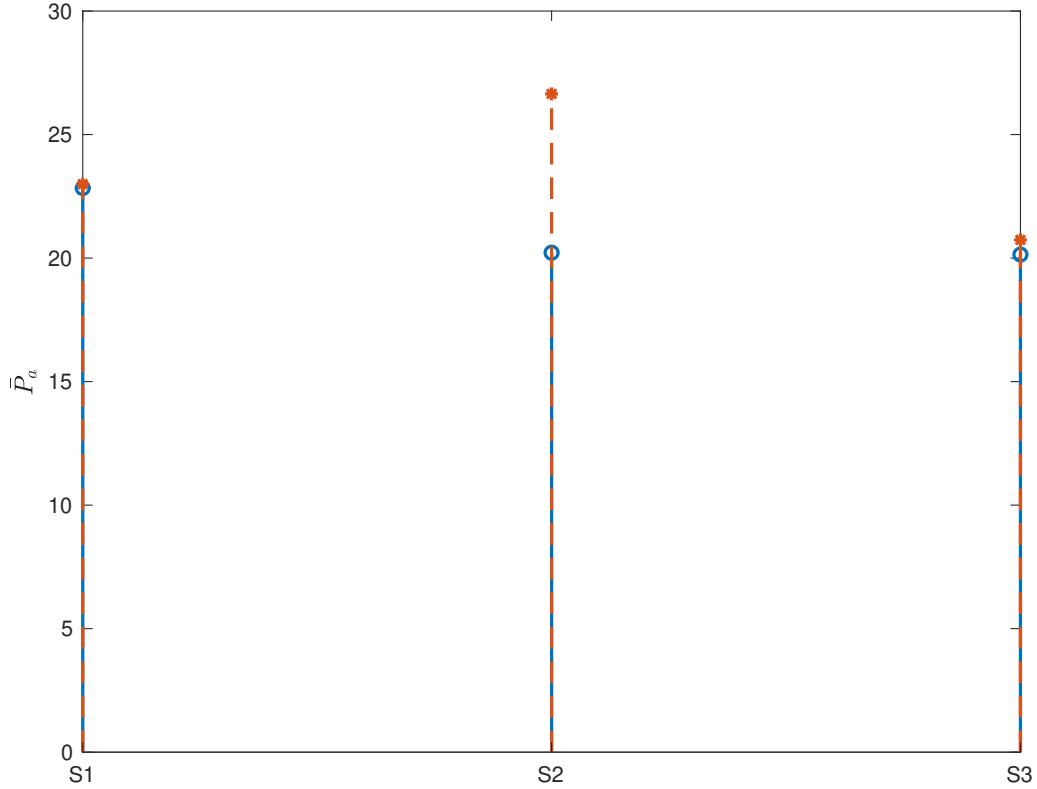
Figure 6.2: Average absorbed power $\bar{P}_a$ in kW for PL (blue) and PC (orange) when only the hydrodynamic model is considered.

The ratios between the average absorbed power $\bar{P}_a$ with PL and PC is shown in Table 6.1.

Table 6.1: Ratios between $\bar{P}_a$ with PL and PC

|	S1	S2	S3
$\bar{P}_a(PC)/\bar{P}_a(PL)$	1.01	1.32	1.03

From all the presented results, the absorbed power is higher for PC than for PL for all sea states. The advantage of PC over PL is more apparent for S2 than for the other sea states, where S2 is a sea state with mixed waves spread over a wide band of frequencies. These results agree with previous studies [11].
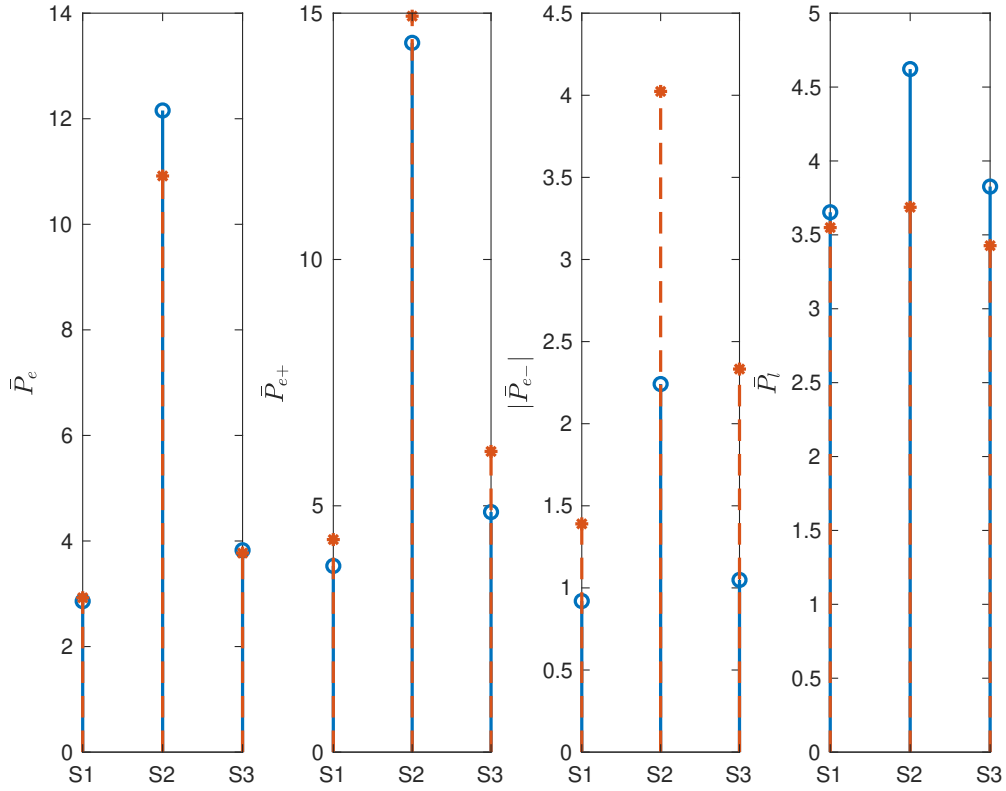
6.2 Wave-to-wire model

6.2.1 Average output power

The WEC only produces power during the upwards motion of the floating body and draws power from the grid during the downwards motion, as explained in Section 1.2. Thus, the average powers have been split into its positive and negative components in order to better verify the effect each control method has on the electric power output. In Figure 6.3, the average mechanical powers for both control methods, found by equation (3.37), are given.
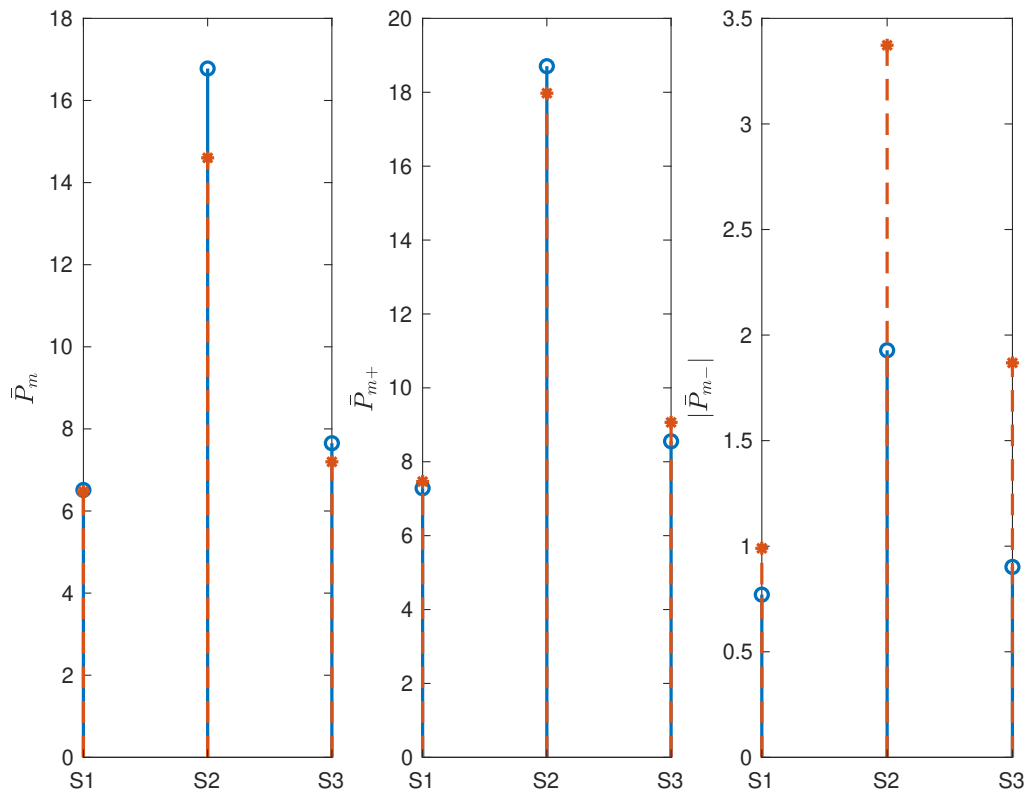
Figure 6.3: Average mechanical power $\bar{P}_{mech}$ in kW for PL (blue) and PC (orange) when the wave-to-wire model is considered

The average electrical power and losses for both PL and PC are shown in Figure 6.4. Using these results, it can be found that PL on average gives 6% more electrical power output than PC.

Figure 6.4: Average electrical power $\bar{P}_e$ and losses $\bar{P}_l$ in kW for PL (blue) and PC (orange) when the wave-to-wire model is considered

From Figure 6.4, it can be seen that PC results in more generated power (positive electrical power), but PC also requires more power from the grid in order to maintain tension in the mooring line (negative electrical power) than when PL is applied. On the other hand, using PL as the control method results in more average power losses than PC. In Table 6.2, the ratios between the average electrical powers and losses for the two control methods are shown.

Table 6.2: Ratios of the average electrical powers and losses for PL and PC

Ratio	S1	S2	S3
$\bar{P}_e(PC)/\bar{P}_e(PL)$	1.02	0.9	0.99
$\bar{P}_{e+}(PC)/\bar{P}_{e+}(PL)$	1.14	1.04	1.25
$\bar{P}_{e-}(PC)/\bar{P}_{e-}(PL)$	1.51	1.8	2.22
$\bar{P}_l(PC)/\bar{P}_l(PL)$	0.97	0.8	0.9

Power losses

In Section 3.3, the calculation of the power losses are presented. From equation (3.32), it can be seen that the power losses in this model are dependent on the generator speed ω_r and generator torque T_e. In the polynomial expression, the generator torque is raised to the fourth power, resulting in that the losses are higher for cases with higher torque

values. This means that if there are larger deviations in the generator torque between PL and PC it will be seen in the total power losses, which might explain the difference in the power losses from Figure 6.4, especially if the generator speed is very similar.

Here, the calculated power losses are only found based on the stator copper losses, but in a SMPMSM, the iron losses are also a significant fraction of the total losses [36]. The iron losses have an effect on the efficiency and performance of the machine, and could result in overheating and a reduction of the rated torque and efficiency [48]. In [49], it was also shown that iron losses in PM-generators have a high impact on the electric efficiency at low speeds. A common trade with renewable energy applications, as wave power, is that the generators operate with lower speeds and varying frequency, making the iron loss an important contributor to the total power losses in a WEC. On the basis of this, an inclusion of the iron losses in the model could result in different electrical power output results. The iron losses from the rotor are normally considered to be small and negligible, whereas the iron losses in the stator teeth and yoke represent the main portion of the total iron losses [50]. This means that in order to include the iron losses in the model, more knowledge about the generator is needed. However, the iron losses are usually much smaller than the stator copper losses [25], which means that the total power losses might not be that different if the iron losses are included.

A generator is designed to work in a stationary manner with small variations in its operational state. When PC is applied, the PTO damping is modified on a wave-to-wave basis, forcing the generator to constantly change, making it work in a way it has not been designed for. As a result, there might be other losses related to wear and tear, and hence more maintenance could be required over time.

The polynomial expression that calculates the power losses is found on the basis of both the generator losses as well as the converter losses [10]. The losses related to the converter are small compared to the generator and contributes with 3-10% of the total losses [10]. However, the converter is assumed to be ideal, and it is not clear if losses related to the converter are included in the model.
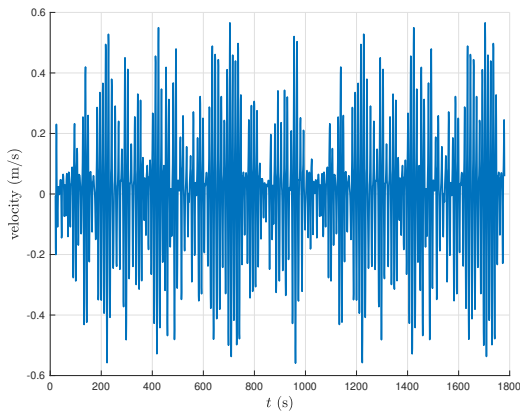
6.2.2 WEC velocity

From equation (2.11), it is known that the amount of absorbed power from the waves is dependent on the velocity of the WEC. In Figure 6.3, it can be noticed that there is not much difference between the absorbed power for the two control methods for S1 and S3, while for S2, PL absorbs more power than PC.

Comparing the amplitudes of the velocities in Figures 6.5-6.7, it can be seen that when PC is applied the WEC has a higher velocity than with PL for all sea states. This can easiest be seen in Figure 6.6. It can also be noticed that the WEC has the highest velocity for S2 and the lowest for S1. Looking at Figure 5.1, it can be seen that this can be related to the energy content in the sea states where S2 has the highest energy content around the resonance frequency of the floating body ($1.2 \, \mathrm{rad/s}$) and S1 has the lowest. From previous results, it can also be mentioned that a higher WEC velocity will result in more absorbed power. That S2 results in higher WEC velocities can therefore also be seen in the absorbed power in Figure 6.3.
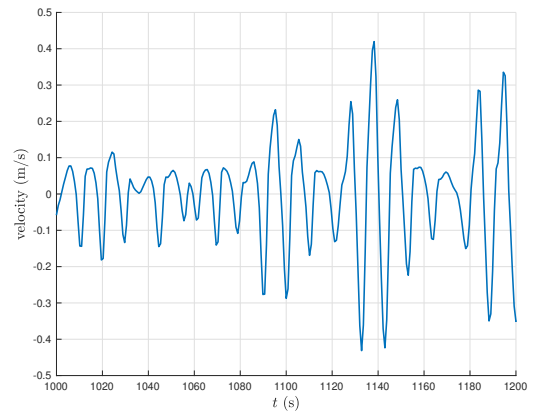
In general, the velocity of the WEC is very similar between the two control methods for all sea states. This means that by just looking at the WEC velocity, the absorbed power

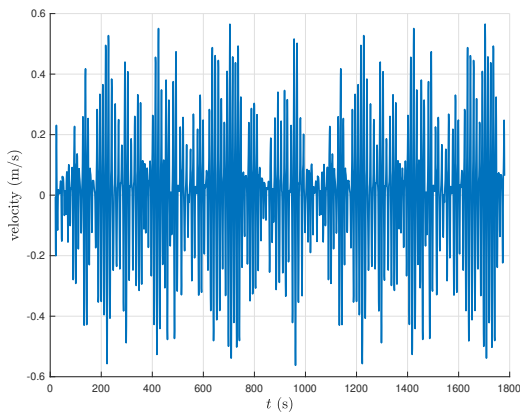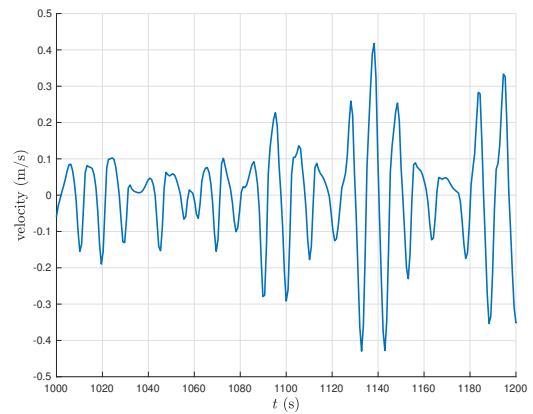should be approximately the same for PL and PC.

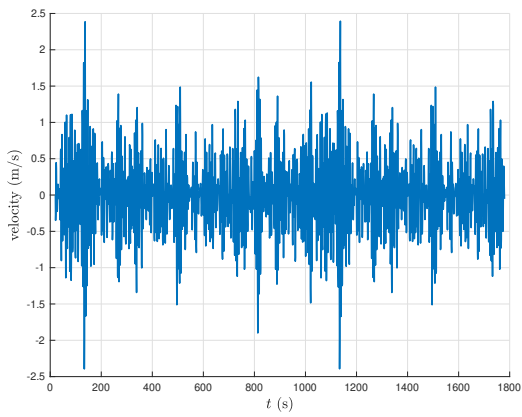**S1**

(a) PL

(b) PL

(c) PC

(d) PC

Figure 6.5: WEC velocity $\dot{x}(t)$ over the entire simulation time (subfigures a and c) and for the time interval 1000 s to 1200 s (subfigures b and d) for both control methods.
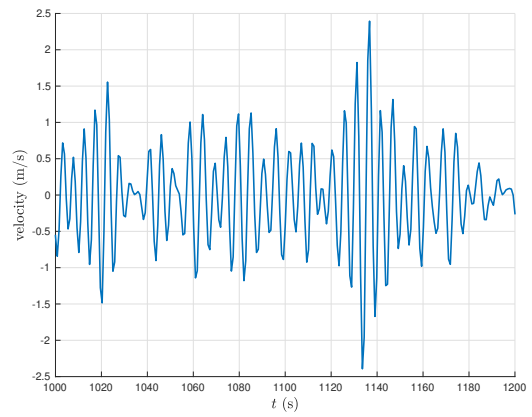
S2

(a) PL

(b) PL

(c) PC

(d) PC

Figure 6.6: WEC velocity $\dot{x}(t)$ over the entire simulation time (subfigures a and c) and for the time interval 1000 s to 1200 s (subfigures b and d) for both control methods.

S3

(a) PL

(b) PL

(c) PC

(d) PC

Figure 6.7: WEC velocity $\dot{x}(t)$ over the entire simulation time (subfigures a and c) and for the time interval 1000 s to 1200 s (subfigures b and d) for both control methods.
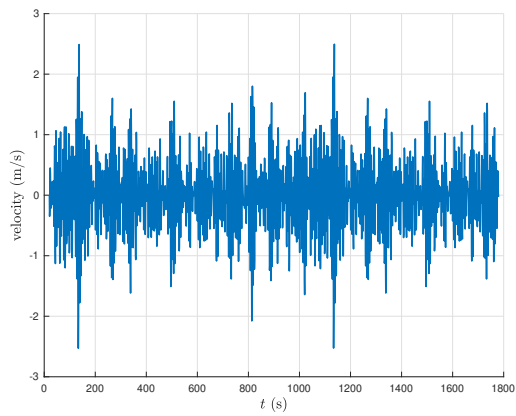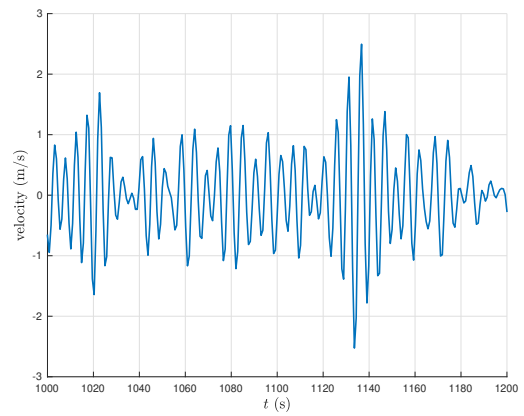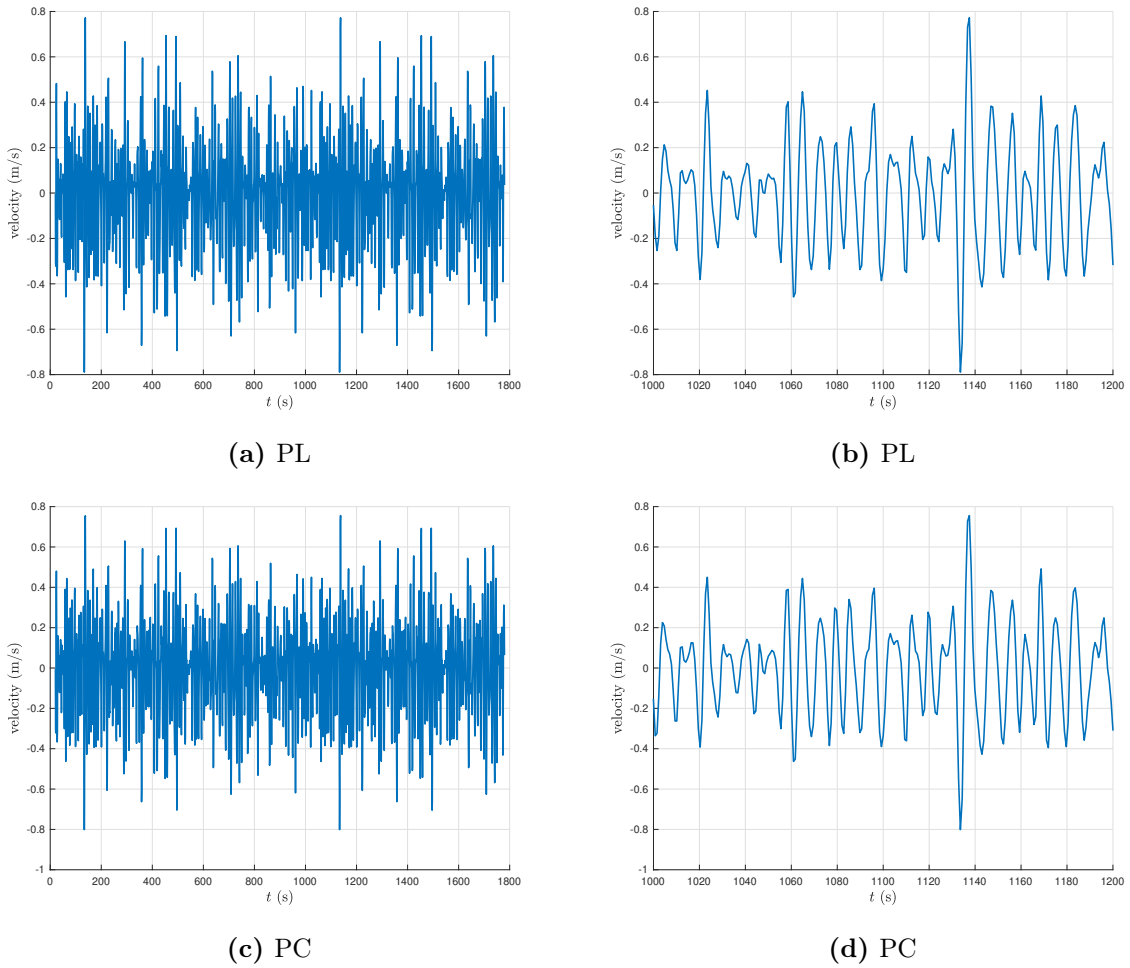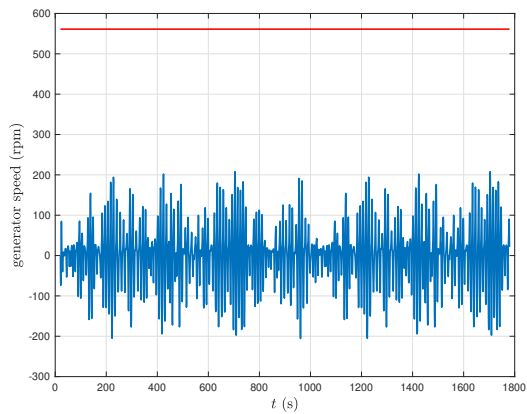
6.2.3 Generator speed

From the system description given in Section 1.2, it is know that the movement of the WEC is a direct cause of the rotation of the generator. By comparing Figures 6.5-6.7 with Figures 6.8-6.10 this can clearly be seen. As for the velocity, the generator speed is the highest for S2 and lowest for S1, where S2 also is the only sea state that produce high enough generator speeds to make field weakening necessary. It can also be seen that the generator speed is higher for PC than for PL, as it was for the WEC velocity. From equation (3.1) it is seen that the generator speed and WEC velocity are proportional. This means that whenever the velocity of the WEC increases so does the generator speed, which is seen in the comparison of the two variables.

As previously mentioned, the total power losses depend on the generator speed. Looking at the generator speed in Figures 6.8-6.10, it can be seen that the generator speed is very similar between PL and PC for all sea states. Even though the generator speed has a larger amplitude for PC than for PL, the differences are so small that they most likely will not cause much difference in the power losses related to the generator speed.

S1

(a) PL
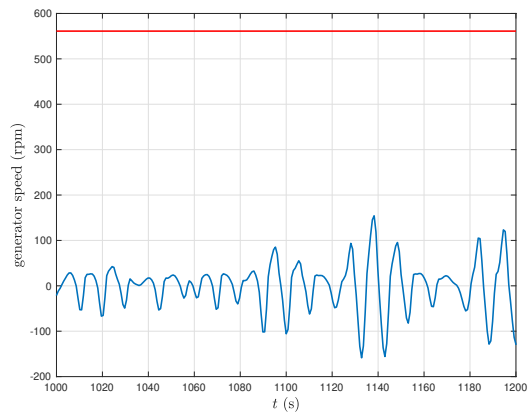
(b) PL
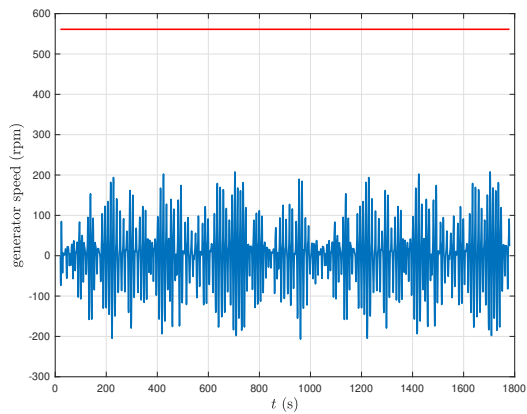
(c) PC

(d) PC

Figure 6.8: Generator speed ω_r over the entire simulation time (subfigures a and c) and for the time interval 1000 s to 1200 s (subfigures b and d) for both control methods. The red line represent the field weakening speed.

S2

(a) PL

(b) PL

(c) PC

(d) PC

Figure 6.9: Generator speed ω_r over the entire simulation time (subfigures a and c) and for the time interval 1000 s to 1200 s (subfigures b and d) for both control methods. The red line represent the field weakening speed.
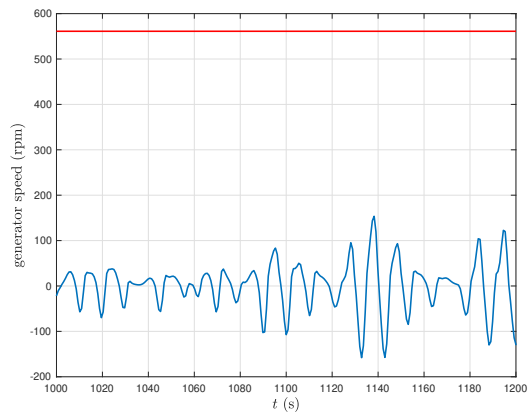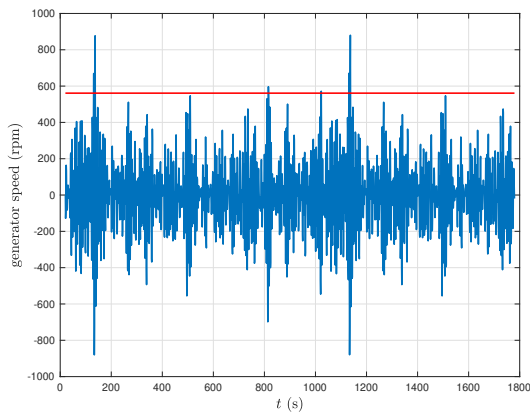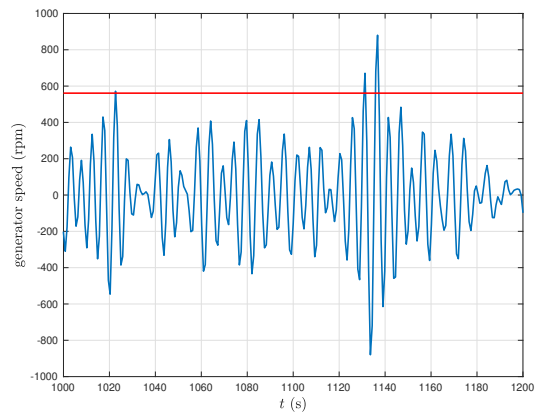
S3

(a) PL

(b) PL

(c) PC

(d) PC

Figure 6.10: Generator speed ω_r over the entire simulation time (subfigures a and c) and for the time interval 1000 s to 1200 s (subfigures b and d) for both control methods. The red line represent the field weakening speed.
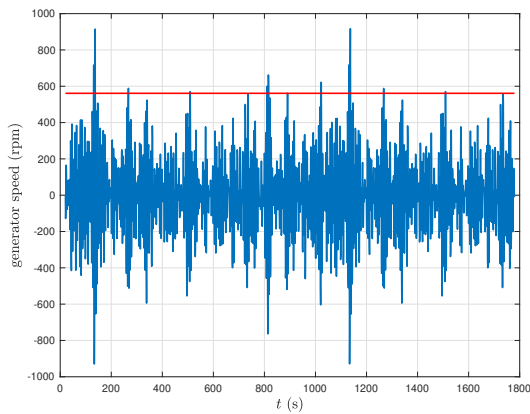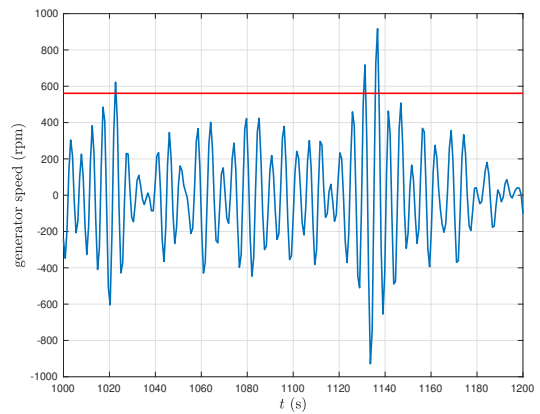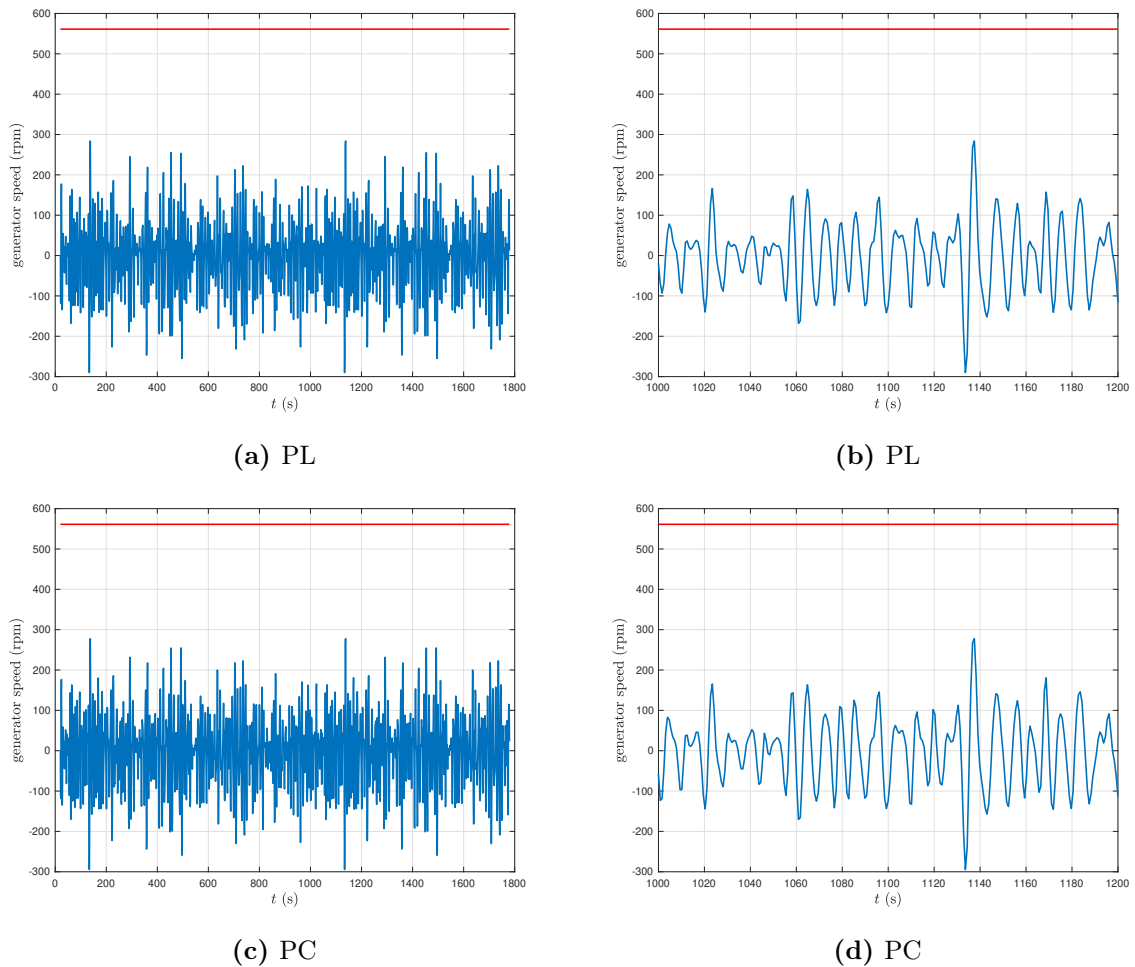
6.2.4 Generator torque

From equations (3.21) and (2.9), it is known that the reference torque depends on the velocity of the WEC and the PTO damping. Comparing the shape of the reference torque for PL and PC in Figures 6.11-6.13, it can be noticed that there are some differences in both the shape and amplitudes of the reference torque, where PC generates larger amplitudes than PL. Since PL has a constant damping, the dependence on the velocity can mainly be seen through the shape of the reference torque, while for PC the shape of the reference torque can not be directly connected to the velocity because of the varying PTO damping. From Subsection 6.2.2 it is known that the WEC velocity is very similar between the two control methods, this means that the difference between the reference torque is mainly related to the PTO damping. This will further be discussed in Subsection 6.2.8.

In Figures 6.11-6.13, it can be noticed that there is a large difference between the reference torque and the measured torque. As a result, the measured torque switches very much between its maximum and minimum values, i.e., the electric PTO system is working at

the boundary of its capacity and not closer to nominal values. The high torque values can be related to the energy content of the given sea state. Sea states with a very high energy content results in higher reference torques, as indicated by equation (3.21). From the corresponding figures, it can also be seen that the measured torque follows the reference torque well for regions with no torque limitations, which means that the torque control works adequately.

S1

(a) PL

(b) PL

(c) PC

(d) PC
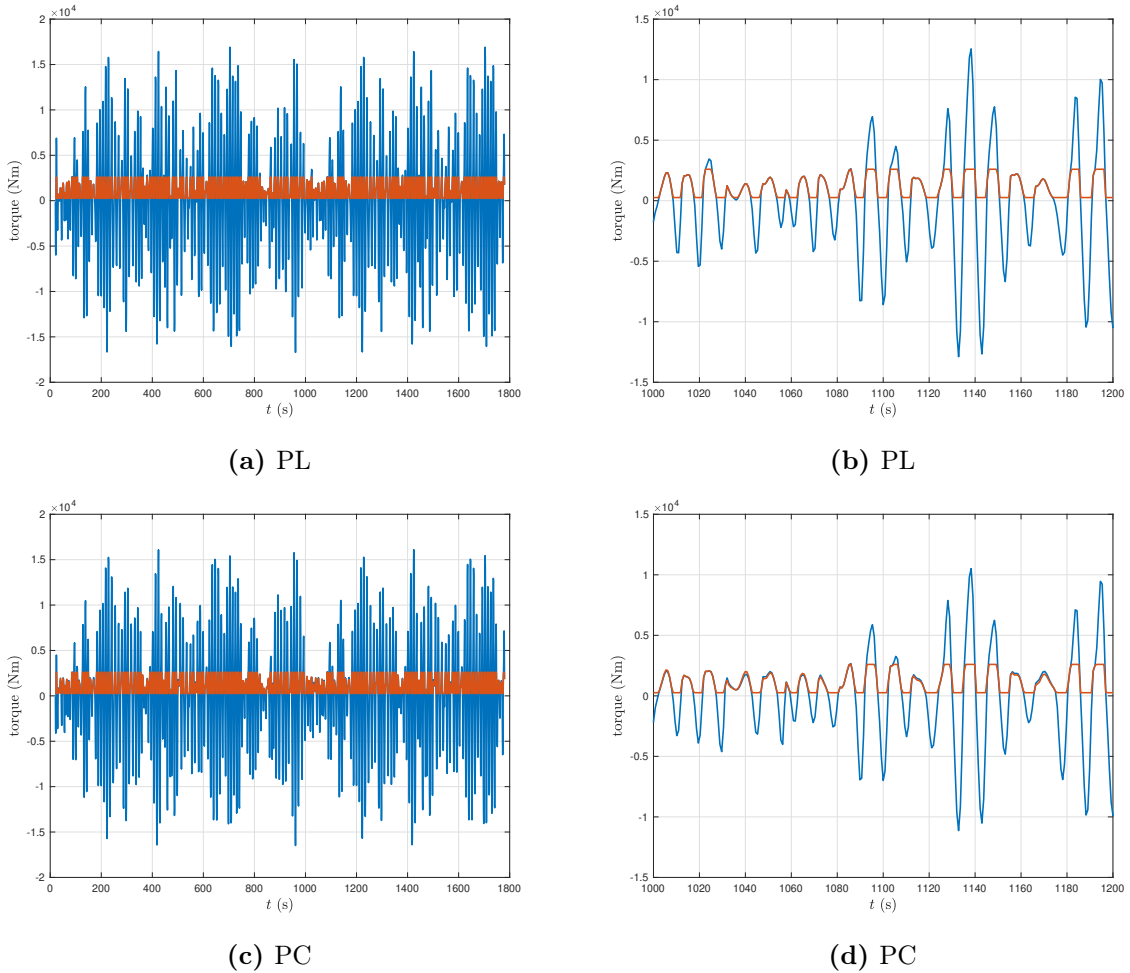
Figure 6.11: Reference $T_{e,ref}$ and measured T_e torque over the entire simulation time (subfigures a and c) and for the time interval 1000 s to 1200 s (subfigures b and d) for both control methods.

S2

(a) PL
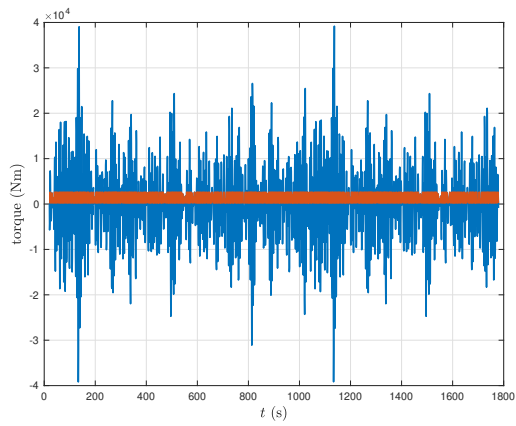
(b) PL

(c) PC

(d) PC

Figure 6.12: Reference $T_{e,ref}$ and measured T_e torque over the entire simulation time (subfigures a and c) and for the time interval 1000 s to 1200 s (subfigures b and d) for both control methods.

S3

(a) PL

(b) PL

(c) PC

(d) PC

Figure 6.13: Reference $T_{e,ref}$ and measured T_e torque over the entire simulation time (subfigures a and c) and for the time interval 1000 s to 1200 s (subfigures b and d) for both control methods.
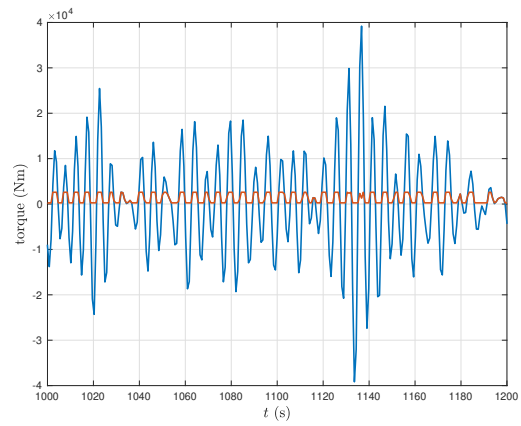
In Subsection 6.2.1, the dependence the electrical torque has on the power losses was mentioned. From Table 6.2, it can be seen that PL results in more power losses than PC. This can be related to the difference in the measured torque. In Figures 6.14-6.16, it can be noticed that the torque values are higher for PL than PC, this can especially be seen for S3 in Figure 6.16. The reason why PL gives higher torque values are related to the reference torque. For PC, the PTO damping adapts to each individual wave, which results in more oscillations in the reference torque, while PL has a more constant oscillation. This results in that some places, for instance between 1160 s and 1180 s in Figure 6.13, the reference torque is smaller for PC than PL resulting in smaller torque values.

S1

(a) PL
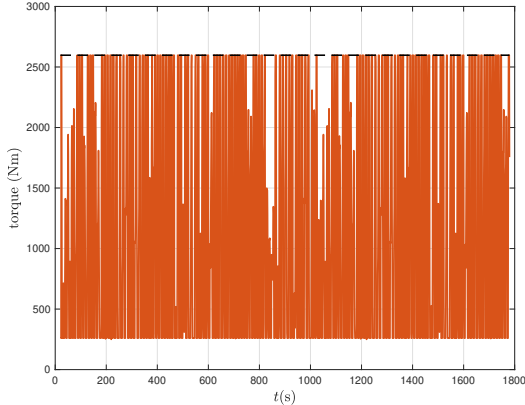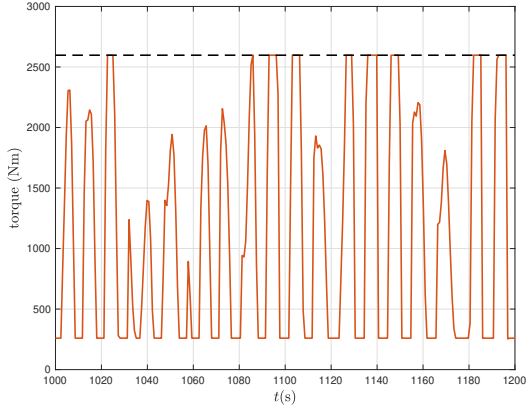
(b) PL
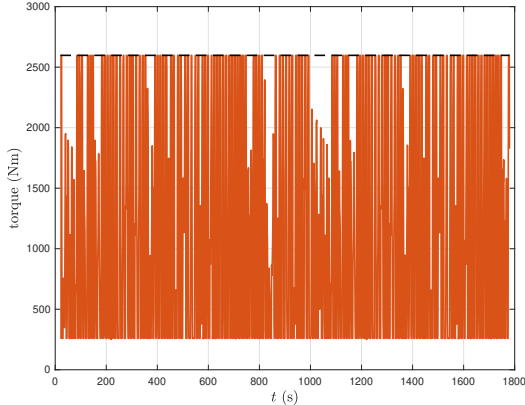
(c) PC
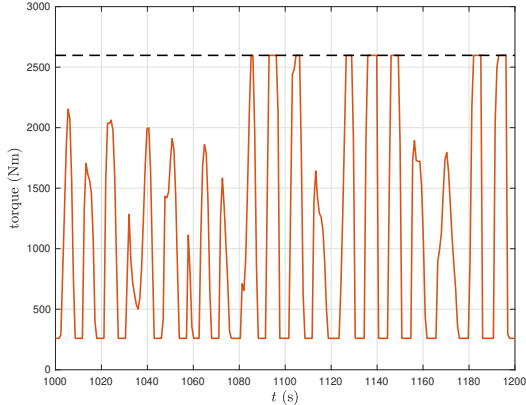
(d) PC

Figure 6.14: Measured torque T_e over the entire simulation time (subfigures a and c) and for the time interval 1000 s to 1200 s (subfigures b and d) for both control methods.
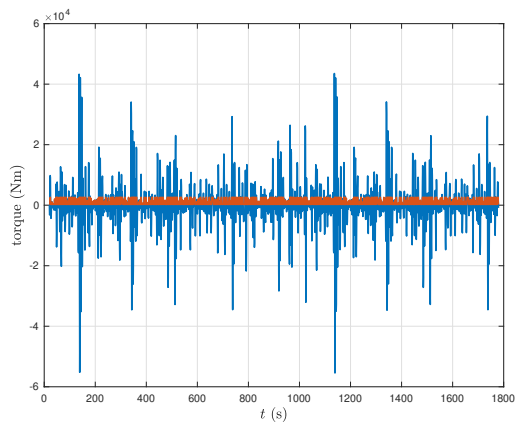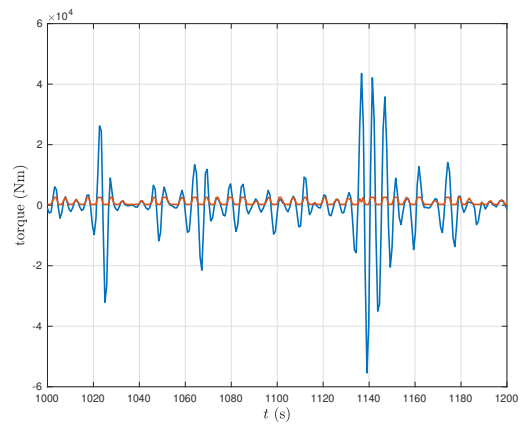
S2

(a) PL

(b) PL

(c) PC

(d) PC

Figure 6.15: Measured torque T_e over the entire simulation time (subfigures a and c) and for the time interval 1000 s to 1200 s (subfigures b and d) for both control methods.
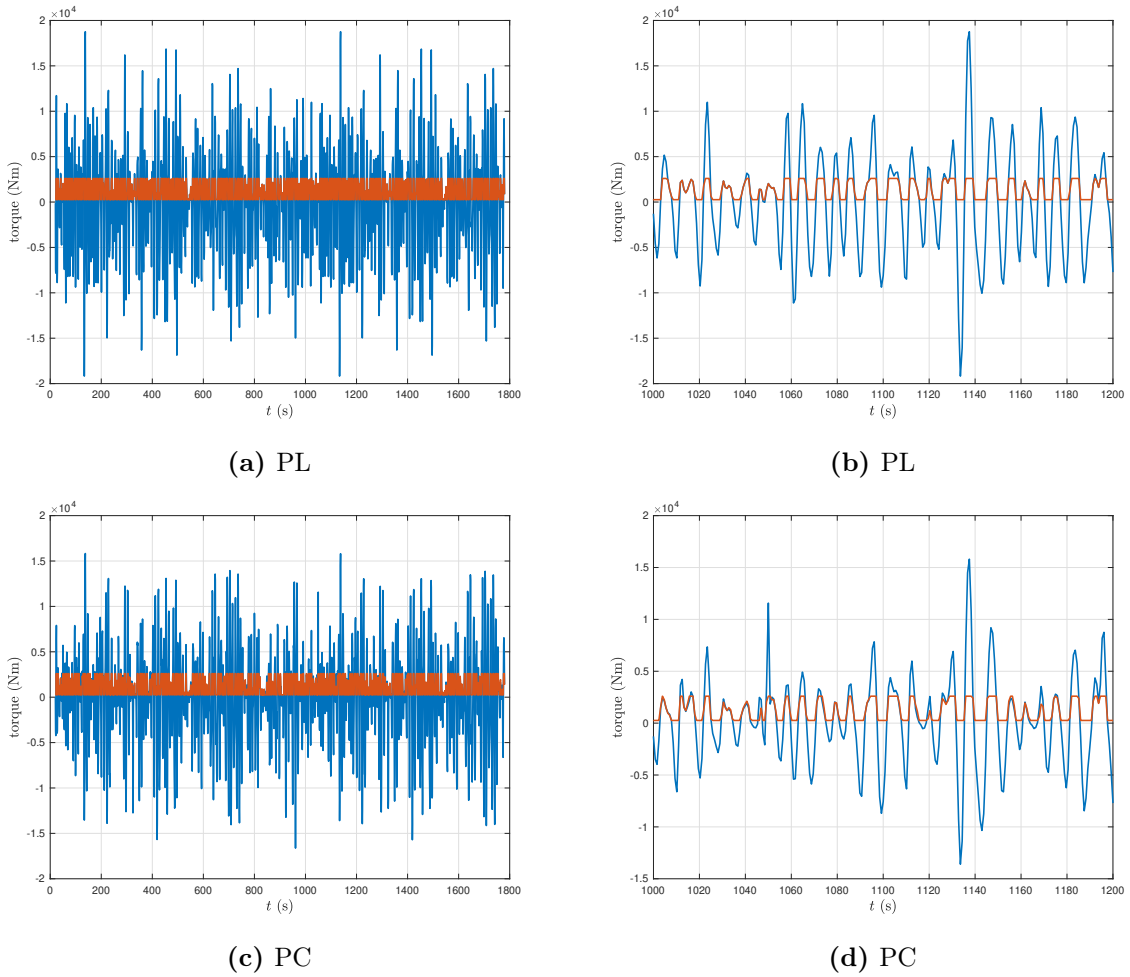
S3

(a) PL

(b) PL

(c) PC

(d) PC

Figure 6.16: Measured torque T_e over the entire simulation time (subfigures a and c) and for the time interval 1000 s to 1200 s (subfigures b and d) for both control methods.
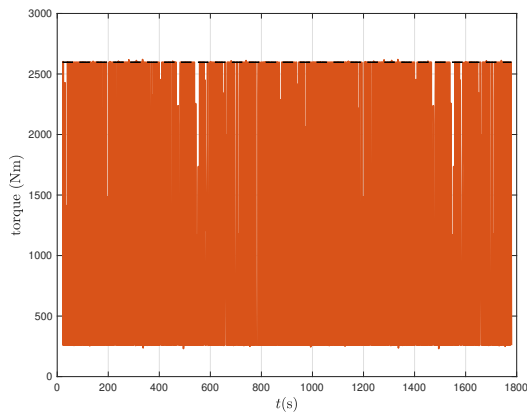
6.2.5   D- and q-axis voltages

First, the d-axis voltages for the two control methods, illustrated in Figures 6.17, 6.19, and 6.21, can be discussed. The d-axis voltage u_d is very similar between the two control methods for all sea states. The main difference lies in the amplitudes of the oscillations. Looking closer at the figures, it can be noticed that the amplitudes when PL is applied are mostly higher than when PC is applied. From equation (3.2), it is known that the d-axis voltage depends on the d- and q-axis currents and the generator speed. Due to the resulting size of each part in the expression, the dominant part is related to the generator speed ω_r and the q-axis current i_q. Previously, it has been shown that the generator speeds for each control method are very similar, although PC gives a slightly higher speed. This means that the main difference in u_d lies with i_q. As can be seen in Figures 6.25, 6.27, and 6.29, i_q is averagely higher for PL than for PC, which results in that u_d will get larger amplitudes for PL than PC.

Now, the q-axis voltages u_q can be compared. Looking at Figures 6.18, 6.20, and 6.22, the main difference between the q-axis voltages is the oscillation, where PC results in more oscillations in u_q than PL. Looking only at the expression for u_q in equation (3.3),

PL should result in higher values for u_q than when PC is applied since there is more q-current for PL than for PC. However, due to the spikes in u_q for PC, the average value for u_q becomes higher for PC than for PL. The oscillations and the spikes for PC is a direct cause of the HHT method and the constant changing of the tuning frequency on a wave-to-wave basis, which will be discussed in Subsection 6.2.9.
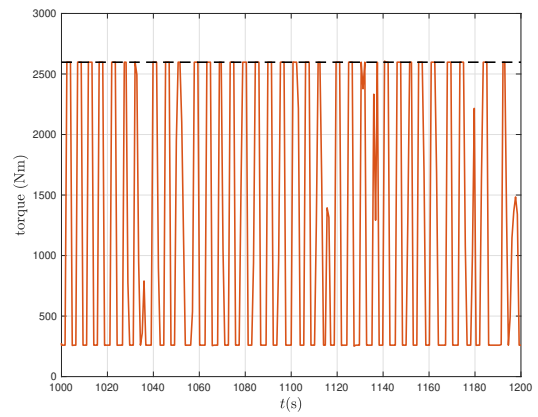
S1

(a) PL

(b) PL

(c) PC

(d) PC

Figure 6.17: D-axis voltage u_d over the entire simulation time (subfigures a and c) and for the time interval 1000 s to 1200 s (subfigures b and d) for both control methods.
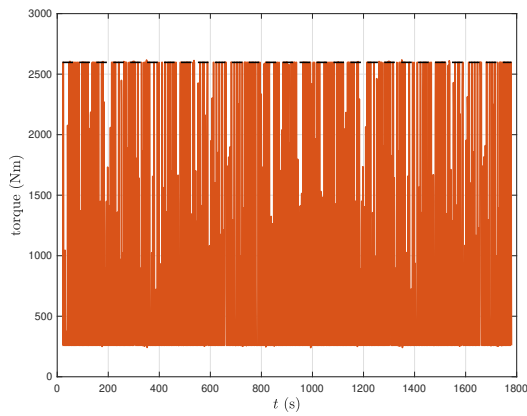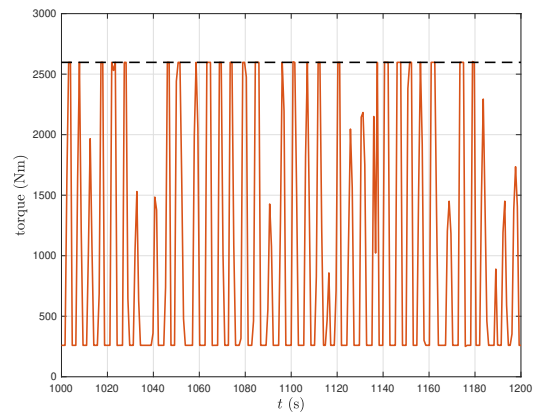
S1

(a) PL
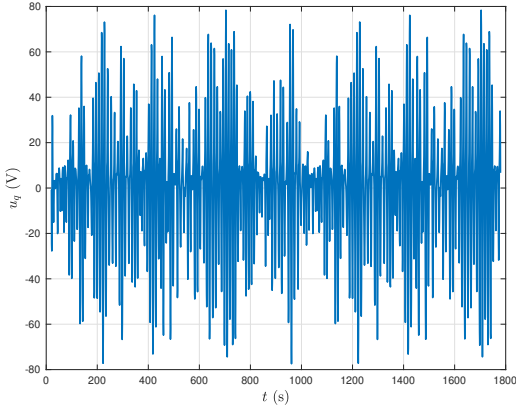
(b) PL

(c) PC

(d) PC

Figure 6.18: Q-axis voltage u_q over the entire simulation time (subfigures a and c) and for the time interval 1000 s to 1200 s (subfigures b and d) for both control methods.
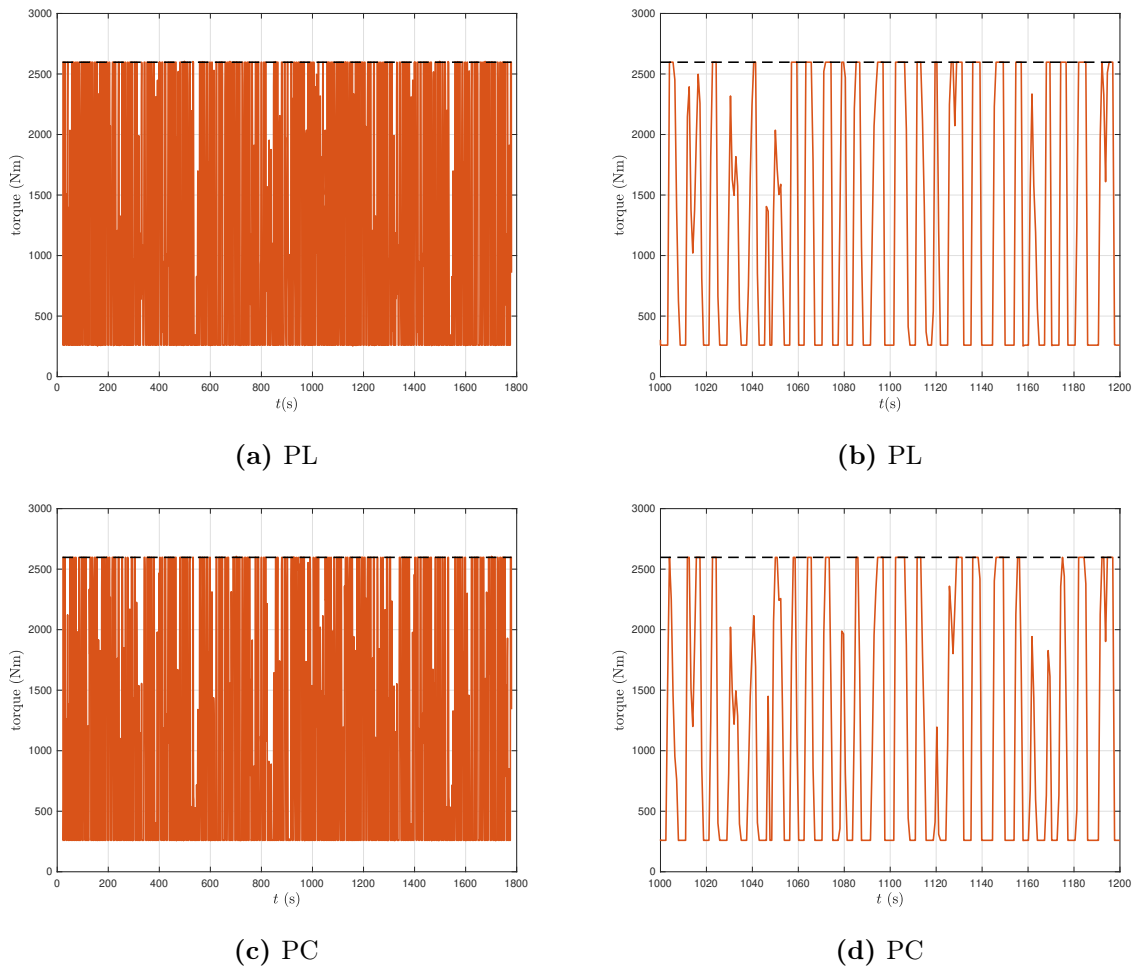
S2

(a) PL

(b) PL

(c) PC

(d) PC

Figure 6.19: D-axis voltage u_d over the entire simulation time (subfigures a and c) and for the time interval 1000 s to 1200 s (subfigures b and d) for both control methods.
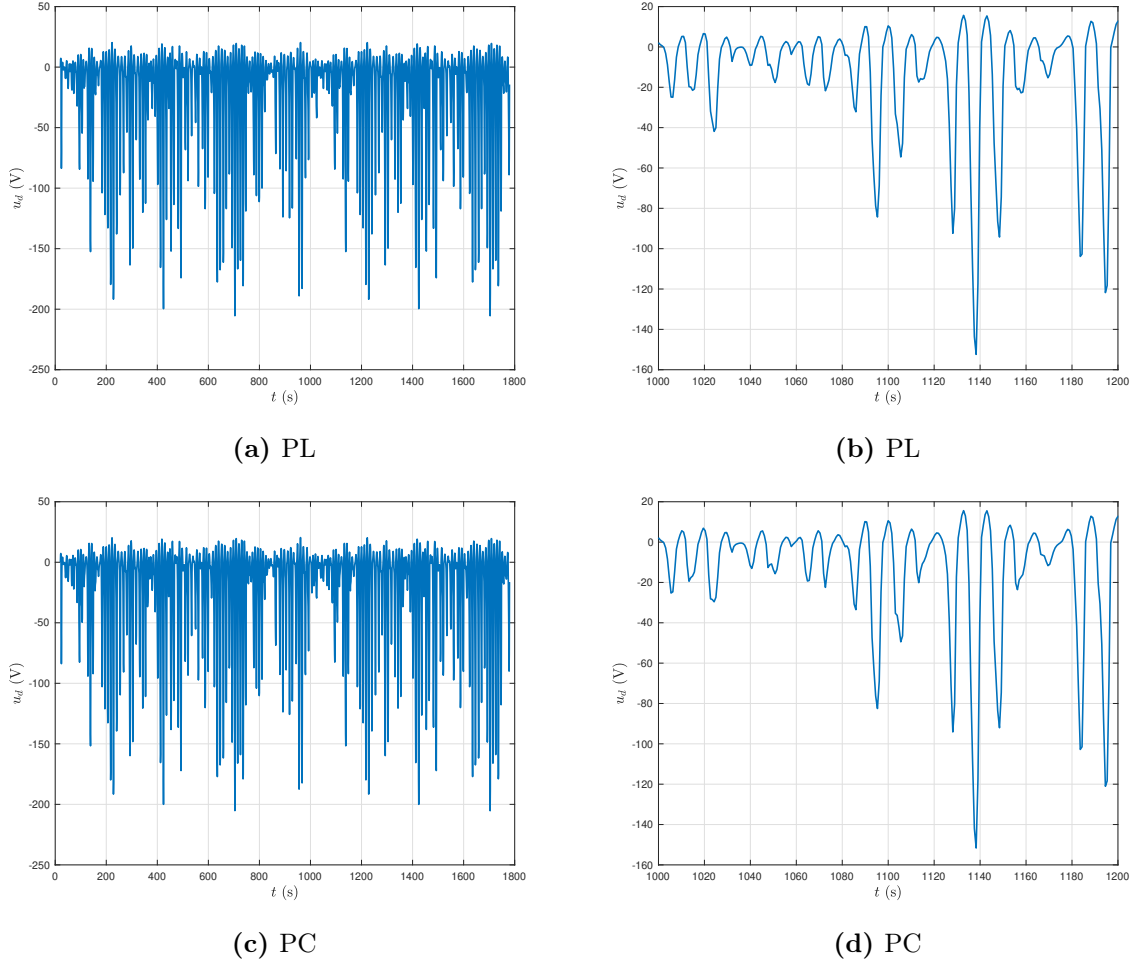
S2

(a) PL

(b) PL
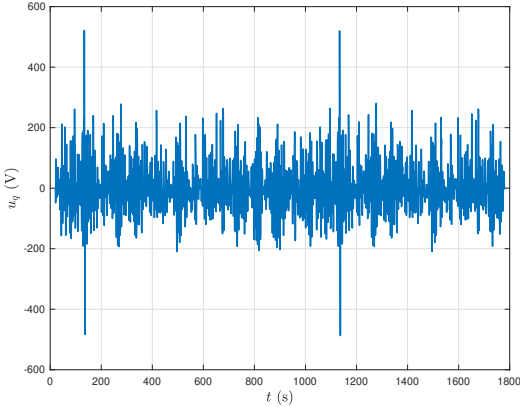
(c) PC
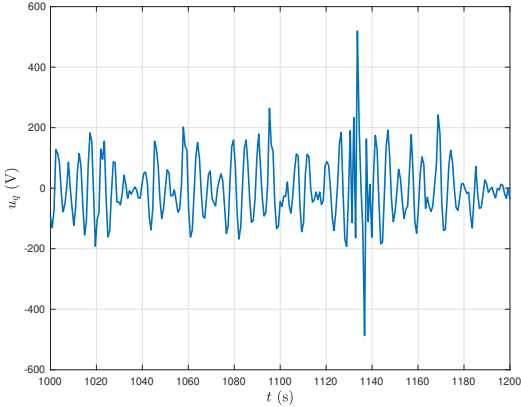
(d) PC

Figure 6.20: Q-axis voltage u_q over the entire simulation time (subfigures a and c) and for the time interval 1000 s to 1200 s (subfigures b and d) for both control methods.

S3

(a) PL
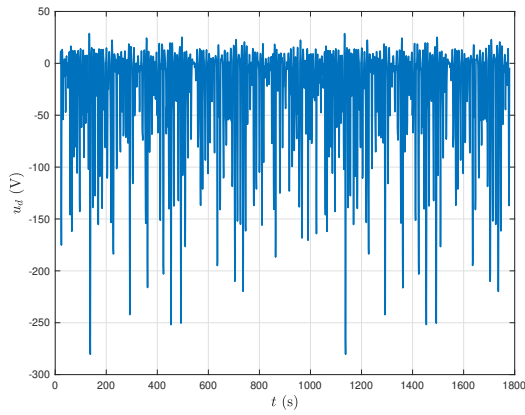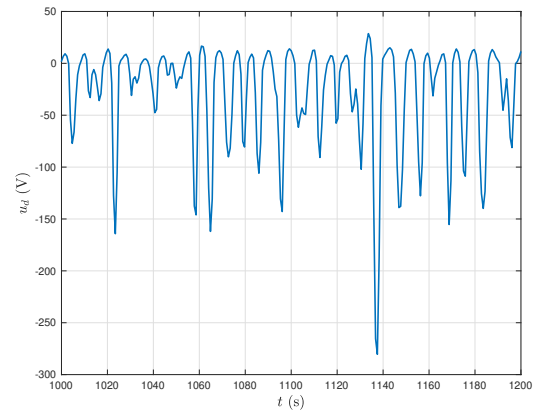
(b) PL

(c) PC

(d) PC

Figure 6.21: D-axis voltage u_d over the entire simulation time (subfigures a and c) and for the time interval 1000 s to 1200 s (subfigures b and d) for both control methods.

S3

(a) PL

(b) PL

(c) PC

(d) PC

Figure 6.22: Q-axis voltage u_q over the entire simulation time (subfigures a and c) and for the time interval 1000 s to 1200 s (subfigures b and d) for both control methods.

In Figure 6.23, both u_q and u_d have been plotted along with the WEC velocity for S1. There it can be noticed that u_q follows the velocity while u_d is the opposite. This can be explained through the expression for the d- and q-axis voltages in equations (3.2) and (3.3). As discussed earlier, the dominant part of the voltage expressions are dependent on the generator speed. From the way u_d is defined, the voltage will be positive when the speed is negative and negative when the speed is positive. For u_q, the voltage will be positive for positive speeds and so on. This also means that for higher generator speeds, more voltage will be induced, i.e., higher u_d and u_q values.

S1

(a) PL

(b) PC
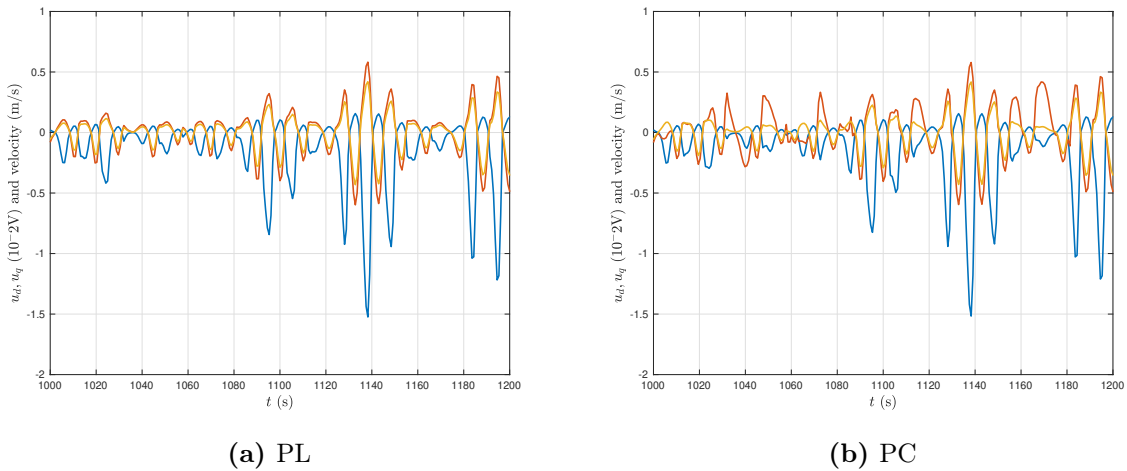
Figure 6.23: WEC velocity $\dot{x}(t)$ (yellow), u_d (blue) and u_q (red) over the time interval 1000 s to 1200 s for PL (subfigure a) and PC (subfigure b).

6.2.6   D- and q-axis currents

Comparing Figures 6.25, 6.27, and 6.29 with Figures 6.14-6.16, it can be seen that the squared oscillations seen in the torque T_e can also be observed in the q-current i_q. As seen in equations (3.7) and (3.20), the torque is proportional to the q-current. Because of this, the power losses are also indirectly related to i_q. From Figure 6.4, it is seen that PL results in higher power losses. As seen in Figures 6.25, 6.27, and 6.29, PL also results in higher i_q values. Physically, a higher i_q will result in an increased stator current which will give more copper losses in the generator, which corresponds to the power loss results.

As previously mentioned, PL results in higher q-axis current values than PC. The q-axis current is found based on the reference q-axis current, which is dependent on the torque reference, as seen in equation (3.20). Due to the proportionality between i_q and T_e, i_q will reach its maximum value when T_e does. Since PL has higher measured torque values, PL also will have higher i_q values. When field weakening is applied, the q-current is also calculated with a part consisting of the negative multiplication of the generator speed and d-current. Since both of these values are smaller for PL than for PC, the resulting i_q will become higher for PL than for PC during field weakening as well.

S1

(a) PL
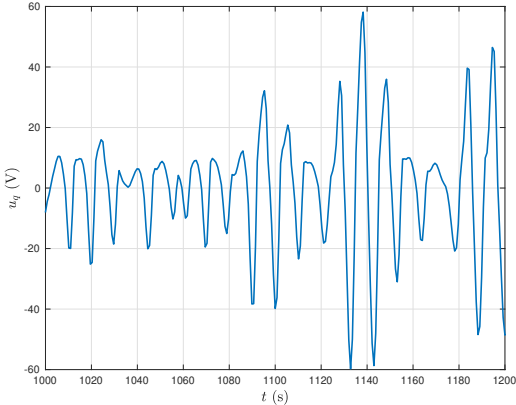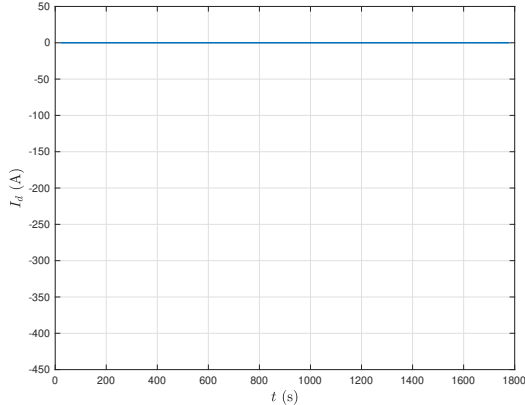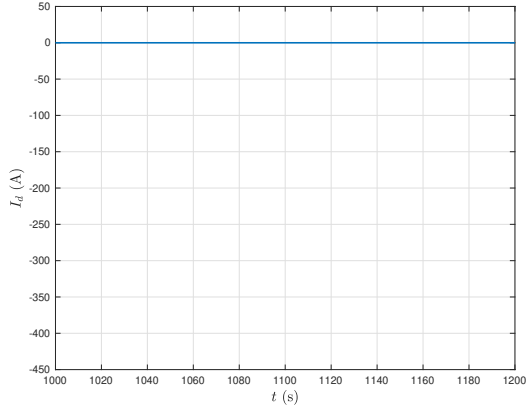

(b) PL
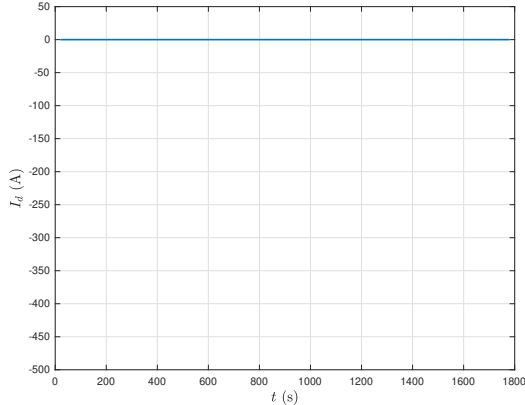
(c) PC
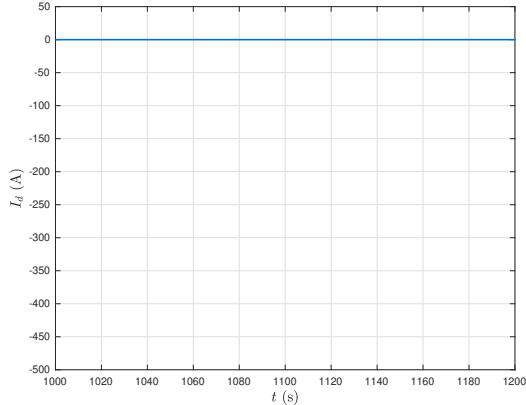
(d) PC

Figure 6.24: D-axis current i_d over the entire simulation time (subfigures a and c) and for the time interval 1000 s to 1200 s (subfigures b and d) for both control methods.
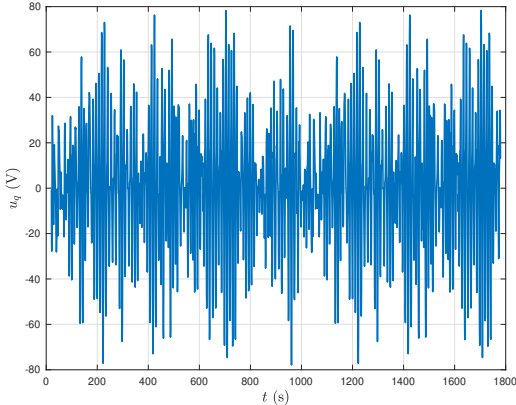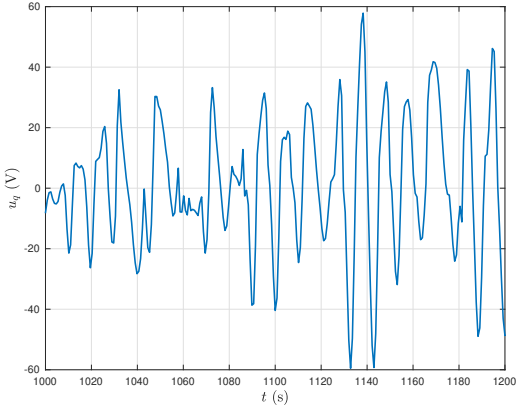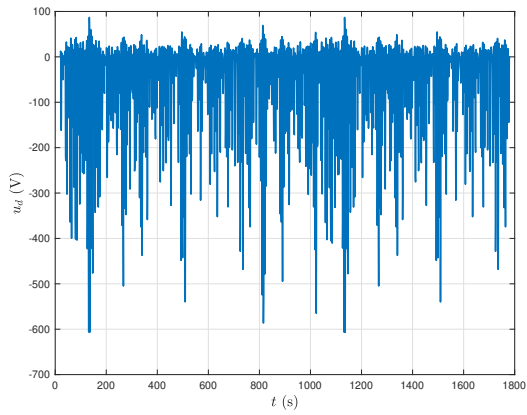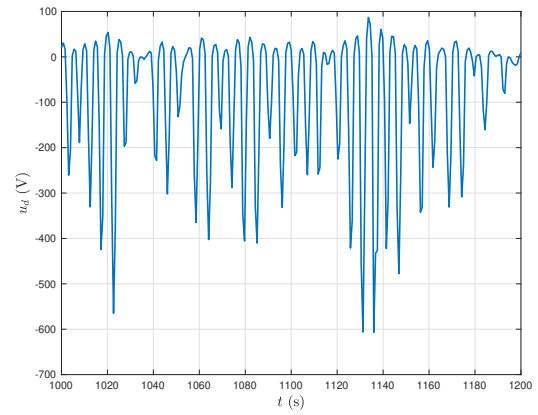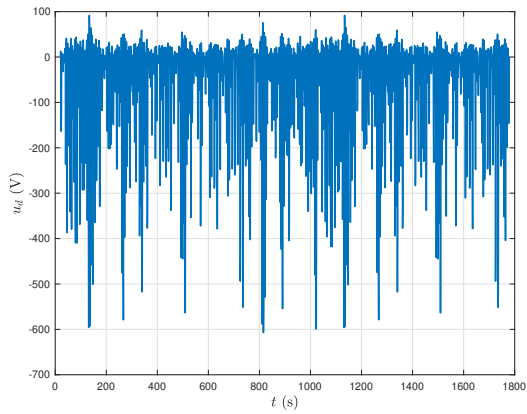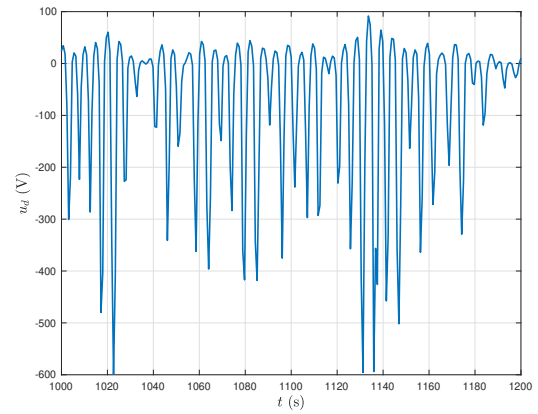
S1

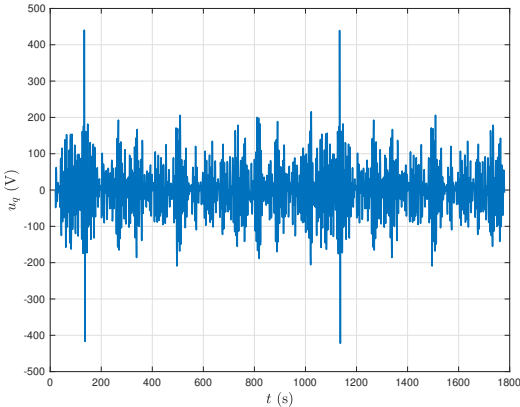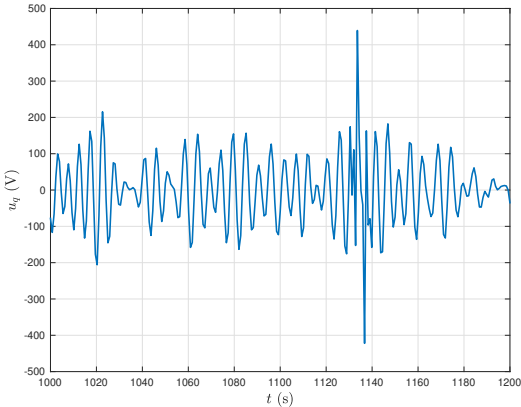**(a)** PL

(b) PL

(c) PC

(d) PC
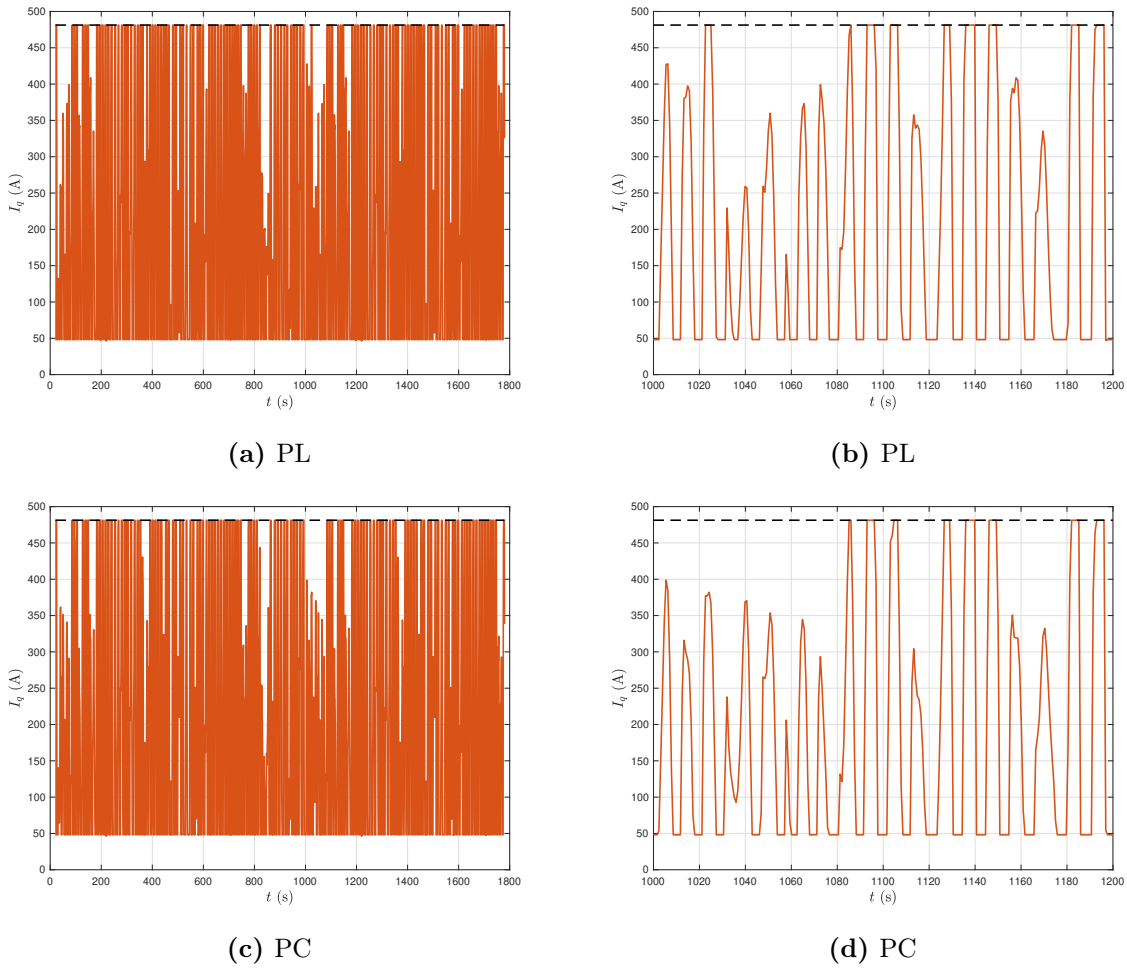
Figure 6.25: Q-axis current i_q over the entire simulation time (subfigures a and c) and for the time interval 1000 s to 1200 s (subfigures b and d) for both control methods.

In Figure 6.26, it can be seen that S2 is the only sea state that results in field weakening. For the two other sea states, i_d is constantly zero, as seen in Figures 6.24 and 6.28. In Figure 6.26, it can also be noticed that field weakening is needed more often for PC than for PL. This is related to the way the current controller is designed and the generator speed. From Figure 3.4, it can be seen that it is the generator speed that ultimately decides whether or not field weakening is applied. Field weakening happens only if the q-axis reference current is outside of its boundaries and the generator speed is larger than the field weakening speed. So, if the generator speed is higher, the field weakening speed will more often be reached. When field weakening is applied, it can also be noticed that there is more negative d-current for PC than for PL. Field weakening is used to operate the generator at higher speeds than the rated speed by introducing a negative d-current. Hence, more negative d-current is needed in order to operate at higher generator speeds.

S2

(a) PL
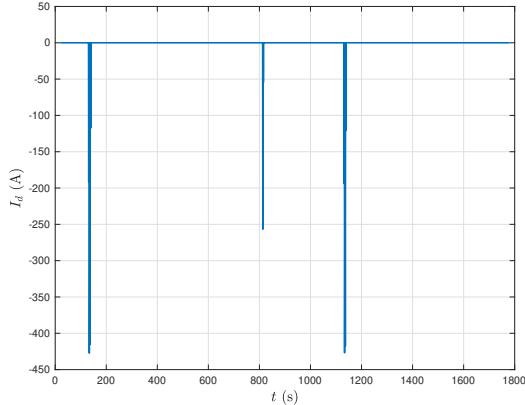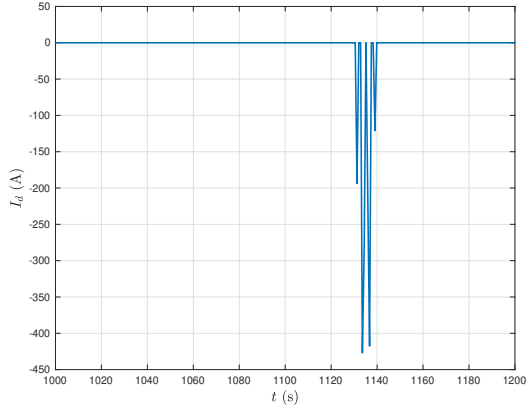
(b) PL
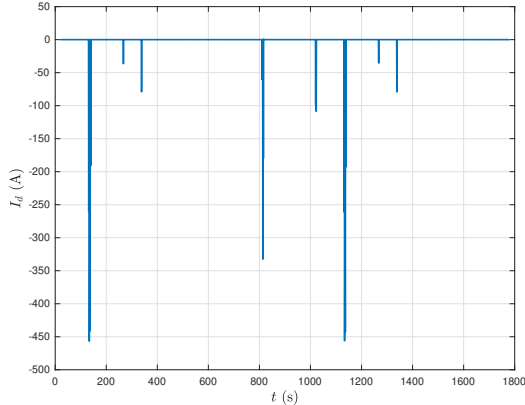
(c) PC
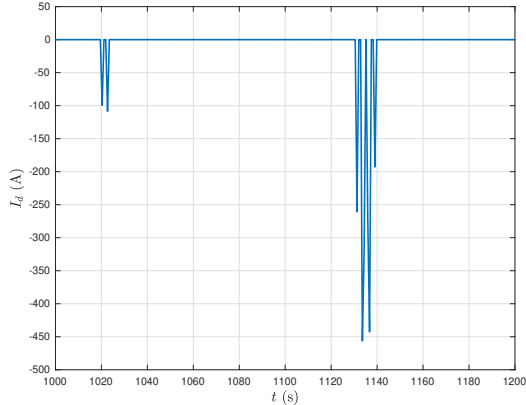
(d) PC

Figure 6.26: D-axis current i_d over the entire simulation time (subfigures a and c) and for the time interval 1000 s to 1200 s (subfigures b and d) for both control methods.
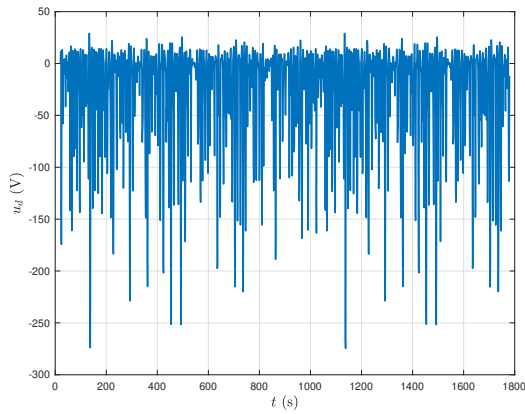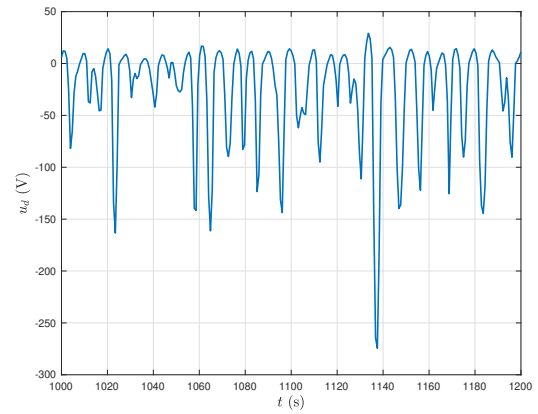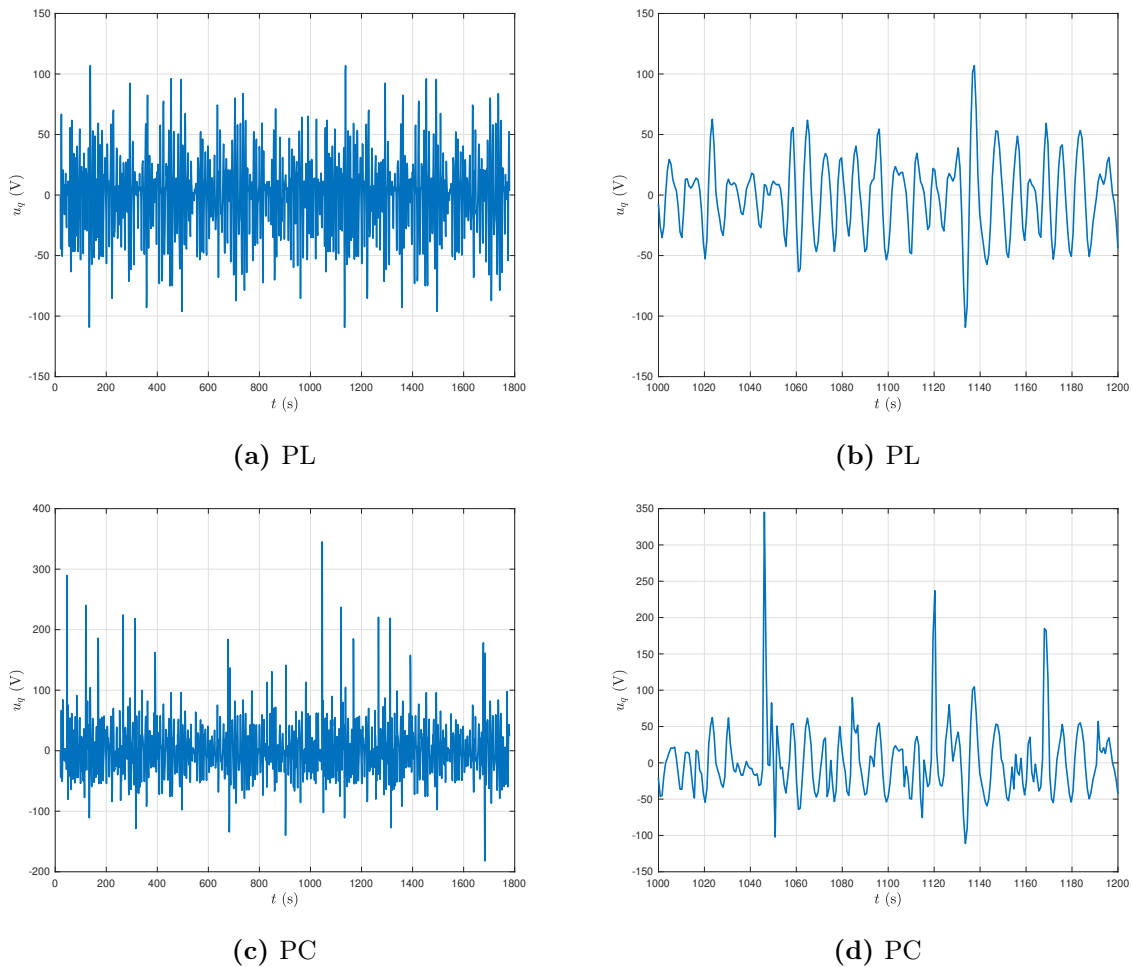
S2

(a) PL
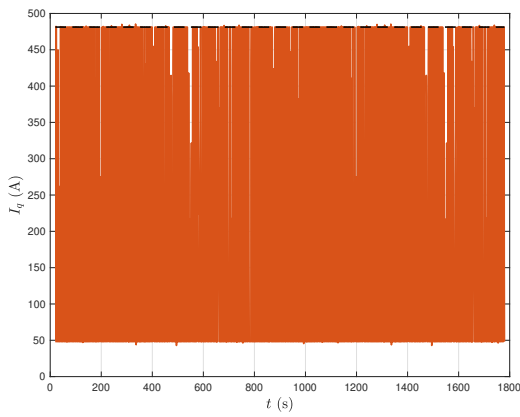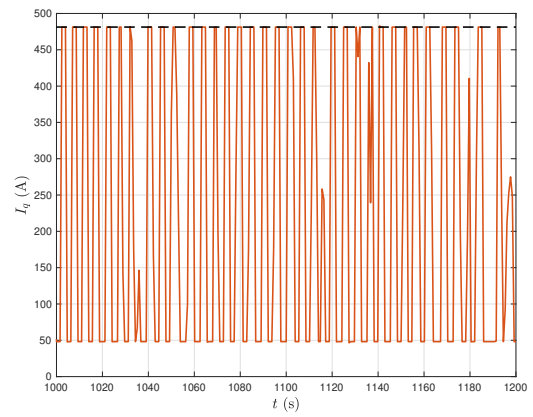
(b) PL
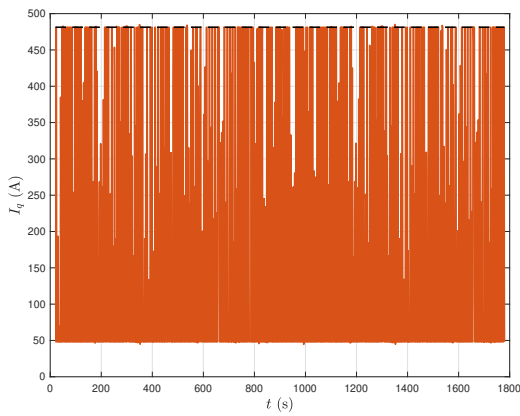
(c) PC
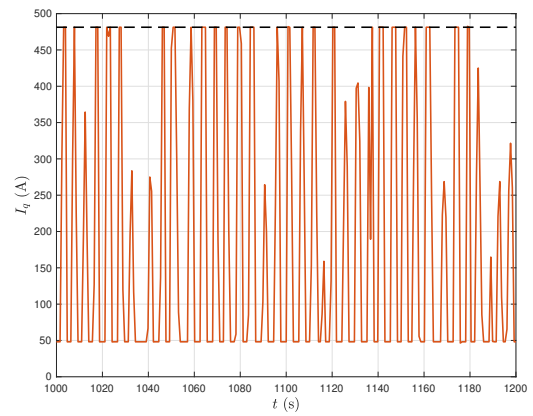
(d) PC

Figure 6.27: Q-axis current i_q over the entire simulation time (subfigures a and c) and for the time interval 1000 s to 1200 s (subfigures b and d) for both control methods.

S3

(a) PL
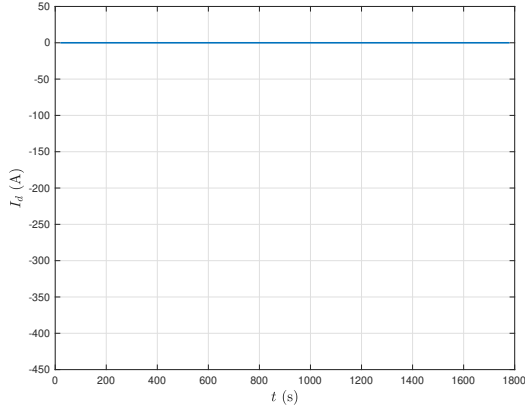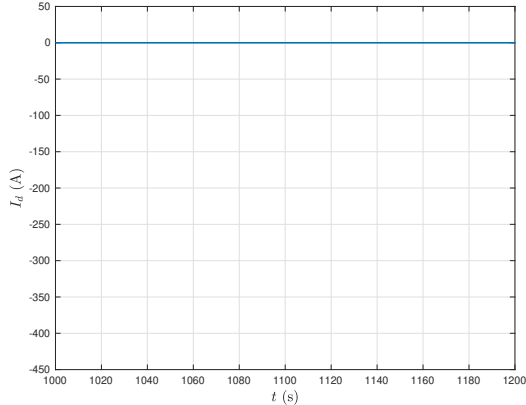
(b) PL
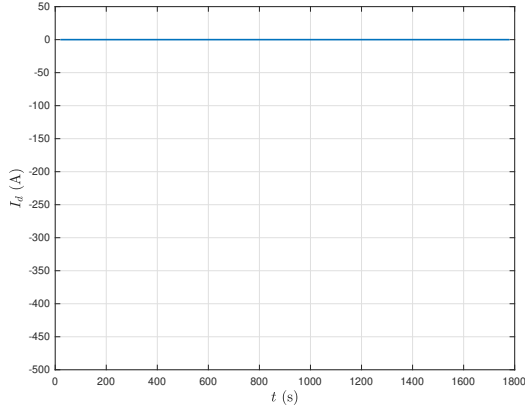
(c) PC
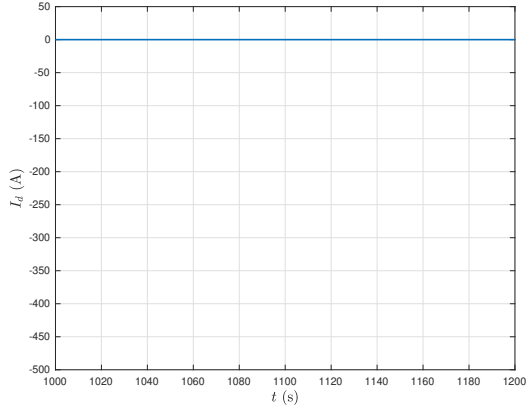
(d) PC

Figure 6.28: D-axis current i_d over the entire simulation time (subfigures a and c) and for the time interval 1000 s to 1200 s (subfigures b and d) for both control methods.

S3

(a) PL

(b) PL

(c) PC

(d) PC
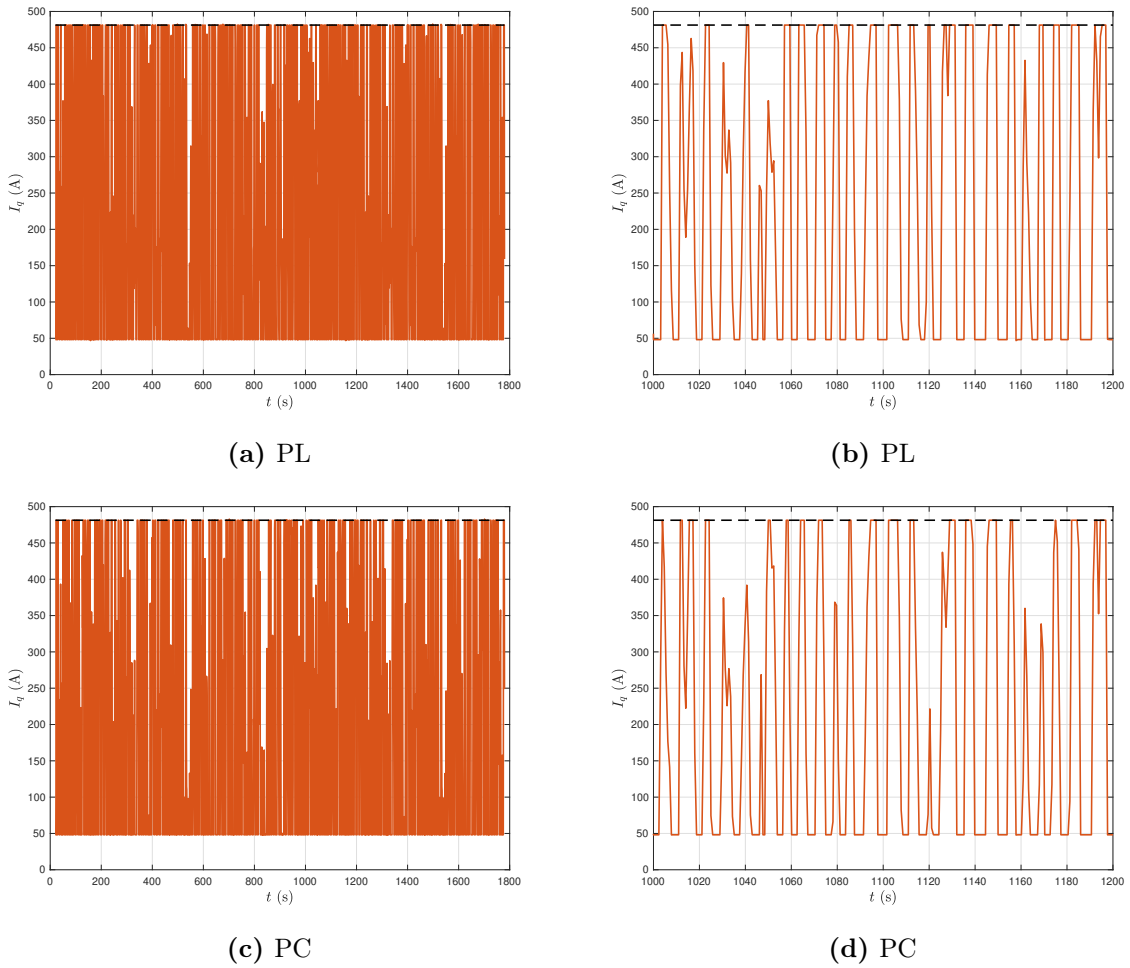
Figure 6.29: Q-axis current i_q over the entire simulation time (subfigures a and c) and for the time interval 1000 s to 1200 s (subfigures b and d) for both control methods.

6.2.7 Instantaneous powers

A significant difference between the control methods is the large negative peaks in the instantaneous mechanical and electrical power seen in the PC results in Figures 6.30-6.32. These peaks are the reason why the average negative mechanical and electrical power in Figures 6.3 and 6.4 are around twice as high for PC than for PL. Comparing, for example, the large negative peaks in Figure 6.30d with u_q in Figure 6.18d for PC, it can be seen that the negative peaks happen when there are fast oscillations in u_q. These oscillations are related to the tuning frequency, which will be discussed in Subsection 6.2.9.

As previously explained, during the periods when the WEC velocity is negative, power is drawn from the grid in order to maintain tension in the mooring line. From the electrical power results in Figure 6.4 and the instantaneous power results in Figures 6.30-6.32, it is seen that PC needs a lot more power from the grid in order to maintain tension in the rope.

From the system description, it is know that the amount of absorbed power is connected to the WEC velocity. This can easily be seen by comparing the WEC velocities in Figures 6.5-6.7 with the instantaneous powers in Figures 6.30-6.32. As expected, whenever the

velocity is negative, the instantaneous mechanical power is also negative. It can also be seen that a higher WEC velocity gives more mechanical power. From the previous discussion on the WEC velocity, it is known that the WEC velocity is higher for PC than for PL. This can also be seen in the results for the instantaneous powers, where PC gets higher positive amplitudes in the instantaneous mechanical power, and thus absorbs more power, than PL. From Table 6.2, this behavior can also be seen in the ratio of the average positive electrical power.

S1

(a) PL

(b) PL

(c) PC

(d) PC
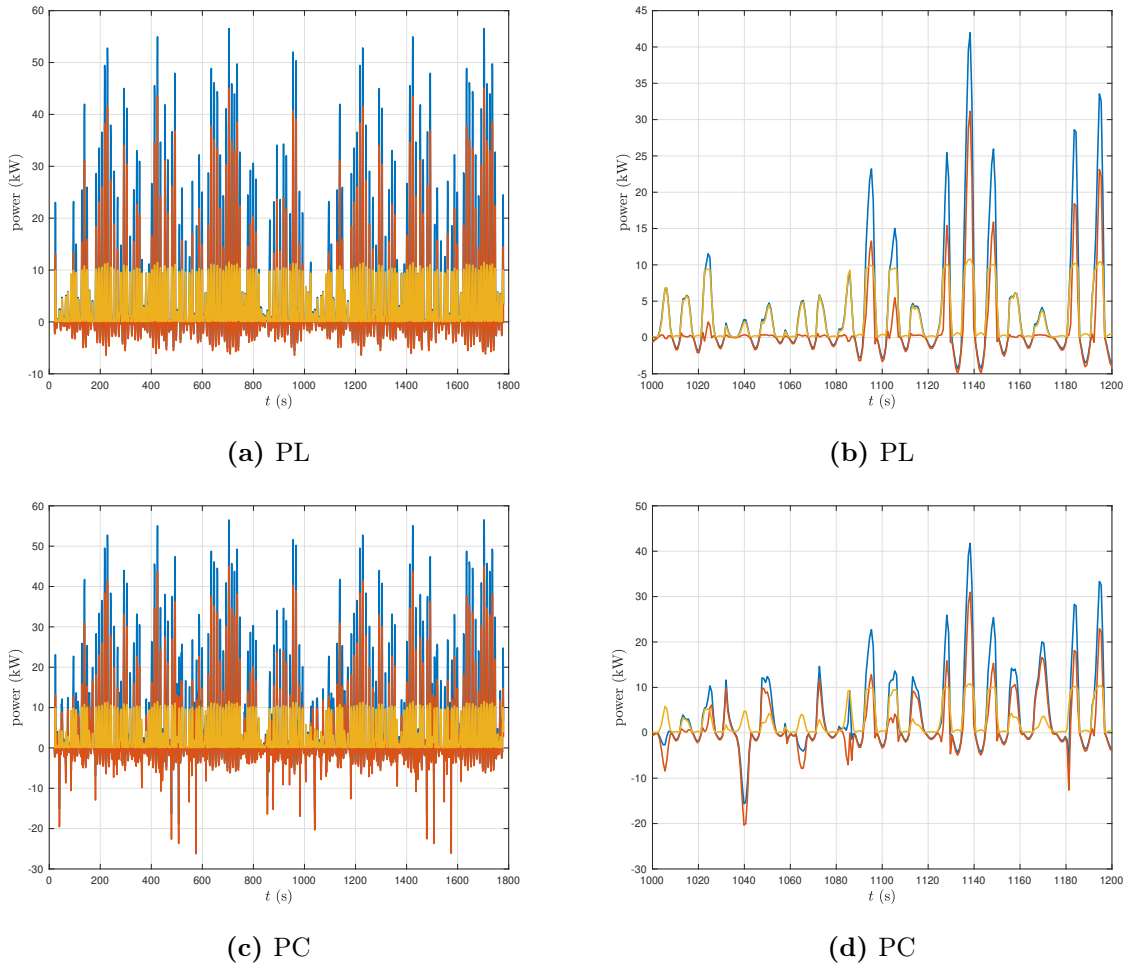
Figure 6.30: Instantaneous mechanical power P_{mech} (blue), electrical power P_e (red) and power losses P_l (yellow) over the entire simulation time (subfigures a and c) and for the time interval 1000 s to 1200 s (subfigures b and d) for both control methods.

S2

(a) PL
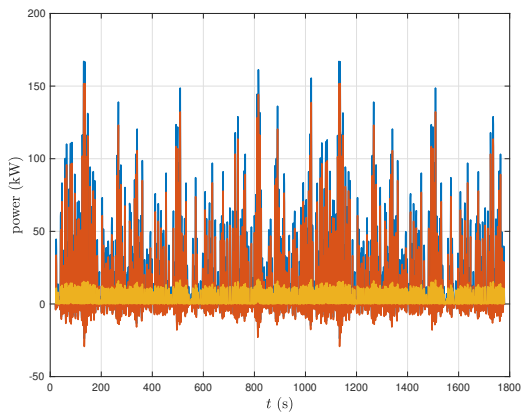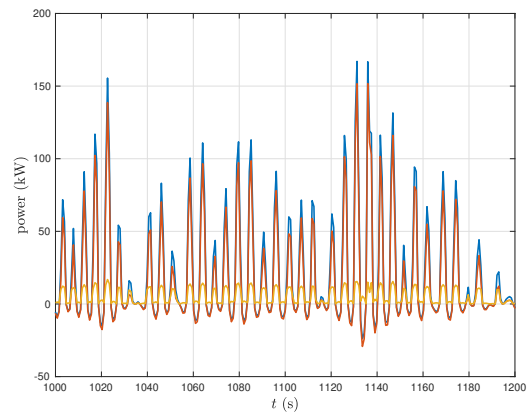
(b) PL
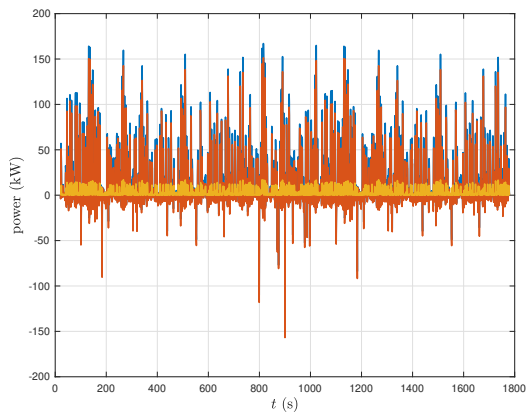
(c) PC
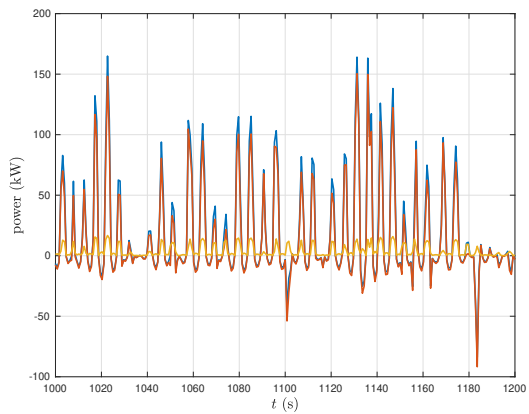
(d) PC

Figure 6.31: Instantaneous mechanical power P_{mech} (blue), electrical power P_e (red) and power losses P_l (yellow) over the entire simulation time (subfigures a and c) and for the time interval 1000 s to 1200 s (subfigures b and d) for both control methods.

S3

(a) PL

(b) PL

(c) PC

(d) PC
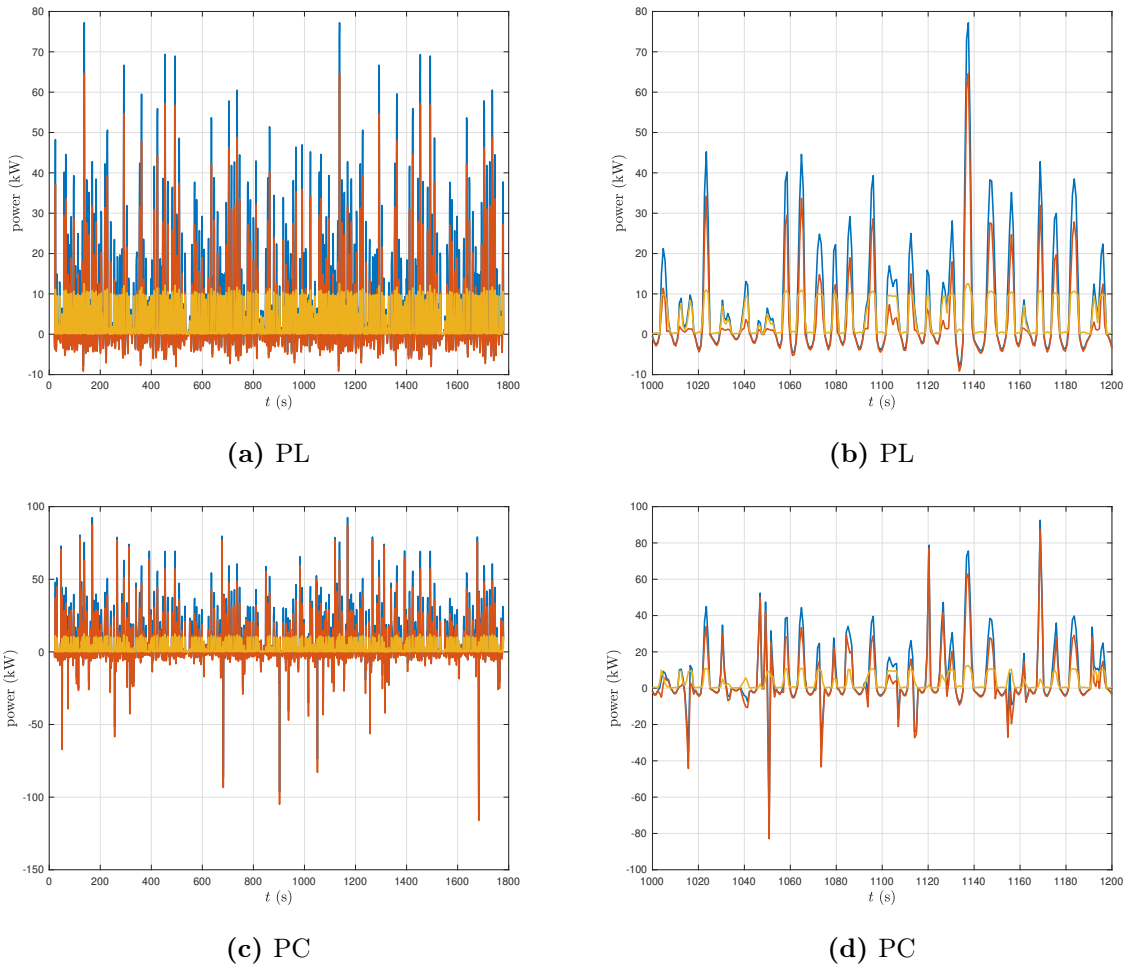
Figure 6.32: Instantaneous mechanical power P_{mech} (blue), electrical power P_e (red) and power losses P_l (yellow) over the entire simulation time (subfigures a and c) and for the time interval 1000 s to 1200 s (subfigures b and d) for both control methods.

6.2.8 PTO damping

The constant PTO damping found for PL is shown in Table 6.3, which is related to the chosen tuning frequency ($\omega_{1,fe}$) and the body parameters, as indicated by equation (4.1).

Table 6.3: PTO damping B_p for PL in the hydrodynamic model and the wave-to-wire model

	S1	S2	S3
B_p	$1.1506{\cdot}10^6$ kg/s	$6.302{\cdot}10^5$ kg/s	$9.3544{\cdot}10^5$ kg/s

Comparing the PTO damping for PC in Figures 6.33-6.35, it can be seen that the PTO damping oscillates more for S2 and less for S1, i.e., the oscillations in the PTO damping varies with the bandwidth of the sea state. This makes sense when the waves characterizing the sea state is considered. In S2, the waves are spread over a wider band of frequencies, being composed of high frequency waves generated by the local wind and swell conditions (low-frequency waves), resulting in more variations from wave-to-wave. For S1, the waves are characterized only by swells, which are more repetitive and similar

from wave-to-wave. As a result, the PTO damping will oscillate more over time for S2 than for S1. Since the PTO damping is dependent on the tuning frequency, the oscillations seen in the PTO damping will also be present in the chosen tuning frequency for PC.

S1

(a)   (b)
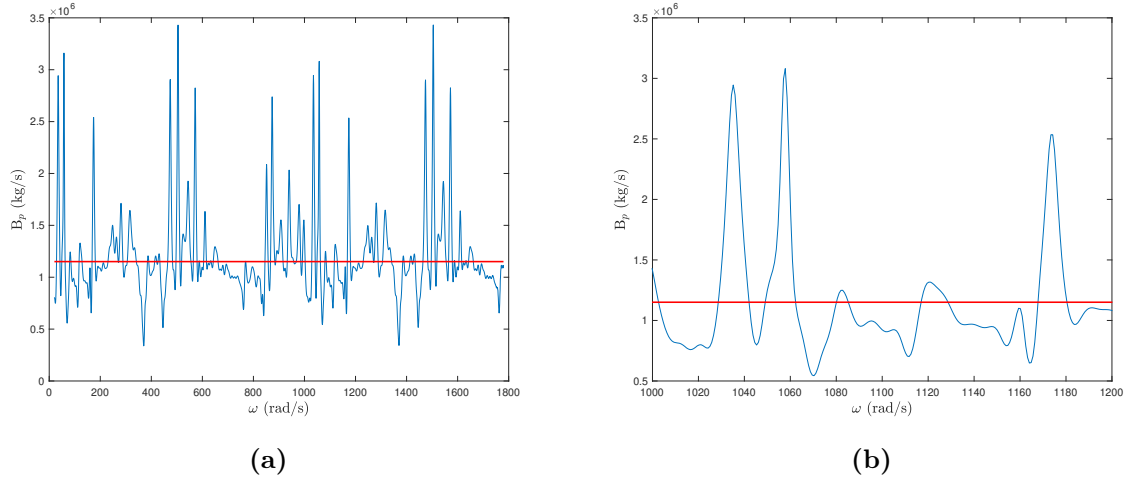
Figure 6.33: PTO damping B_p over the entire simulation time (subfigure a) and for the time interval 1000 s to 1200 s (subfigure b) for PC. The red line represent the constant PTO damping for PL.

S2

(a)   (b)
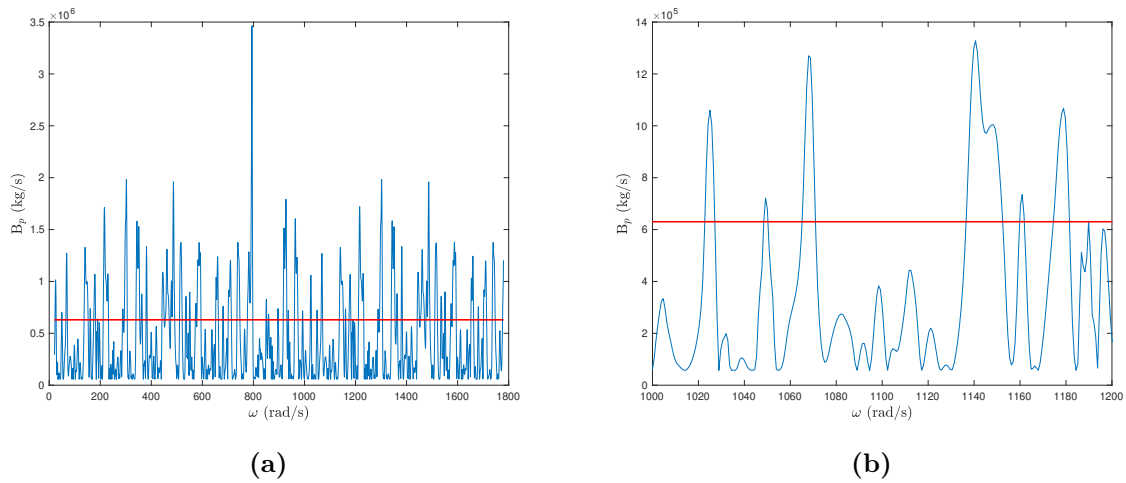
Figure 6.34: PTO damping B_p over the entire simulation time (subfigure a) and for the time interval 1000 s to 1200 s (subfigure b) for PC. The red line represent the constant PTO damping for PL.
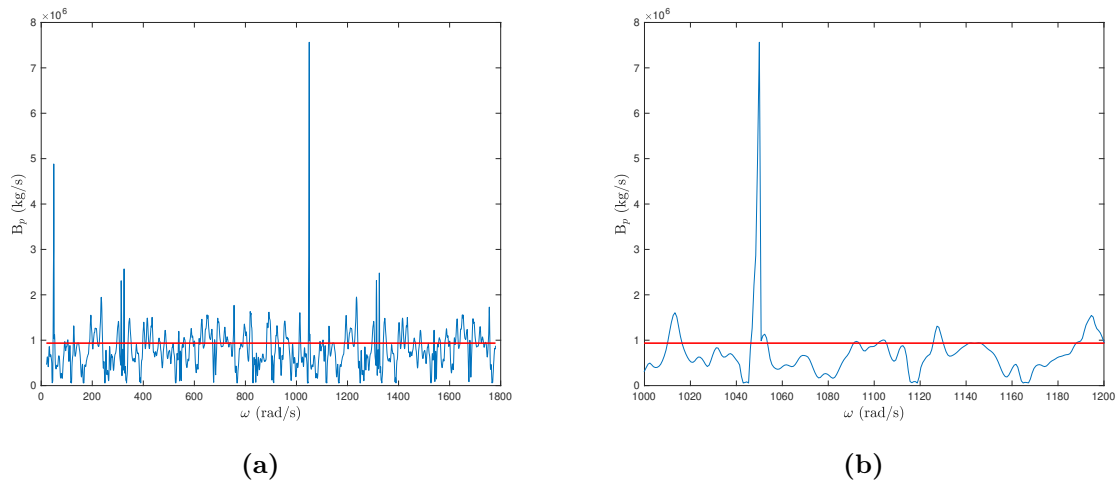
**Figure 6.35:** PTO damping B_p over the entire simulation time (subfigure a) and for the time interval 1000 s to 1200 s (subfigure b) for PC. The red line represent the constant PTO damping for PL.

6.2.9 Tuning frequencies

Figure 6.36 shows the ratio between the energy of the IMF components E_{c_i}, calculated by using equation (4.7), and the energy in the excitation force E_{fe}. It can be seen that the dominant IMF component is the first IMF component for all sea states, although for S2 the second IMF component is also significant. These results correspond to the results obtained in [11].
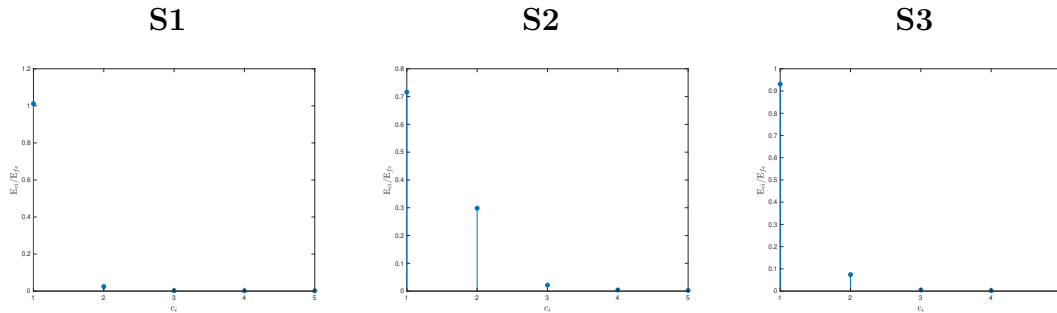
Figure 6.36: Ratios between the energy in the IMF components E_{c_i} and excitation force spectrum E_{fe}

In Table 6.4, the tuning frequency used for PL is presented. There it can be noticed that the tuning frequency varies with the bandwidth of the sea state, where the widest bandwidth results in a higher tuning frequency. The mean centroid frequency can mathematically be defined as the center of mass of the spectrum. By considering this, the mean centroid frequency will naturally be larger for a wideband spectrum since the energy is spread over a greater frequency band, shifting the center of mass. This behavior can also be seen in the calculated PTO damping for PL, shown in Table 6.3, where the PTO damping is largest for the lowest bandwidth. This can be seen through the chosen tuning frequency and the hydrodynamic coefficients in Figure 5.4, where a lower frequency gives

a larger added mass while the radiation damping looks like a normal distribution with its peak value around 1 rad/s.

Table 6.4: Tuning frequency used during PL in the hydrodynamic model and the wave-to-wire model

	S1	**S2**	**S3**
$\omega_{1,fe}$	0.5360 rad/s	0.7454 rad/s	0.6086 rad/s

Figures 6.37-6.39 shows the Hilbert spectrum of the first IMF component, i.e., the dominant IMF component, when PC is used as the control method. The Hilbert spectrum is an energy distribution over time and frequency. In Figures 6.37-6.39, the plot shows how the tuning frequency for PC varies over time, while the color scale, from yellow to dark blue, illustrates the energy content from correspondingly high to low. From the Hilbert spectrum of the first IMF component, it can be noted that the frequency ranges 0.5-0.55 rad/s, 0.4-0.8 rad/s, and 0.5-0.7 rad/s have the highest energy content for respectively S1, S2 and S3. As in [12], these values also coincide with the calculated mean centroid frequencies of the excitation force spectrum. However, HHT also identifies at which time these oscillations occur.

Taking a closer look at the tuning frequency for PC in Figures 6.37-6.39 it can be noticed that the tuning frequency oscillates in a repetitive manner. For instance, in Figure 6.37 the blue peak at 400 s is the same peak at 1400 s. The reason for these repetitions are related to the way the waves are generated in the simulations. In the simulations, the sea is modelled as a summation of different cosine-waves with different phases. At one point, the simulated sea will have repeated itself, also making the tuning frequency to repeat itself.

By following the tuning frequencies in Figures 6.37-6.39, it can also be seen that the tuning frequency has an underlying sinusoidal oscillation. This underlying oscillation can be more easily seen in the tuning frequency for S1 and S3. Comparing the oscillation for S1 in Figure 6.37 and the oscillation for S3 in Figure 6.39, it can be seen that the frequency oscillates in a slower frequency for S1 than the frequency for S3.

S1

(a)   (b)
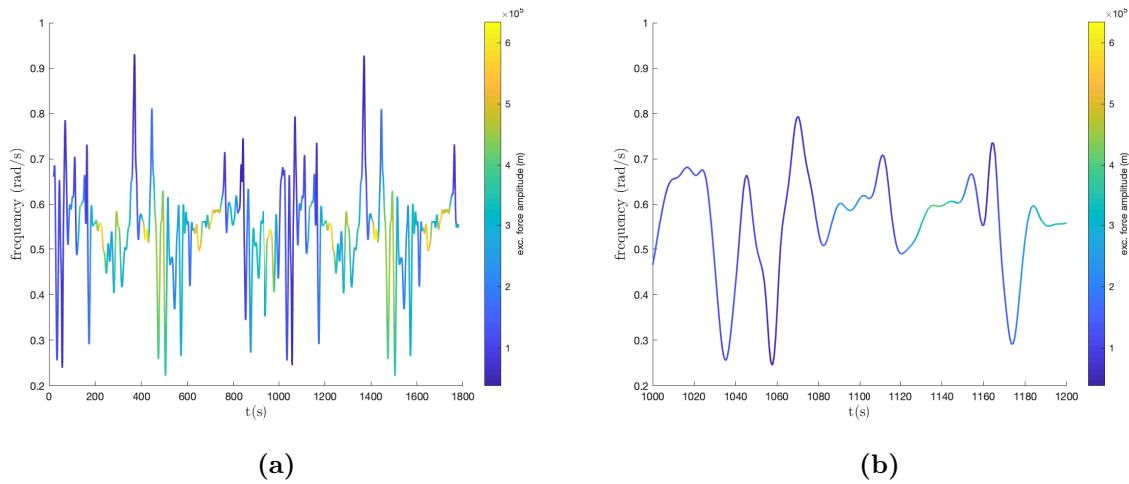
Figure 6.37: Hilbert spectrum of the first IMF over the entire simulation time (subfigure a) and for the time interval 1000 s to 1200 s (subfigure b) for PC.

S2

(a)   (b)
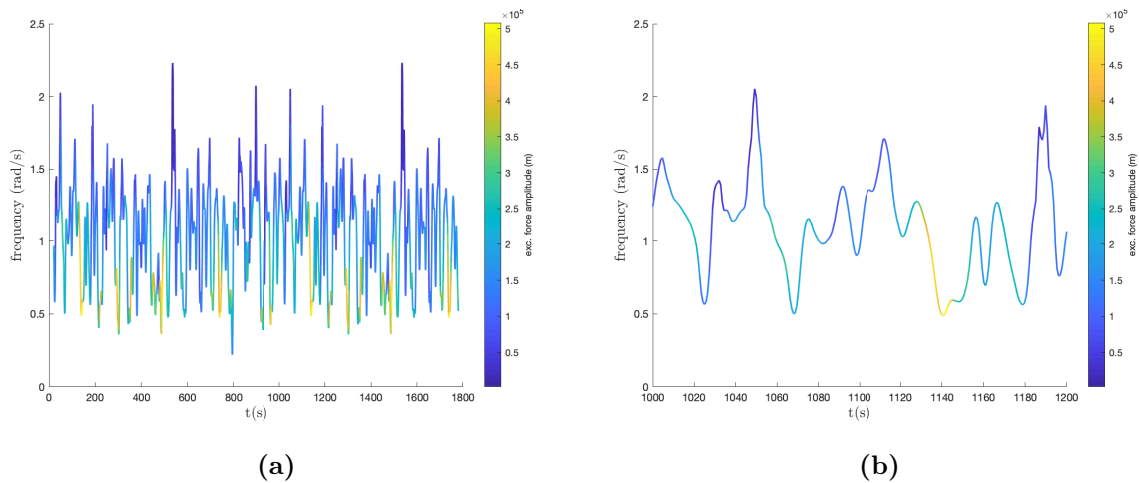
Figure 6.38: Hilbert spectrum of the first IMF over the entire simulation time (subfigure a) and for the time interval 1000 s to 1200 s (subfigure b) for PC.

There are more wild peaks in the tuning frequency for S3, in Figure 6.39, than for the other two sea states. Although, in the tuning frequency for S2 in Figure 6.38, the amplitude is much higher than for the other two sea states, making the wild peaks less apparent. The frequencies with a large amplitude are related to fast oscillations in the excitation force. The reason these oscillations become so evident in the tuning frequency could be a result of mode mixing in the EMD method. Comparing the wild peaks in the tuning frequency to the fast oscillations in the q-axis voltages in Figures 6.18, 6.20, and 6.22 it can be noticed that the wild peaks correspond to the fast oscillations seen in the q-axis voltages for PC.

S3

(a)

(b)
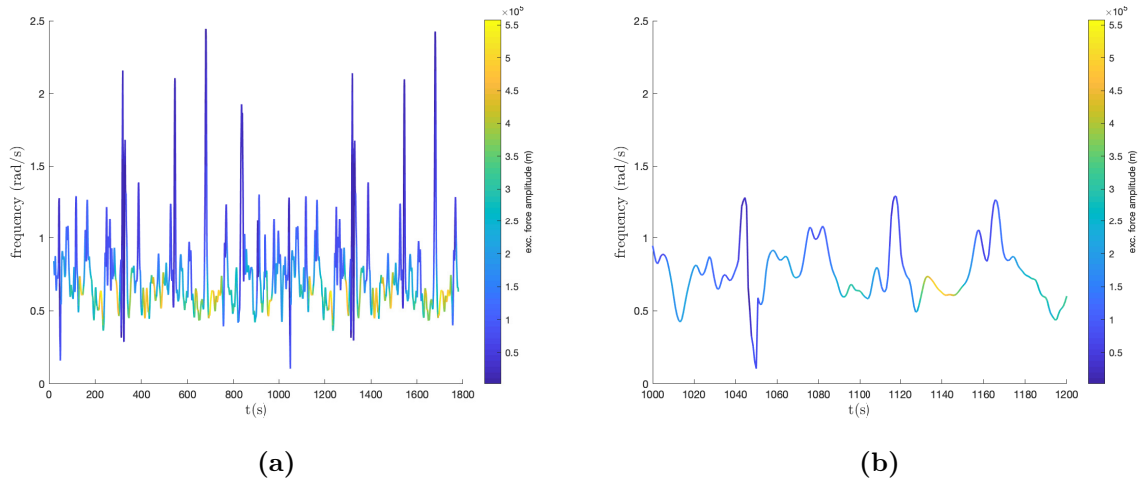
Figure 6.39: Hilbert spectrum of the first IMF over the entire simulation time (subfigure a) and for the time interval 1000 s to 1200 s (subfigure b) for PC.

6.2.10   Current controller

As previously mentioned, the PI-controller uses the stationary deviation between the reference currents and the output currents to calculate the reference voltages. In Figures 6.40-6.43, the stationary deviation, i.e., the input to the PI-controller, is presented for both PL and PC in all sea states. The d-axis currents are neglected for S1 and S3 as they are equal to zero during the entire simulation. From the figures it can be noticed that for PL, the deviation between the reference currents and the output currents are less than the deviation for PC. Comparing the deviation between i_q and $i_{q,ref}$ and the tuning frequencies for PC, it can be noticed that the spikes in the deviation are related to the wild peaks in the tuning frequency. This means that the current control system might be more suitable for a control method with a constant tuning frequency than with a varying tuning frequency.

From the PC results in Figures 6.40, 6.42, and 6.43, it can be concluded that i_q does not follow $i_{q,ref}$ properly. This result also reduces the oscillations in u_q for PC. In order to make the deviation between i_q and i$_{q,ref}$ smaller, the gain K_p in the PI-controller can be increased, but by increasing K_p the oscillations in u_q also increases, which is not desired because this results in more negative power. As a result, K_p needs to be held small. By not assuming an ideal converter bridge with PWM, K_p could be held higher and the stationary deviation between the reference and output currents for both control methods could be held low.

From equation (3.20), it is indicated that the reference q-axis current is proportional to the reference torque. As has been previously discussed, the reference torque has greater amplitudes for PC than for PL. Thus, the q-current references becomes much higher for PC than for PL. This may also be one of the reasons why PC demands larger K_p values in the PI-controller in order for i_q to better follow $i_{q,ref}$.

S1

(a) PL
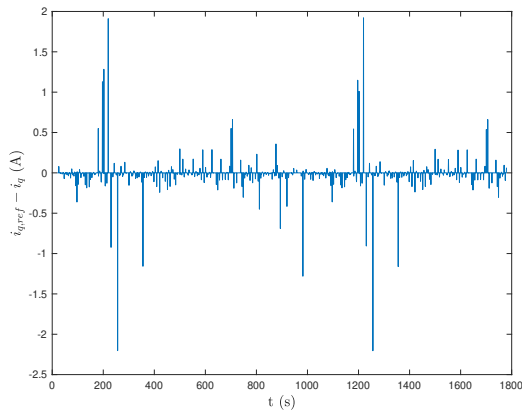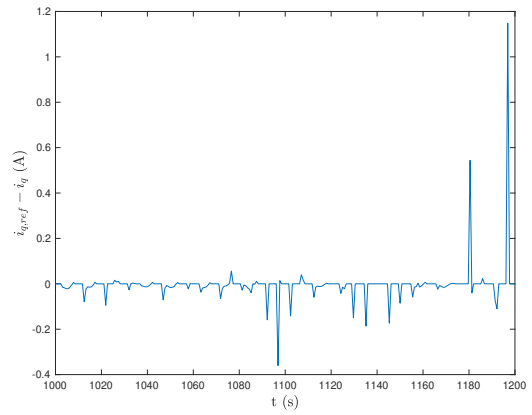
(b) PL
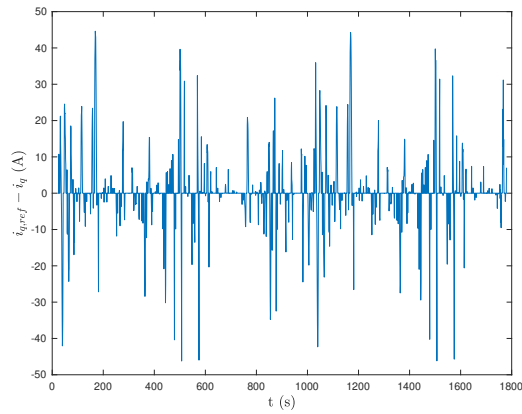
(c) PC
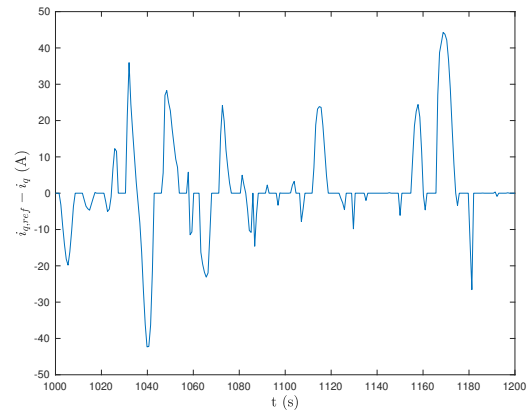
(d) PC

Figure 6.40: Stationary deviation between $i_{q,ref}$ and i_q over the entire simulation time (subfigure a and c) and for the time interval 1000 s to 1200 s (subfigure b and d) for both control methods.

S2

(a) PL
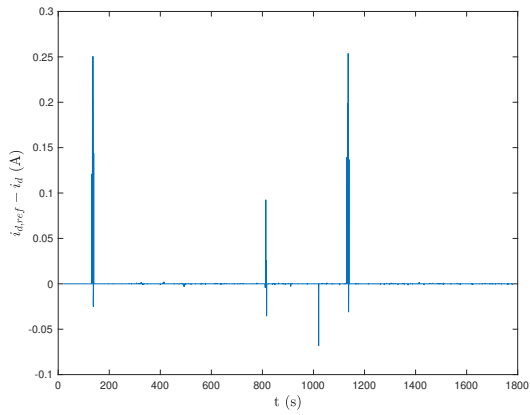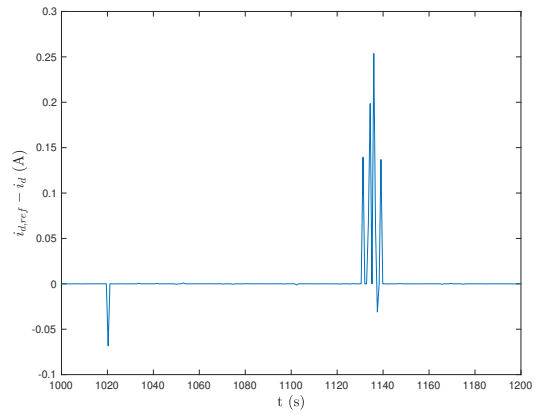
(b) PL
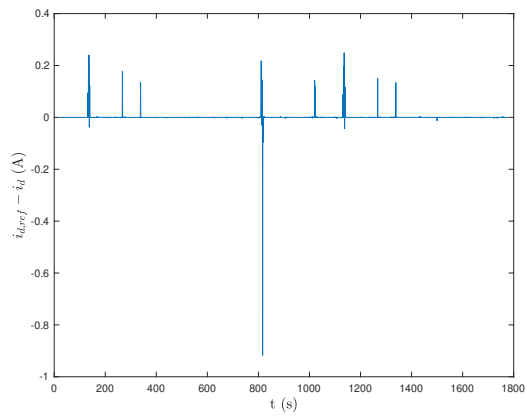
(c) PC
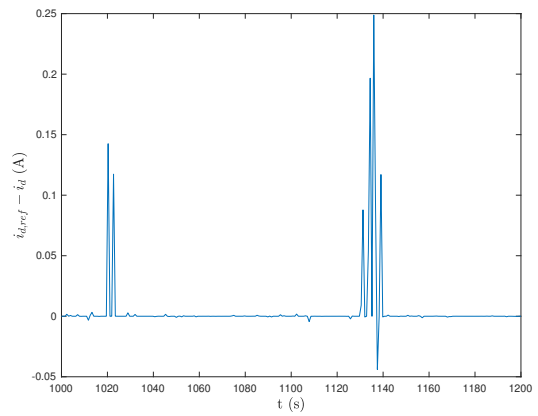
(d) PC

Figure 6.41: Stationary deviation between $i_{d,ref}$ and i_d over the entire simulation time (subfigure a and c) and for the time interval 1000 s to 1200 s (subfigure b and d) for both control methods.

S2

(a) PL
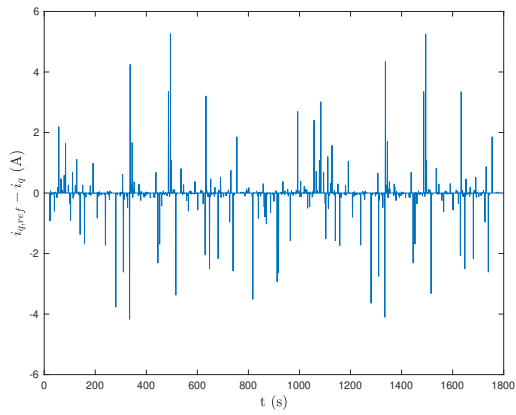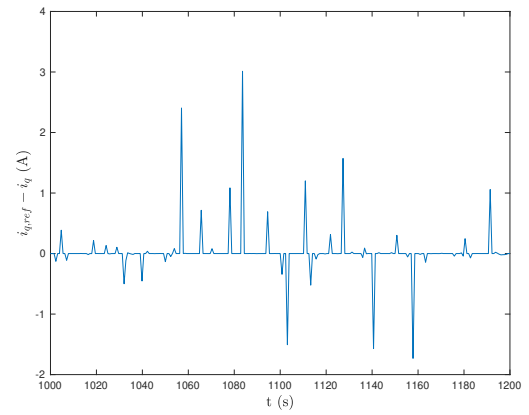
(b) PL
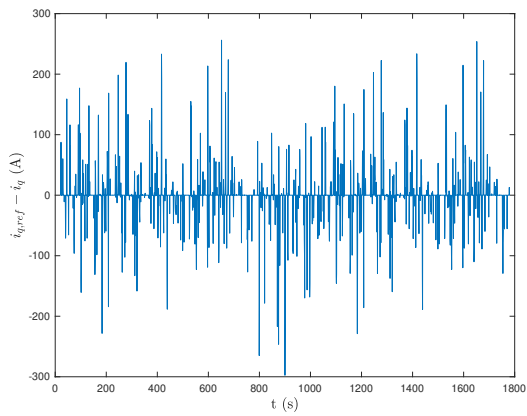
(c) PC
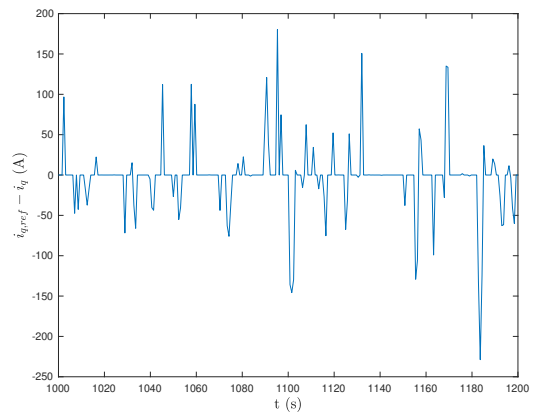
(d) PC

Figure 6.42: Stationary deviation between $i_{q,ref}$ and i_q over the entire simulation time (subfigure a and c) and for the time interval 1000 s to 1200 s (subfigure b and d) for both control methods.

S3

(a) PL

(b) PL

(c) PC

(d) PC
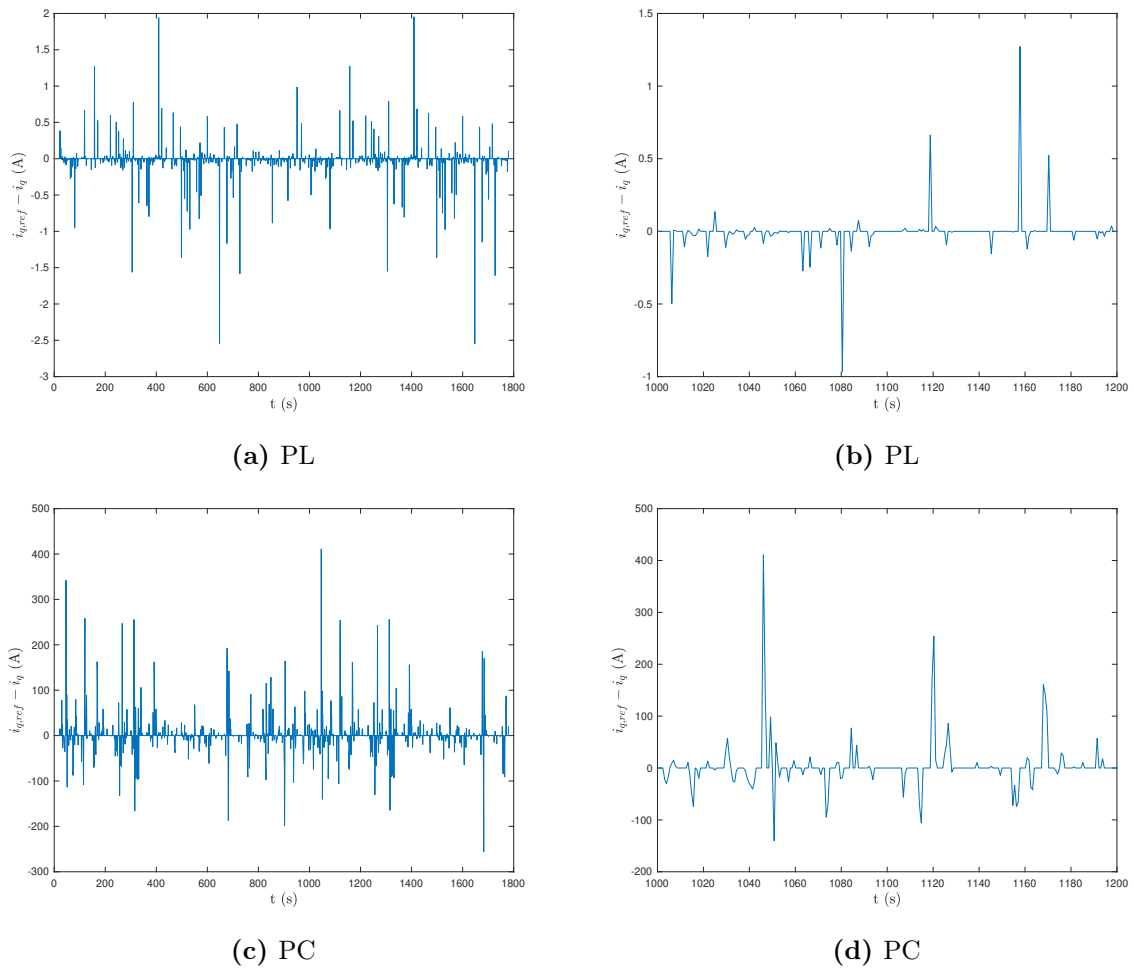
Figure 6.43: Stationary deviation between $i_{q,ref}$ and i_q over the entire simulation time (subfigure a and c) and for the time interval 1000 s to 1200 s (subfigure b and d) for both control methods.

Chapter 7

Ideal PTO model vs. non-ideal PTO model

7.1 PTO force

The calculated PTO force in the wave-to-wire model, i.e., for the non-ideal PTO system, is not the real force applied by the PTO. This can be seen through the comparison of the machinery force f_p when PC is applied in both the hydrodynamic model, i.e., for the ideal PTO system, and the wave-to-wire model for S2, as shown in Figure 7.1. It can be seen that f_p has a maximum and minimum value when the wave-to-wire model is used, but when the simulations are done with only the hydrodynamic model, the machinery force does not have any limitations. In other words, the machinery force is constrained by the PTO limitations. For the hydrodynamic model in Figure 7.1a, it can be noticed that the velocity of the WEC follow the machinery force, i.e., the velocity depends on the machinery force. Using this, the velocity of the WEC in Figure 7.1b also becomes bound by the PTO limitations. From equation (2.9), it is known that the machinery force depends on the WEC velocity and the PTO damping, or in other words, the PTO damping depends on the WEC velocity and machinery force. Because both the machinery force and WEC velocity is limited by the PTO, the PTO damping will also be restricted by the PTO specifications, ultimately justifying that the PTO damping used in the simulations are not the exact PTO damping calculated by the HHT method.

S2

(a)   (b)
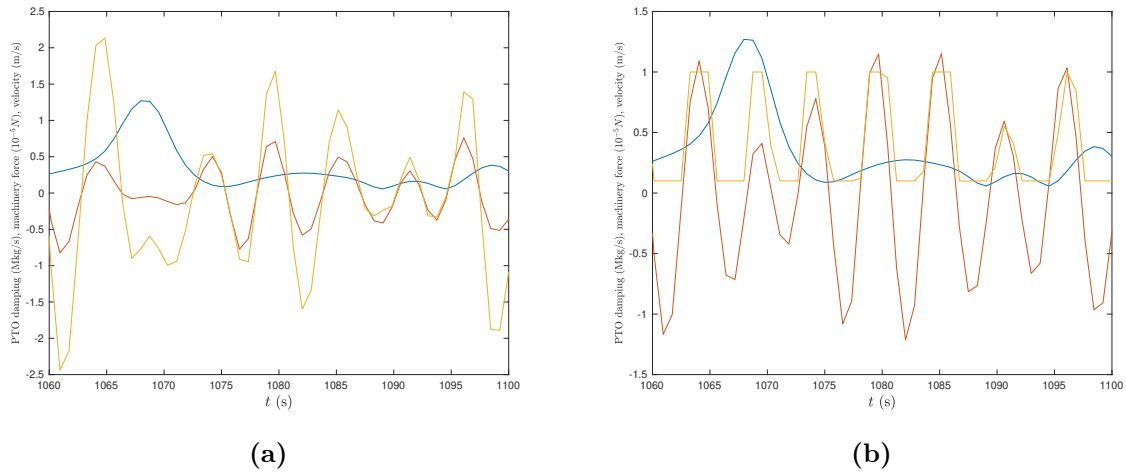
Figure 7.1: Machinery force (yellow), WEC velocity (orange) and PTO damping (blue) over the time interval 1060 s to 1100 s when PC is applied in the hydrodynamic model (subfigure a) and the wave-to-wire model (subfigure b).

Maximum torque values correspond to maximum PTO force values, as seen in equation (3.21). From the efficiency map in Figure 3.7, it is seen that for the velocity values obtained here, the efficiency of the generator and converter bridge is lower. By working with lower torque values, and hence lower machinery force, the efficiency of the PTO will increase, which might give more electrical power output.

7.2 Output power

From Table 6.1, it was concluded that PC for an ideal PTO has a greater advantage for sea states with a wider band of frequencies, like S2, than PL since the waves vary more. Looking at Table 6.2, the improvements PC gave for a wideband spectra can no longer be observed for the non-linear PTO. The reason for these different results will be discussed further.

When comparing the total output power from the wave-to-wire model in Figure 6.4 with the output power for the hydrodynamic model with an ideal PTO in Figure 6.2, it can be seen that the total output power for the wave-to-wire model is much lower than the output power from the hydrodynamic model only, for both PL and PC. The different output power results can be related to limitations in the generator efficiency only. The power output is on average 75% lower for PC and 70% lower for PL, when non-ideal and ideal PTO are compared. However, by looking at the absorbed power for the wave-to-wire model, before the electrical power loss, in Figure 6.3, it can be noticed that the absorbed power for the wave-to-wire model is already lower than the absorbed power for the hydrodynamic model in Figure 6.2. In this case, the power absorbed is on average 60% lower for PC and 50% lower for PL, when non-ideal and ideal PTO are compared. This means that the PTO specifications and limitations also have an impact on the amount of power that the WEC can absorb, and hence generate. One of these limitations are related to the maximum and minimum PTO force, which in the end, limits the generator torque, currents, and voltages.

Further, looking at the positive electrical power for the wave-to-wire model, in Figure 6.4, it can be seen that PC result in more absorbed power than PL for all sea states. On average, PC absorbs approximately 10% more power than PL. This corresponds to the absorbed power results for the hydrodynamic model in Figure 6.2. These results are connected to the fact that PC adapts to each wave, exploiting the oscillating frequency of the most energetic incoming wave, while PL chooses a constant tuning frequency after the excitation force spectrum.

For the wave-to-wire model, Table 6.2 shows that both S1 and S3 give the highest difference between PL and PC in the absorbed power, while for S2 the two control methods absorb around the same amount of power. On the other hand, the result from the hydrodynamic model shows that PC has a greater advantage for wideband sea states, like S2, and for sea states with a narrower banded sea spectra, like S1, the difference between PL and PC is very small. The different output results from the two models are related to the PTO damping and the control system of the WEC. For a wideband sea state, it has been shown that the PTO damping varies more. This brings more challenges to the PTO control system, which causes more losses and thus limiting the advantage of the PC control method.

As previously discussed, the rapid changes in the PTO damping for S2 gives more demands to the control system of the WEC. In this thesis, the converter bridge with PWM has been assumed to be ideal, which has given a larger dependence on the tuning of the PI-controller in the current controller. The converter bridge with PWM should be implemented in order to better evaluate the effect PC has on a fully-coupled wave-to-wire model.

One important comment when the results from these two models are compared is that the hydrodynamic model is not optimized to the electric PTO model, and vice versa. Thus, the results might be different, for a different body geometry. Furthermore, the modelled WEC is based on only one degree of freedom. By expanding this simplified model to include more degrees of freedom might give a better view of the advantages and disadvantages of the PC control scheme for a full wave-to-wire model. It can also be discussed whether or not how the system works makes it more challenging to implement more advanced control methods. Sjolte, Tjensvoll, and Molinas [47] showed that this WEC, with this working principle, has limited potential for increased power extraction using reactive control. In this thesis, it has been shown that the same model has encountered some challenges for a more advanced form of passive loading, where, for instance, PC on average requires 84% more power from the grid compared to PL.

Chapter 8

Conclusion

The aim of this thesis was to investigate the impact a passive control scheme with HHT has on the electric output of a WEC with a non-ideal PTO system. In order to do this, the hydrodynamic model of the oscillating cylinder in [11] was connected to an all-electric PTO system, like the system of the wave energy converter Lifesaver [10]. To be able to see the effect of the passive control scheme, the results were compared to the results when running a hydrodynamic model with an ideal PTO and when using passive loading tuned to the mean centroid frequency of the excitation force spectrum.

When an ideal PTO is assumed, the advantage of PC over PL is seen for a wideband spectra. However, when a non-ideal electric PTO is included, the improvements PC gave over PL for a wideband spectra could no longer be observed. By comparing the output results, it was seen how the PTO limitations to the machinery force restrict the WEC's movement in the waves. As a result, the amount of power the WEC can absorb, and thus generate, is being bounded by the PTO specifications and the generator efficiency, restricting the WEC from operating at its full potential. The PTO limitations also result in that the electric PTO system works at the boundary of its capacity over longer period of times, which could result in other losses related to wear and tear over time.

As a result of the working principle of the modelled WEC, the electrical power results were divided into its negative and positive components. From these results, it was observed that PC generates more electrical power than PL, similar to the results from the hydrodynamic model. However, PC also require more power from the grid in order to operate correctly. On the other hand, higher power losses are obtained with PL than with PC. The higher power losses are derived from higher generator torques, and hence, higher stator currents for PL. In the wave-to-wire model, the power losses were only found on the basis of the stator copper losses, even though iron losses also are a significant fraction of the total losses in a SMPMSM. An inclusion of the iron losses could give different results and a more clear picture on the total power losses related to each control method. Nevertheless, due to the high power requirement from the grid during the downwards motion of the WEC for PC, PL was found to give on average more electrical power output than PC.

One of the challenges throughout the simulations with PC for the wave-to-wire model was the PTO control system, where the current controller was simplified. In the current controller model, the converter bridge with PWM was assumed to be ideal and that the output voltages follow the reference voltages perfectly. This assumption may have made

it more difficult for the current controller to handle the fast oscillations in the voltages, caused by the varying tuning frequency of the PC control strategy, resulting in more negative power being drawn from the grid. Since PL holds the tuning frequency constant, these oscillations were not observed in the results. It can then be seen that the benefit of using a time-varying PTO damping is reduced when the control system is having difficulties handling the fast oscillations in the tuning frequency. As a conclusion, in order to apply the PC control method, a more dynamic control system is required, while for PL the simplified control system works fine.

8.1 Further work

In this thesis, the simplified current controller has been thoroughly discussed. The basis of the future work connected to the PC control method and the effect it has on the electrical power output should be related to the implementation of the converter bridge converter with PWM to see if the challenges with PC and the non-ideal PTO becomes more moderate. These studies can also help understand the current controller and the effect fast variations in the damping has on the output when the converter bridge with PWM is implemented better.

By including the grid connected system into the model, the total delivered power can be studied and other challenges related to the working principle of the PTO can be located. The hydrodynamic model can also be further evolved by including more degrees of freedom, and the advantages and disadvantages of PL and PC could be studied further.

For the PC control method in general, Garcia-Rosa et al. [11] suggested a further study on a strategy where more than one IMF component is considered when finding the tuning frequency. From the results obtained here, this could be interesting to investigate further with a non-ideal PTO as well. A drawback is if this would lead to more oscillations in the tuning frequency. Another element that can be further investigated is the effect of mode mixing and how this influence the tuning frequency.

Bibliography

[1]   Ocean Energy Systems. *Annual report - An overview of ocean energy activities in 2018*. Tech. rep. The Executive Committee of Ocean Energy Systems, 2019.

[2]   T.W. Thorpe. "Wave Energy". In: *2010 survey of energy resources*. World Energy Council, 2010, pp. 562–573.

[3]   Wave Net. *Establishment of a European thematic network on wave energy*. Tech. rep. European Commission, 2003.

[4]   T.W. Thorpe. *A brief Review of Wave Energy*. Tech. rep. The UK Department of Trade and Industry, May 1999.

[5]   *World Energy Outlook 2019*. World Energy Outlook. International Energy Agency, 2019.

[6]   J. V. Ringwood, G. Bacelli, and F. Fusco. "Energy-Maximizing Control of Wave-Energy Converters: The Development of Control System Technology to Optimize Their Operation". In: *IEEE Control Systems Magazine* 34.5 (Oct. 2014), pp. 30–55.

[7]   Kjell Budal and Johannes Falnes. "A resonant point absorber of ocean-wave power". In: *Nature* 256 (Aug. 1975), pp. 478–479.

[8]   Antonio Falcao and João Henriques. "Effect of non-ideal power take-off efficiency on performance of single- and two-body reactively controlled wave energy converters". In: *Journal of Ocean Engineering and Marine Energy* 1 (Apr. 2015), pp. 273–286.

[9]   Romain Genest, Félicien Bonnefoy, Alain H. Clement, and Aurélien Babarit. "Effect of non-ideal power take-off on the energy absorption of a reactively controlled one degree of freedom wave energy converter". In: *Applied Ocean Research* 48 (Oct. 2014), pp. 236–243.

[10] Jonas Sjolte, Christian Sandvik, Elisabetta Tedeschi, and Marta Molinas. "Exploring the Potential for Increased Production from the Wave Energy Converter Lifesaver by Reactive Control". In: *Energies* 6 (July 2013), pp. 3706–3733.

[11] Paula B. Garcia-Rosa, Geir Kulia, John V. Ringwood, and Marta Molinas. "Real-Time Passive Control of Wave Energy Converters Using the Hilbert-Huang Transform". In: *IFAC-PapersOnLine Volume 50(1), Proc. of the 20th IFAC World Congress*. July 2017, pp. 14705–14710.

[12] P. B. Garcia-Rosa, J. V. Ringwood, O. B. Fosso, and M. Molinas. "The Impact of Time–Frequency Estimation Methods on the Performance of Wave Energy Converters Under Passive and Reactive Control". In: *IEEE Transactions on Sustainable Energy* 10.4 (Oct. 2019), pp. 1784–1792.

[13] Walter H. Michel. "Sea Spectra Revisited". In: *Marine Technology* 36.4 (1999), pp. 211–227.

[14] Michel K. Ochi and E. Nadine Hubble. "Six-Parameter Wave Spectra". In: *15th International Conference on Coastal Engineering*. 1976, pp. 301–328.

[15] Michel K. Ochi. "Wave statistics for the design of ships and ocean structures". In: Society of Naval Architects and Engineers, Nov. 1978.

[16] M. S. Longuet-Higgins. "Statistical Properties of Wave Groups in a Random Sea State". In: *Philosophical Transactions of the Royal Society of London. Series A, Mathematical and Physical Sciences* 312.1521 (Oct. 1984), pp. 219–250.

[17] Pierpaolo Ricci, Jean-Baptiste Saulnier, Antonio Falcao, and M. Pontes. "Time-Domain Models and Wave Energy Converters Performance Assessment". In: *Proceedings of the ASME 2008 27th International Conference on Offshore Mechanics and Arctic Engineering*. Vol. 6. June 2008.

[18] Johannes Falnes. *Ocean waves and oscillating systems: Linear Interaction Including Wave-Energy Extraction*. 2nd ed. Cambridge University Press, 2004.

[19] W. E. Cummins. "The impulse response function and ship motions". In: *Schiffstechnik* 47.9 (1962), pp. 101–109.

[20] M. Greenhow and S. P. White. "Optimal heave motion of some axisymmetric wave energy devices in sinusoidal waves". In: *Applied Ocean Research* 19.3-4 (Aug. 1997), pp. 141–159.

[21] Pierpaolo Ricci. "Time-Domain Models". In: *Numerical Modelling of Wave Energy Converters: State-of-the Art Techniques for Single WEC and Converter Arrays*. Ed. by Matt Folley. Elsevier Inc., 2016, pp. 31–66.

[22] Umesh A. Korde and John V. Ringwood. *Hydrodynamic Control of Wave Energy Devices*. 1st ed. United Kingdom: Cambridge University Press, 2016.

[23] Jonas Sjolte. "Marine renewable energy conversion: Grid and off-grid modeling, design and operation". PhD thesis. Norwegian University of Science and Technology, 2014.

[24] P. Pillay and R. Krishnan. "Application characteristics of permanent magnet synchronous and brushless DC motors for servo drives". In: *IEEE Transactions on Industry Applications* 27.5 (Oct. 1991), pp. 986–996.

[25] Sandra Eriksson. "Design of Permanent-Magnet Linear Generators with Constant-Torque-Angle Control for Wave Power". In: *Energies* 12 (Apr. 2019), p. 1312.

[26] Ned Mohan. *Advanced Electric Drives: Analysis, Control, and Modeling Using MATLAB/Simulink®*. 16th ed. New Jersey: John Wiley & Sons, 2014.

[27] Peter Vas. *Vector control of AC machines*. Vol. 22. Monographs in electrical and electronic engineering. Oxford: Clarendon Press, 1990.

[28] R. H. Park. "Two-reaction theory of synchronous machines generalized method of analysis-part I". In: *Transactions of the American Institute of Electrical Engineers* 48.3 (July 1929), pp. 716–727.

[29] Edward Wilson Kimbark. *Power System Stability: Synchronous Machines*. New York: IEEE Press Power Systems Engineering Series, 1995.

[30] Ned Mohan, Tore M Undeland, and William P. Robbins. *Power Electronics: Converters, Applications and Design*. 3rd ed. New Jersey: John Wiley & Sons, 2003.

[31] Roy Nilsen. *TET4120 - Electric Drives*. Norwegian University of Science and Technology, Department of Electric Power Engineering, 2018.

[32] Chandra Bajracharya, Marta Molinas, Jon Suul, and Tore Undeland. "Understanding of Tuning Techniques of Converter Controllers for VSC-HVDC". In: *Proceedings of the Nordic Workshop on Power and Industrial Electronics*. June 2008.

[33] Jeffrey Umland and M. Safiuddin. "Magnitude and symmetric optimum criterion for the design of linear control systems: What is it and how does it compare with the

others?" In: *IEEE Transactions on Industry Applications* 26.3 (June 1990), pp. 489–497.

[34] Jens G. Balchen, Trond Andresen, and Bjarne A. Foss. *Reguleringsteknikk*. 6th ed. Trondheim: Norges Teknisk-Naturvitenskapelige Universitet, Institutt for teknisk kybernetikk, 2016.

[35] J. Lemmens, P. Vanassche, and J. Driesen. "PMSM Drive Current and Voltage Limiting as a Constraint Optimal Control Problem". In: *IEEE Journal of Emerging and Selected Topics in Power Electronics* 3.2 (June 2015), pp. 326–338.

[36] Stephan Meier. "Theoretical design of surface-mounted permanent magnet motors with field weakening capability". MA thesis. Royal Institute of Technology, 2002.

[37] Ching-Tsai Pan and Jenn-Horng Liaw. "A Robust Field-Weakening Control Strategy for Surface-Mounted Permanent-Magnet Motor Drives". In: *IEEE Transactions on Energy Conversion* 20.4 (Dec. 2005), pp. 701–709.

[38] Christian Mclisky Sandvik. "Wave-to-Wire Model of the Wave Energy Converter Bolt2". MA thesis. Norwegian University of Science and Technology, 2012.

[39] Martine Furnes Pettersen. *Hydrodynamic model of the wave energy converter Bolt2*. Project report in TET4520. Department of Electric Power Engineering, NTNU – Norwegian University of Science and Technology, Dec. 2019.

[40] Jeffrey A. Oskamp and H. Tuba Özkan-Haller. "Power Calculations for a Passively Tuned Point Absorber Wave Energy Converter on the Oregon Coast". In: *Renewable Energy* 45 (Sept. 2012), pp. 72–77.

[41] Kjell Budal, Johannes Falnes, Lars Christian Iversen, Per Magne Lillebekken, Geirmund Oltedal, Tormod Hals, Tor Onshus, and Arne S. Høy. "The Norwegian wave-power buoy project". eng. In: *The Second International Symposium on Wave Energy Utilization*. Norges teknisk-naturvitenskapelige universitet, Fakultet for naturvitenskap og teknologi, Institutt for fysikk, June 1982.

[42] J.M.J. Journée and W.W. Massie. *Offshore Hydrodynamics*. 1st ed. Delft, Netherlands: Delft University of Technology, 2001.

[43] N. E. Huang, Z. Shen, S. R. Long, M. C. Wu, H. H. Shih, Q. Zheng, N.-C. Yen, C. C. Tung, and H. H. Liu. "The empirical mode decomposition and the Hilbert spectrum for nonlinear and non-stationary time series analysis". In: *Proc. Royal Society London* 454 (1998), pp. 903–995.

[44] A. Zeiler, R. Faltermeier, I. R. Keck, A. M. Tomé, C. G. Puntonet, and E. W. Lang. "Empirical Mode Decomposition - an introduction". In: *The 2010 International Joint Conference on Neural Networks (IJCNN)*. July 2010, pp. 1–8.

[45] Victor for MetaQuotes Software Corp. *Introduction to the Empirical Mode Decomposition Method*. Last accessed 12 May 2020. 2012. URL: https://www.mql5.com/en/articles/439.

[46] P. Welch. "The use of fast Fourier transform for the estimation of power spectra: A method based on time averaging over short, modified periodograms". In: *IEEE Transactions on Audio and Electroacoustics* 15.2 (June 1967), pp. 70–73.

[47] Jonas Sjolte, Gaute Tjensvoll, and Marta Molinas. "All-Electric Wave Energy Converter with Stand-alone 600VDC Power System and Ultracapacitor Bank". In: *Electric Vehicles and Renewable Energy conference*. Mar. 2012.

[48] Alexandra Barmpatza and Joya Kappatou. "Finite Element Method Investigation and Loss Estimation of a Permanent Magnet Synchronous Generator Feeding a Non-Linear Load". In: *Energies* 11 (Dec. 2018), p. 3404.

[49]   Fredrik Bülow, Sandra Eriksson, and Hans Bernhoff. "No-load core loss prediction of PM generator at low electrical frequency". In: *Renewable Energy* 43 (July 2012), pp. 389–392.

[50]   S. Morimoto, Y. Takeda, T. Hirasa, and K. Taniguchi. "Expansion of operating limits for permanent magnet motor by current vector control considering inverter capacity". In: *IEEE Transactions on Industry Applications* 26.5 (Oct. 1990), pp. 866–871.

Appendix A

Appendix

A.1 Entire Simulink model

Here, all the subsystems of the wave-to-wire Simulink model shown in Figure 5.6 are presented.
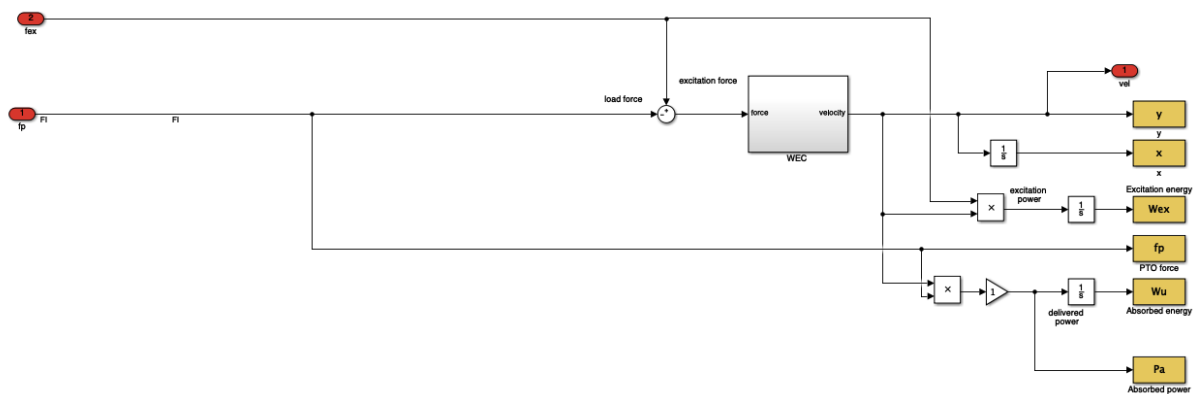
Figure A.1: Hydrodynamic subsystem
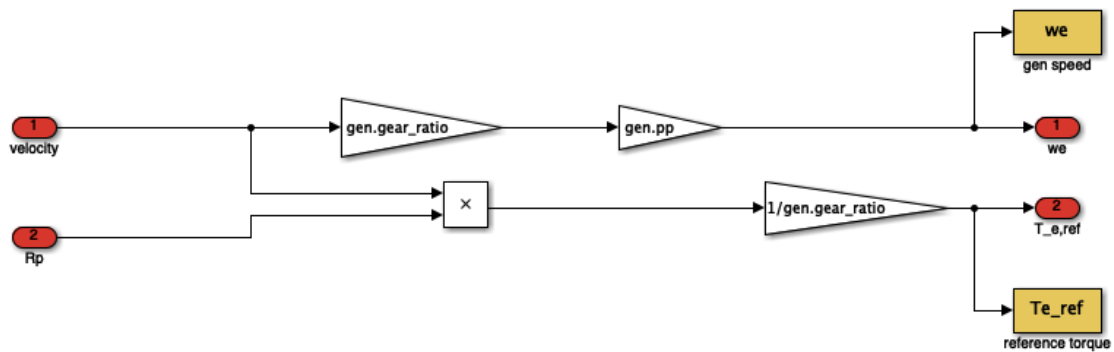
Figure A.2: Generate $T_{e,ref}$ subsystem
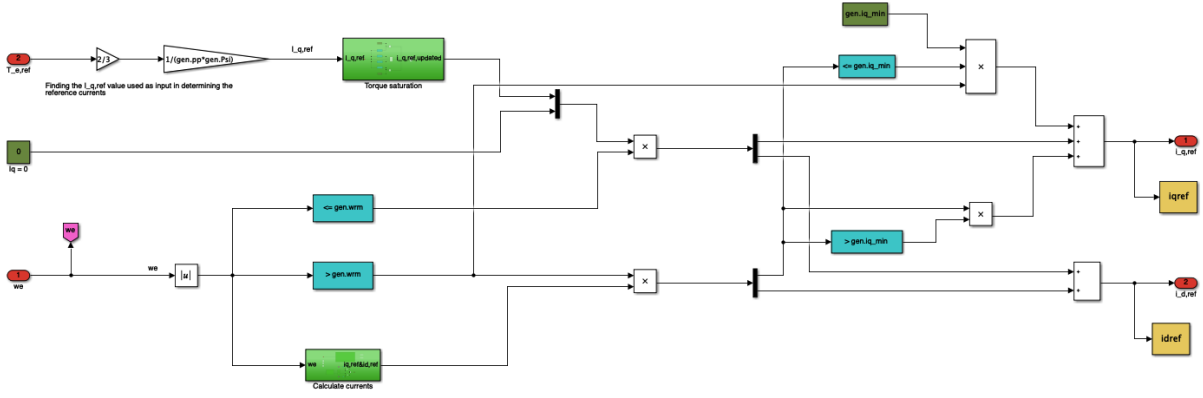
(a) Torque control subsystem
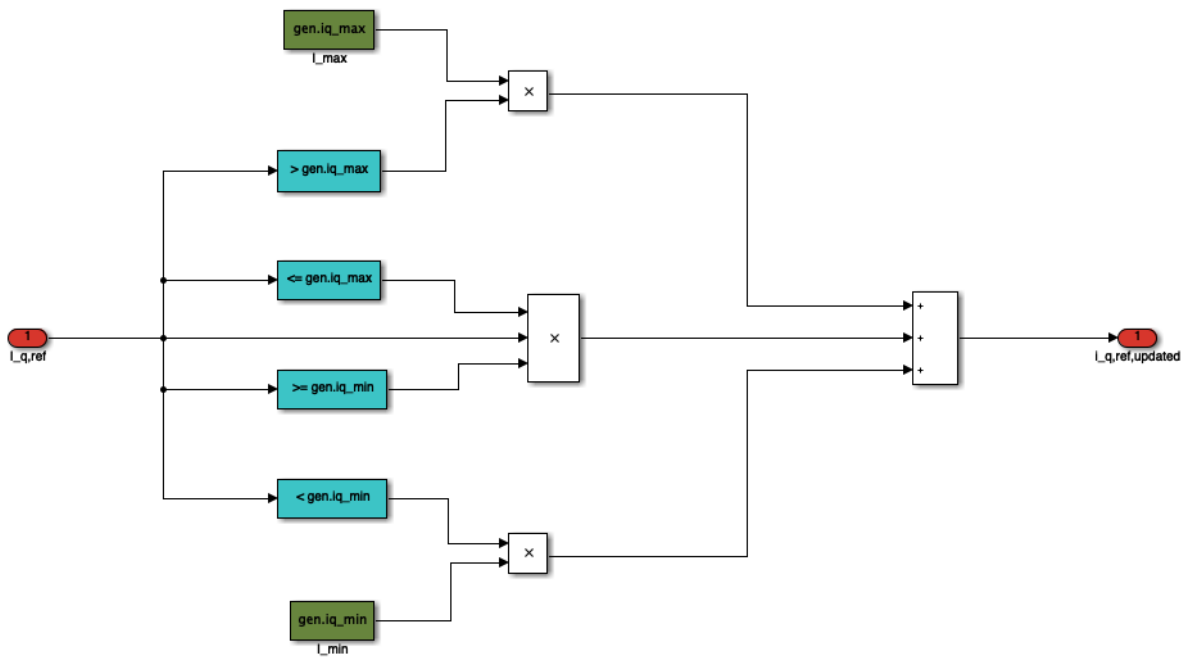
(b) Torque saturation subsystem
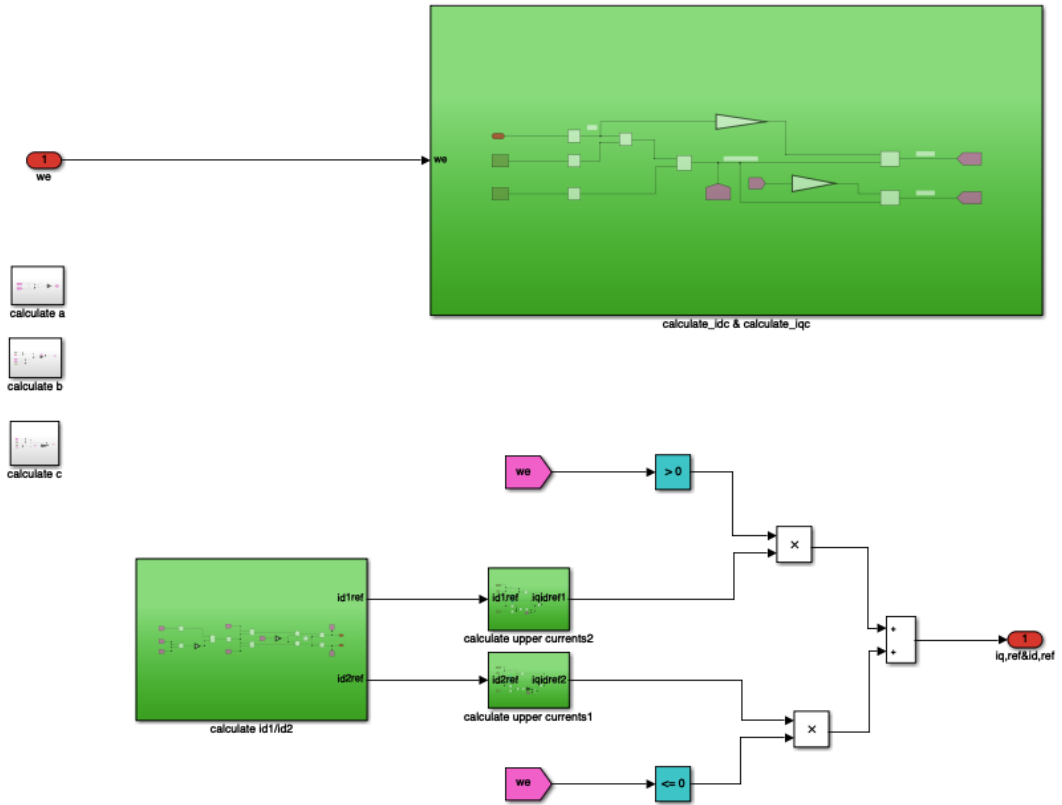
(c) Calculate currents subsystem
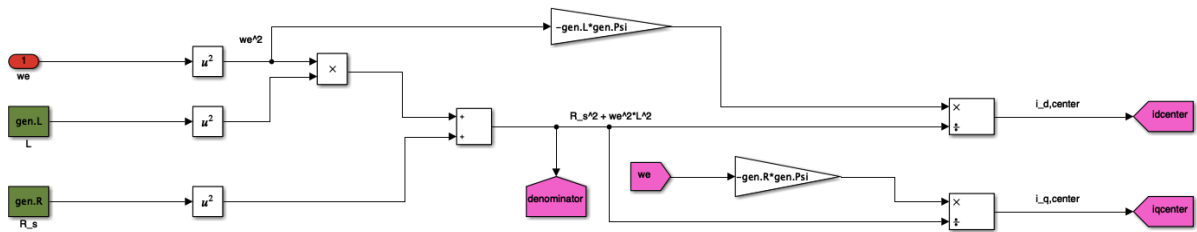
(d) Calculate idc & calculate iqc subsystem
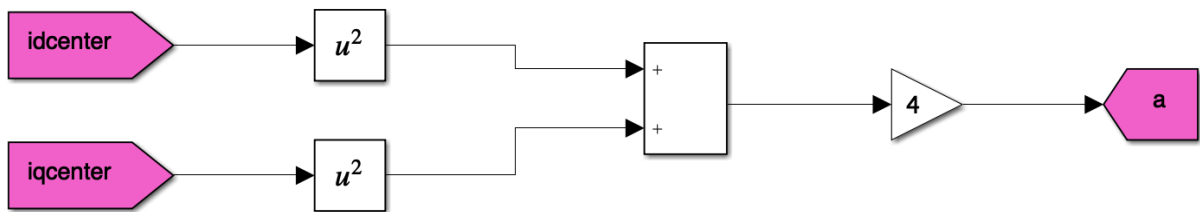
(e) a subsystem
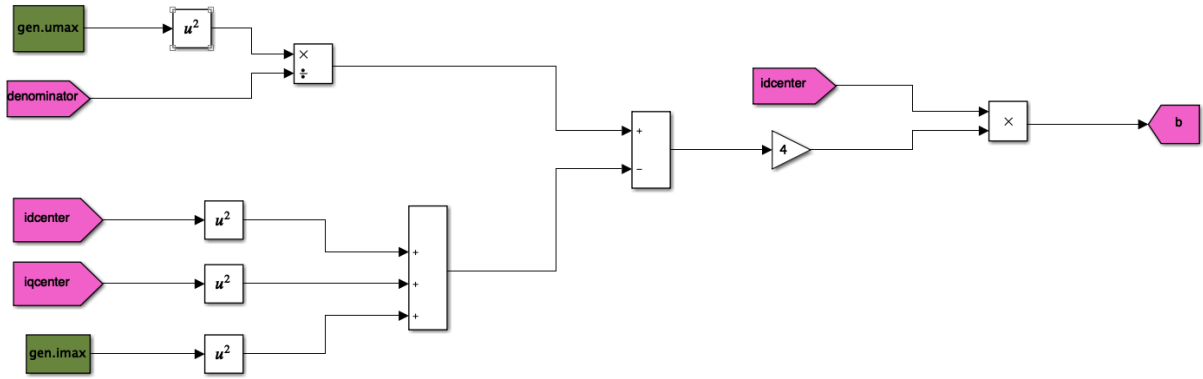
(f) b subsystem
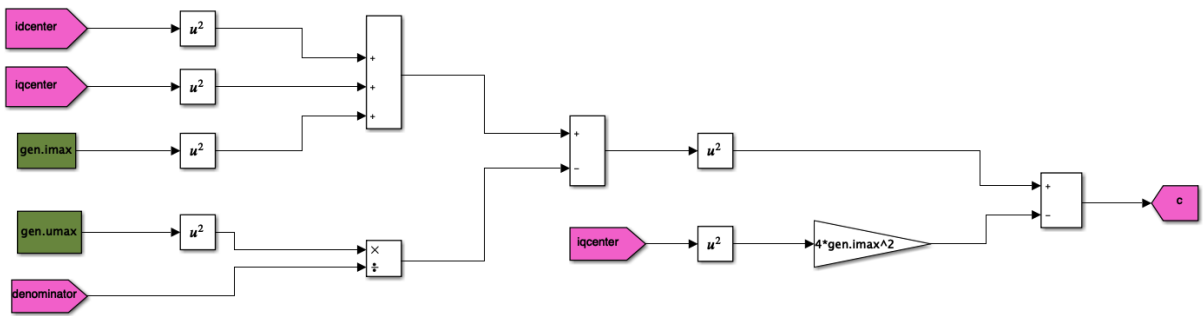
(g) c subsystem
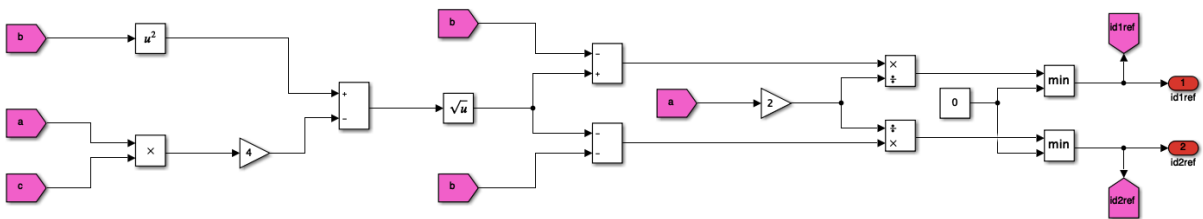
(h) Calculate id1/id2 subsystem
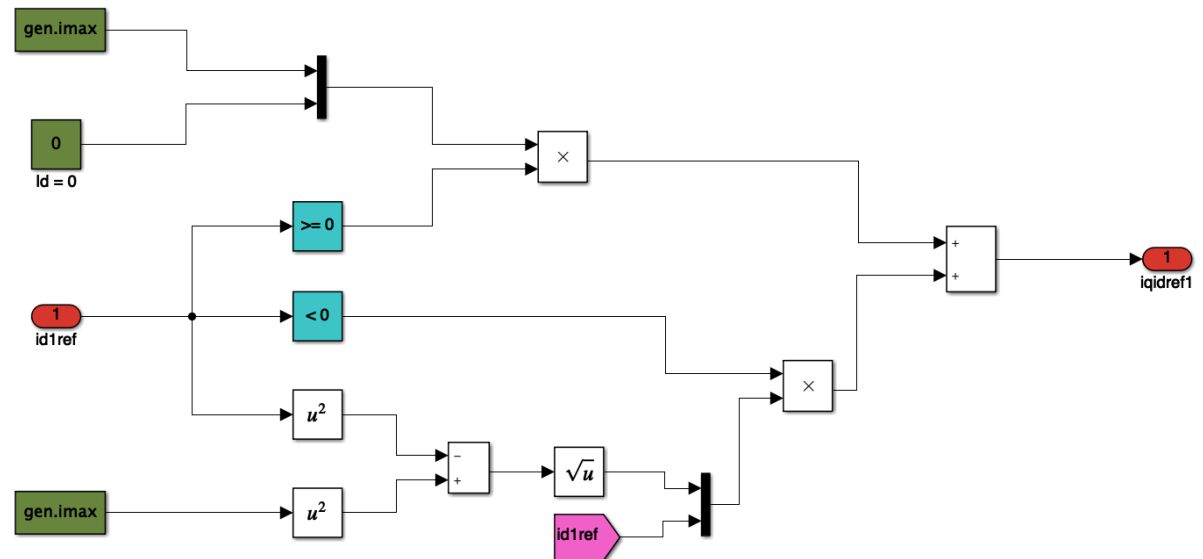
(i) Calculate upper currents2 subsystem
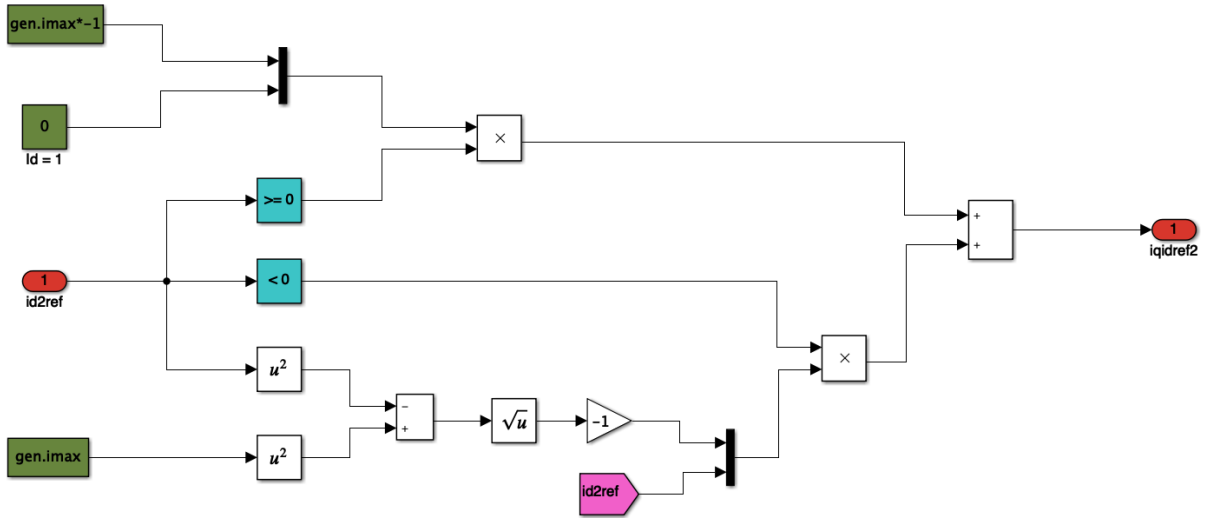
(j) Calculate upper currents1 subsystem

Figure A.3: All the subsystems making up the torque control subsystem
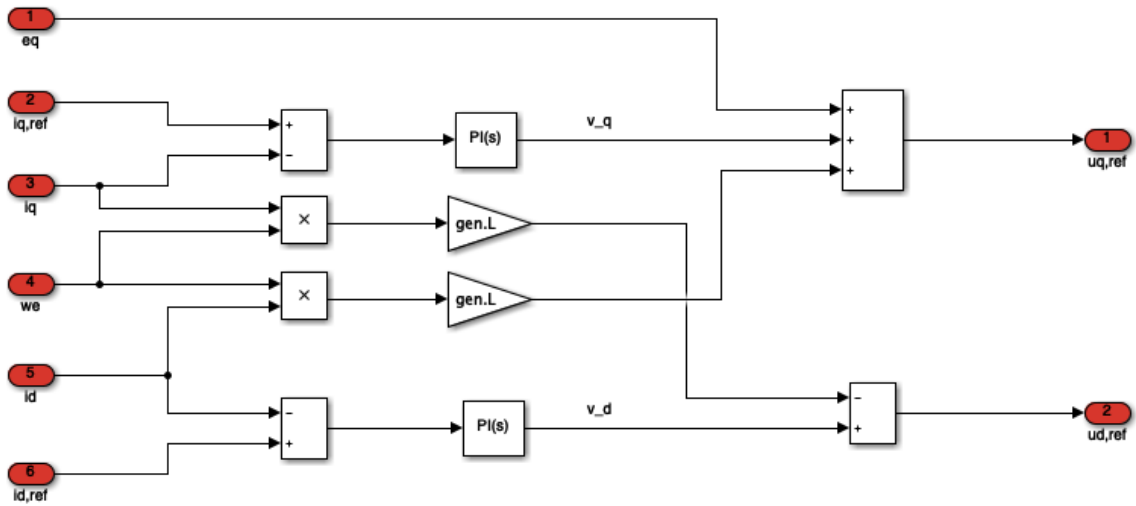
Figure A.4: Current control subsystem
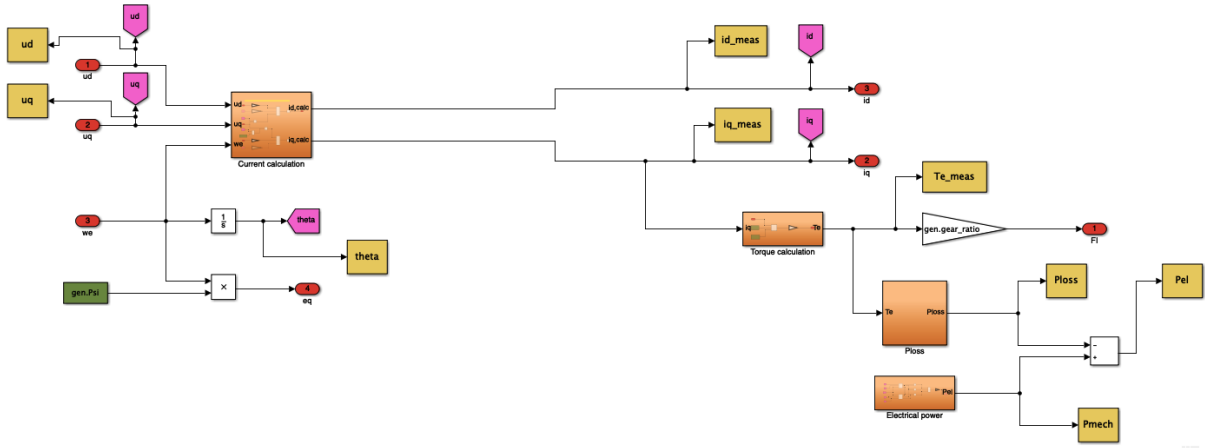
(a) PMSG subsystem
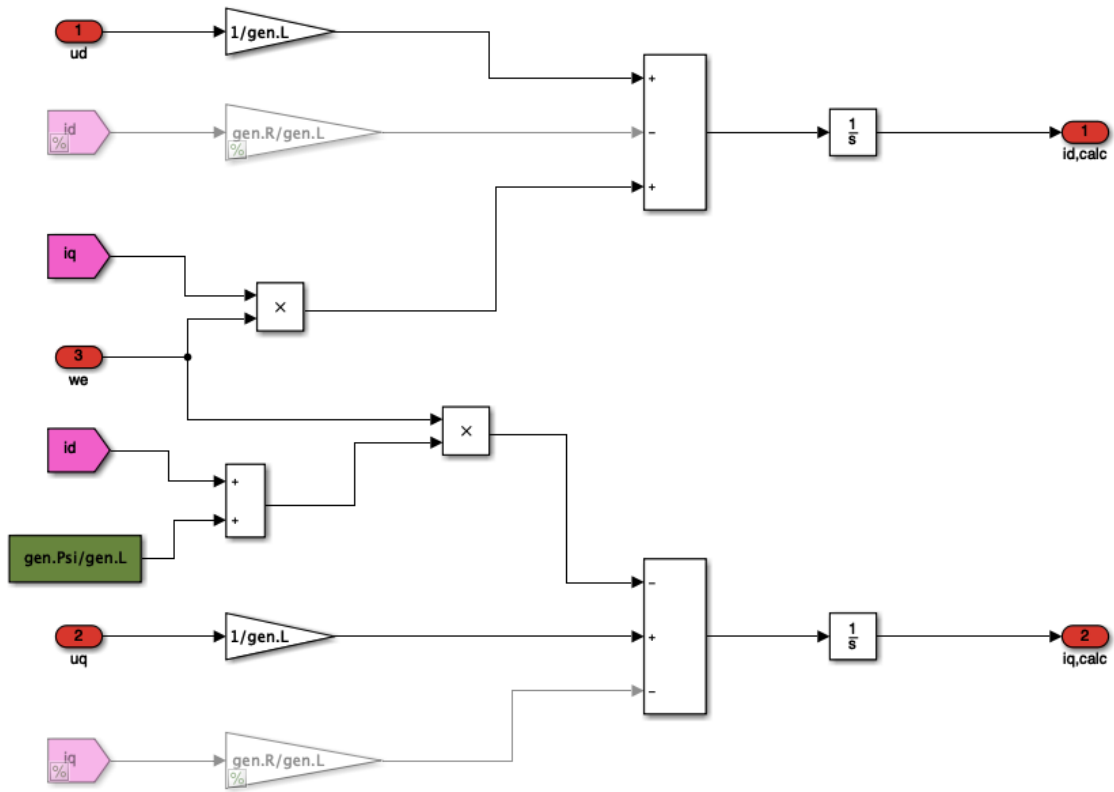
(b) Current calculation subsystem
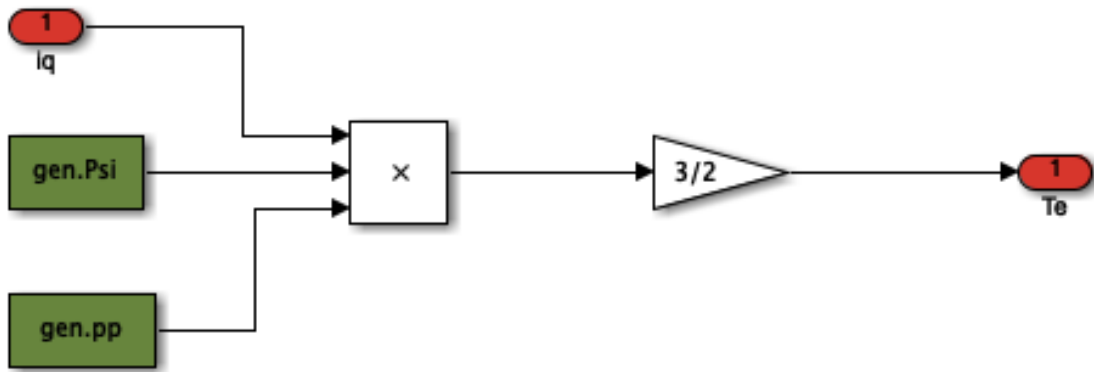
(c) Torque calculation subsystem
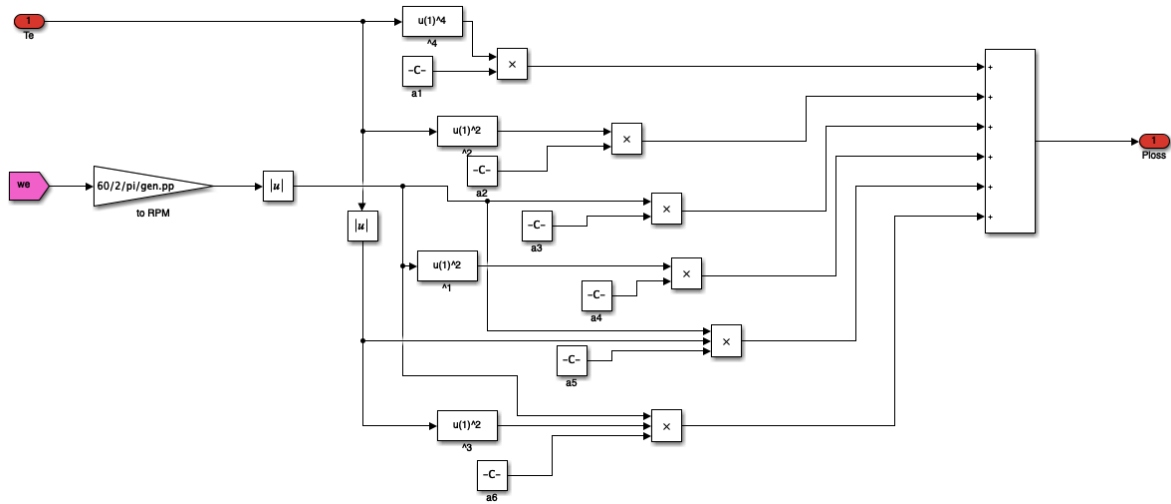
(d) Ploss subsystem
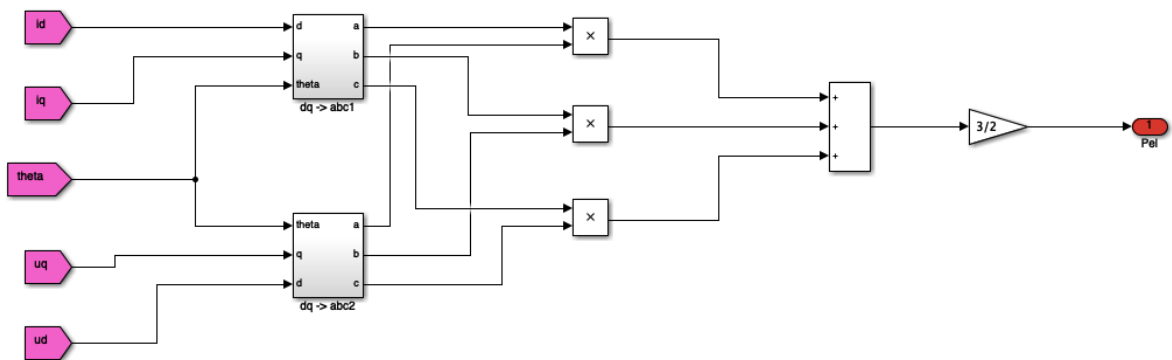
(e) Electrical power subsystem

Figure A.5: All the subsystems making up the PMSG subsystem

A.2   RENEW2020 conference paper

Effect of non-ideal power take-off on the electric output power of a wave energy converter under passive control

Martine F. Pettersen
Dept. of Electric Power Engineering, Norwegian University of Science and Technology, Trondheim, Norway

Paula B. Garcia-Rosa
SINTEF Energy Research, Trondheim, Norway

Marta Molinas
Dept. of Engineering Cybernetics, Norwegian University of Science and Technology, Trondheim, Norway

Olav B. Fosso
Dept. of Electric Power Engineering, Norwegian University of Science and Technology, Trondheim, Norway

ABSTRACT: Different control schemes have been proposed aiming to improve the energy absorption of wave energy converters (WECs) under a variety of operating conditions. The performance of most of these control strategies have been verified through the use of hydrodynamic models, assuming ideal power take-off (PTO) systems. Particularly, recent studies with a passive control (PC) scheme based on the Hilbert-Huang transform (HHT) has shown promising results for increasing the energy absorption of WECs. In this paper, the analysis of such control scheme is extended by including a fully coupled wave-to-wire model that takes into account the physical limitations and efficiency of an electrical PTO system. The effect of HHT passive control on the electric output power of the WEC is studied through numerical simulations and compared with the case when only hydrodynamic models are considered.

Keywords: wave energy, control applications, wave-to-wire model, Hilbert-Huang transform, point absorber

1 INTRODUCTION

Wave energy converters (WECs) are usually designed to match their frequency responses to the predominant wave spectrum, or sea state, of an installation site. Since real ocean waves are non-stationary by nature, and wave profiles with different spectral characteristics occur over time, control systems are employed to improve the energy conversion performance of the WEC for different sea state conditions.

In this framework, several control strategies rely on tuning the parameters of the power take-off system (PTO) to the frequency of waves, e.g., (Yavuz et al. 2007, Cargo et al. 2016). Thus, the frequency that best characterizes the incident non-stationary wave field should be determined. Recent studies have shown that tuning the PTO to time-frequency estimations obtained from the Hilbert-Huang transform (HHT) method result in greater energy absorption than tuning the PTO to a constant frequency of the wave spectrum (Garcia-Rosa et al. 2017), or to time-frequency estimations from the Extended Kalman Filter (Garcia-Rosa et al. 2019).

By assuming a generic and ideal PTO system, such studies (Garcia-Rosa et al. 2017, Garcia-Rosa et al. 2019) have focused on hydrodynamic models only, where the WEC performance under passive and reactive control is measured in terms of absorbed power and PTO rating. Non-ideal PTO systems have not yet been considered for control schemes based on HHT.

This paper aims at investigating the impact of control systems with HHT on the electric output power of a WEC. To this end, the hydrodynamic model of an oscillating body is connected to an all-electric PTO system, as the system of the wave energy converter Lifesaver (Sjolte et al. 2013). Thus, the analysis of the WEC performance under control systems using HHT is extended for a fully coupled wave-to-wire model, which includes the physical limitations and efficiency of the PTO. Sjolte et al. (2013) have shown that the electric PTO system of Lifesaver has limited potential for increased production by reactive control, because of large accumulated average losses and limited efficiency of the generator. In such a way, this paper studies how the PTO limitations will affect the power production by the HHT passive control method.

2 WAVE-TO-WIRE DYNAMIC MODELLING

The WEC considered in this paper is a single oscillating point absorber, moving only in heaving motion. The oscillating body is a vertical cylinder which is connected to an electric PTO system, as the PTO system of the wave energy converter Lifesaver (Sjolte et al. 2013).

2.1 *Time-series of the wave elevation*

A mathematical way of modelling irregular waves in the time domain is through a finite number of sinusoidal waves with different amplitudes, frequencies and phases, which is an approximation of real ocean waves. Then, the elevation of an irregular wave can be calculated as (Ricci et al. 2008)

$$\zeta(t) = \sum_{n=1}^{N} \sqrt{2S(\omega_n)(\omega_n)d\omega} \sin(\omega_n t + \phi_n), \qquad (1)$$

where ω_n and ϕ_n are the angular frequency and random phase of the n-th wave component, respectively.

When modelling wind generated waves, it is common to use an energy spectrum that characterizes the intensity of ocean waves. Various mathematical models can be used to describe the wave spectrum, here the Ochi-Hubble spectrum has been considered. It is a 6-parameter wave spectrum that is decomposed into two parts: one containing the lower frequency components of the wave energy (remotely generated swells) and the second including the higher frequency components of the energy (local wind waves) (Ochi & Hubble 1976). The spectral formulation can be expressed as

$$S(\omega) = \frac{1}{4} \sum_{j=1}^{2} \frac{\left[(\lambda_j + 0.25)\,\omega_{m_j}\right]^{\lambda_j}}{\Gamma(\lambda_j)} \frac{H_{s_j}^2}{\omega^{4\lambda_j+1}} e^{-\frac{(\lambda_j + 0.25)\,\omega_{m_j}^4}{\omega^4}}, \qquad (2)$$

where two sets of a three-parameter spectrum has been combined. Each set consists of a spectral shape parameter λ_j, a significant wave height H_{s_j} and a modal or peak frequency ω_{m_j}.

2.2 *Hydrodynamic model*

Using Newton's second law of motion and assuming linear hydrodynamic theory, the motion of the floating body can be described as

$$m\ddot{x}(t) = f_e(t) + f_r(t) + f_s(t) + f_p(t), \qquad (3)$$

where $\ddot{x}(t)$ is the body acceleration, m is the body mass, $f_e(t)$ is the excitation force, $f_r(t)$ is the radiation force, $f_s(t)$ is the hydrostatic force, and $f_p(t)$ is the machinery or PTO force.

The hydrostatic force is the resultant force between the gravitational force and the force due to buoyancy when the body moves from its equilibrium position. As a result, the hydrostatic force can be calculated as

$$f_s(t) = -Sx(t), \qquad (4)$$

where S the hydrostatic stiffness and x is the body displacement.

The excitation force is the force acting on the body as it is held fixed in incident waves. The excitation force is expressed as

$$f_e(t) = \int_{-\infty}^{\infty} h_e(t - \tau)\zeta(\tau)d\tau, \qquad (5)$$

where the inverse Fourier transform of the excitation force transfer function $H_e(\omega)$ can be found by

$$h_e(t) = \frac{1}{2\pi} \int_{-\infty}^{\infty} H_e(\omega)e^{i\omega t}d\omega. \qquad (6)$$

The radiation force is the force due to waves generated by the body motion. It can be expressed as (Cummins 1962)

$$-f_r(t) = m_r(\infty)\ddot{x} + \int_0^t h_r(t - \tau)\dot{x}(\tau)\,d\tau, \qquad (7)$$

where $m_r(\infty)$ is the added mass coefficient at infinite frequency, and the integration kernel $h_r(t - \tau)$, known as the fluid memory term (Greenhow & White 1997), is given by

$$h_r(t - \tau) = \frac{2}{\pi} \int_0^{\infty} B_r(\omega) \cos(\omega(t - \tau))d\omega, \qquad (8)$$

where B_r is the radiation damping.

The forces applied by the PTO system on the WEC, including friction, are defined as the machinery force. How the force is applied and its magnitude will influence the WEC's capability to extract power from incident waves. Here, the machinery force is defined as

$$f_p(t) = -B_p(t)\dot{x}(t), \qquad (9)$$

where $B_p \in \mathbb{R}_+$ represents the PTO damping and $\dot{x}(t)$ is the velocity of the floating body.

The mean absorbed power for a time interval T is calculated as

$$P_a(t) = -\frac{1}{T} \int_0^T f_p(t)\dot{x}(t)dt. \qquad (10)$$

2.3 *Electric PTO model*

The electric PTO system of Lifesaver generates electric power through a winch that is connected to the mooring line, as illustrated in Figure 1. In order

to maintain a continuous rope tension, the generator needs to operate as a motor whenever the device performs downward motions, and then, power flows from the grid to the WEC. The generator only produces power during the upwards motion of the device (Sjolte et al. 2013).
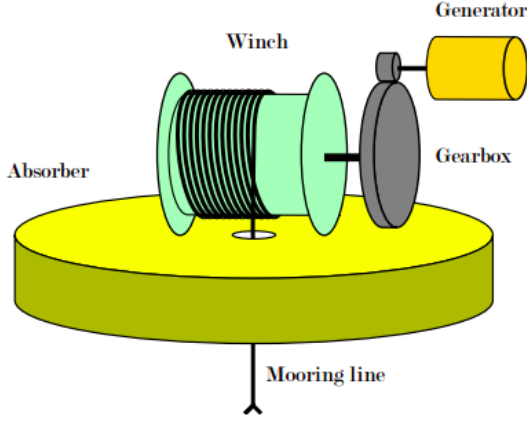

Figure 1: PTO of Lifesaver (Sjolte et al. 2013).

The stand-alone system consists of the following components: Surface-mounted permanent magnet synchronous machine (SMPMSM); inverter/rectifiers; ultra-capacitor bank; DC-link charger; battery charger; brake charger and dump resistor.

The generator used in Lifesaver is a 28-pole SMPMSM. In the synchronous reference frame, the mathematical model of a SMPMSM drive system is commonly expressed as follows (Vas 1990):

$$u_{ds} = R_s i_{ds} + \frac{d}{dt}\left(L_s i_{ds} + \Psi_{PM}\right) - \omega_r L_s i_{qs}, \quad (11)$$

$$u_{qs} = R_s i_{qs} + \frac{d}{dt}\left(L_s i_{qs}\right) - \omega_r \left(L_s i_{qs} + \Psi_{PM}\right), \quad (12)$$

where u_{ds} and u_{qs} are the stator d- and q-axis voltages, i_{ds} and i_{qs} are the stator d- and q-axis currents, R_s and L_s denote the stator resistance and inductance, and Ψ_{PM} is the permanent magnet flux linkage. The rotor angular speed of the generator ω_r is calculated from the hydrodynamic model as

$$\omega_r(t) = \frac{n_p}{2}\rho_g \dot{x}(t), \quad (13)$$

where ρ_g is the angular to gear ratio, and n_p is the number of poles of the generator.

The electromagnetic torque of the generator can be found through the permanent magnet flux linkage Ψ_{PM}, q-axis stator current i_{qs}, and number of pole pairs by

$$T_e(t) = \frac{3}{2}\frac{n_p}{2}\Psi_{PM}i_{qs}(t). \quad (14)$$

As can be seen in equation (11) and (12), a cross coupling between the d- and q-axis voltages occur.

This can be avoided by using a feed-forward technique, where the reference voltages are defined as

$$v_{ds}(t) = u_{ds}(t) + \omega_r L_s i_{qs}(t) \quad (15)$$

$$v_{qs}(t) = u_{qs}(t) - \omega_r L_s i_{ds}(t) - e_q(t), \quad (16)$$

where e_q is the induced voltage in the q-axis. Applying this to equation (11) and (12) results in two independent first-order equations in the synchronous reference frame. Then, the transfer function from the current i to the voltage v can be written as

$$\frac{i(s)}{v(s)} = \frac{\dfrac{1}{R_s}}{1 + \dfrac{L_s}{R_s}s}, \quad (17)$$

and the current controller can be implemented as illustrated in the block diagram in Figure 2.
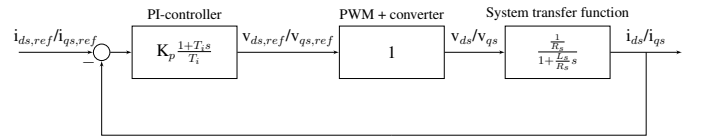
Figure 2: Block diagram of the current controller.

The transfer function for the PWM and converter is set to unity because it is assumed that the voltage from the converter follows the reference voltage perfectly. As a result, the simulation time is significantly reduced and there is no need for a filter in the system. Furthermore, the electrical time constant T_i is cancelled out and the gain K_p is found to be equal to 25. This is explained in more details in Sjolte et al. (2013).

In order to ensure that the limitations of the PTO is not exceeded, torque control is required. The reference torque is calculated using the machinery force from the hydrodynamic model as

$$T_{e,ref}(t) = \frac{1}{\rho_g}f_p(t), \quad (18)$$

where f_p is defined as in equation (9).

Then, the reference for the q-current is given by

$$i_{qs,ref}(t) = \frac{T_{e,ref}(t)}{\frac{3}{2}n_p\Psi_{PM}}. \quad (19)$$

The actual references for q- and d-axis currents used for torque control are updated according to $i_{qs,ref}$ values (19) and the generator characteristics, as summarized below (Sjolte et al. 2013):

1. If $I_{qs,min} < i_{qs,ref} < I_{qs,max}$ then $i_{qs,ref} = i_{qs,ref}$ and $i_{ds,ref} = 0$;

2. If $I_{qs,min} > i_{qs,ref}$ and $\omega_r < \omega_{rm}$ then $i_{qs,ref} = I_{qs,min}$ and $i_{ds,ref} = 0$;

3. If $i_{qs,ref} > I_{qs,max}$ and $\omega_r < \omega_{rm}$ then $i_{qs,ref} = I_{qs,max}$ and $i_{ds,ref} = 0$;

4. Otherwise, if $\omega_r > \omega_{rm}$, then field weakening is necessary.

Where $I_{qs,min}, I_{qs,max}$ are, respectively, maximum and minimum q-axis currents and ω_{rm} is the field weakening speed.

During field weakening, the d- and q-axis currents are decided through a method described by Ching-Tsai Pan and Jenn-Horng Liaw (2005). The method is based on using the current and voltage constraints of the SMPMSM drive system to calculate the real-time upper and lower q-axis current bounds. Using the generator characteristics, the field weakening speed ω_{rm} in [rad/s] can be found by

$$\omega_{rm} = \frac{-2R_s I_{max}\Psi_{PM} + \sqrt{(2R_s I_{max}\Psi_{PM})^2 - 4(\Psi_{PM}^2 + L_s^2 I_{max}^2)(R_s^2 I_{max}^2 - V_{max}^2)}}{2(\Psi_{PM}^2 + L_s^2 I_{max}^2)}$$

(20)

In terms of efficiency of the generator and converter, as described in (Sjolte et al. 2013), the detailed properties of the generator and converter are not exactly known. However, based on provided information on the efficiency at a number of operating points, a polynomial expression for the combined generator and converter losses has been determined. The function is based on the generator torque T_e and the angular speed of the rotor ω_r in rpm, and is given by (Sjolte et al. 2013):

$$|P_l| = a_1 T_e^4 + a_2 T_e^2 + a_3 |\omega_r| + a_4 \omega_r^2 +$$

$$a_5 |\omega_r T_e| + a_6 |\omega_r| T_e^2 . \quad (21)$$

3 TUNING OF THE POWER TAKE-OFF DAMPING

3.1 *Constant frequency tuning*

For passive loading (PL), the PTO damping is set to a constant value, i.e. $B_p(t) = B_p$, for any time t, where B_p can be adjusted according to a chosen tuning frequency. For an incoming regular wave (a wave consisting of only one frequency), the optimal PTO damping is calculated as (Falnes 2002)

$$B_p = \sqrt{B_r(\omega)^2 + \left[\omega(m + m_r(\omega)) - \frac{S}{\omega}\right]^2} . \quad (22)$$

A challenge with passive loading is to select the tuning frequency for real ocean waves and irregular waves as they do not consist of a single frequency in the time-domain. Commonly, the energy frequency or the peak frequency of the wave spectrum is selected as the tuning frequency. The PTO damping can

then be tuned on different time scales based on variations in the sea state (hourly basis), seasonal variations (monthly basis) or on an annual basis (Oskamp & Özkan-Haller 2012).

In any practical application studies, tuning the PTO damping to the frequency of waves will require an estimation of the frequency. In Garcia-Rosa et al. (2019), simulation studies indicate that the Extended Kalman Filter, which is a state observer commonly used in real-time applications, estimates the mean centroid frequency of the excitation force spectrum (ω_{1,f_e}). Thus, in this paper, PL uses this frequency for tuning the damping.

The mean centroid frequency (ω_1) is a statistical parameter of the wave spectrum given by the spectral moments m_1 and m_0 as $\omega_1 = m_1/m_0$. Spectral moments of order n are calculated as

$$m_n = \int_0^\infty \omega^n S(\omega) d\omega . \quad (23)$$

3.2 *Time-frequency tuning using the Hilbert-Huang Transform*

For a passive control (PC) scheme that tunes the PTO on a wave-to-wave basis, $B_p(t)$ can be calculated as

$$B_p(t) = \sqrt{B_r(\hat{\omega}_d)^2 + \left[\hat{\omega}_d(m + m_r(\hat{\omega}_d)) - \frac{S}{\hat{\omega}_d}\right]^2} ,$$

(24)

where $\hat{\omega}_d(t)$ is the estimated time-domain frequency of the wave excitation force. The reason the excitation force is used rather than the wave elevation is because, in this way, some of the high frequency content of the wave elevation is filtered by $H_e(\omega)$. As in Garcia-Rosa et al. (2017), the frequency in this paper is estimated by the Hilbert-Huang Transform (HHT).

HHT is a two-step method for analyzing nonstationary and nonlinear signals. Firstly, the Empirical Mode Decomposition (EMD) is used to decompose the original signal into Intrinsic Mode Functions (IMFs). Secondly, the Hilbert Transform (HT) is used on each IMF component to estimate the instantaneous frequency and amplitude (Huang et al. 1998).

The EMD is applied to the excitation force $f_e(t)$ and empirically identifies the different frequencies of the signal through the process of sifting. The process is explained in the following algorithm:

0. Set $i = 1$ and $r(t) = f_e(t)$;

1. Identify all the local maxima and minima in $r(t)$;

2. Create upper and lower envelopes defined from the corresponding maxima and minima using cubic spline interpolation;

3. Calculate the mean of the envelopes $m(t)$;

4. Subtract the mean from the signal, $h(t) = r(t) - m(t)$;

5. If $h(t)$ can be classified as an IMF, go to the next step. Otherwise, set $r(t) = h(t)$ and repeat the process from 1;

6. Set $c_i(t) = r(t)$. Calculate $r(t) = r(t) - c_i(t)$, set $i = 2, ..., N$ and repeat the process from 1. Define the IMF components as $c_1(t), ..., c_N(t)$ and the residue as $r(t)$.

After the EMD has been completed, the IMF components are given in a sequential order from the highest frequency component to the lowest. Next, the amount of energy in each IMF component are calculated in order to locate the IMF component with the highest energy content (Garcia-Rosa et al. 2017),

$$E_{c_i} = \int_0^T | c_i(t) |^2 \, dt, \qquad (25)$$

where $c_i(t)$ is the i-th IMF component. The IMF component with the highest energy content is referred to as the dominant IMF component $c_d(t)$.

Finally, the HT is applied to the dominant IMF component,

$$v_d(t) = \frac{1}{\pi} P \left\{ \int_{-\infty}^{\infty} \frac{c_d(\tau)}{t - \tau} d\tau \right\}, \qquad (26)$$

where P is the Cauchy principal value. Then, the dominant IMF component can be expressed as an analytical signal,

$$z_d(t) = c_d(t) + jv_d(t) = \hat{a}_d(t)e^{j \int \hat{\omega}_d(t)dt}, \qquad (27)$$

where $\hat{a}_d(t)$ is the instantaneous amplitude,

$$\hat{a}_d(t) = \sqrt{c_d^2(t) + v_d^2(t)}, \qquad (28)$$

and $\hat{\omega}_d(t)$ is the instantaneous frequency, calculated as

$$\hat{\omega}_d(t) = \frac{d}{dt} \arctan \left(\frac{v_d(t)}{c_d(t)} \right). \qquad (29)$$

The instantaneous frequency is then used as the tuning frequency for the PTO damping calculation (24).

4 NUMERICAL SIMULATIONS

In order to evaluate the effect of HHT passive control on a non-ideal PTO, we consider a comparison of the electric output power for the cases when the PTO damping is tuned to

- a constant frequency of the excitation force spectrum, ω_{1,f_e}, referred as PL approach;

- frequency estimated by HHT, $\hat{\omega}_d(t)$, referred as PC approach.

Firstly, a comparison of the results considering only the hydrodynamic model is performed. In this case, an ideal PTO system is assumed, and the mean absorbed power $\bar{P}_a$ is the output power.

4.1 Simulation Parameters

Ochi-Hubble spectra (2) are generated from the real data of the Belmullet wave energy test site used in (Garcia-Rosa, Kulia, Ringwood, & Molinas 2017). The spectral shape parameters $(\lambda_1, \lambda_2, H_{s_1}, H_{s_2}, \omega_{m_1}, \omega_{m_2})$ are set to mimic three sea states from that paper: S1, S2, and S6 (which is renamed as S3 here). The simulation interval is $T = 30$ min with sampling frequency of 1.28 Hz.

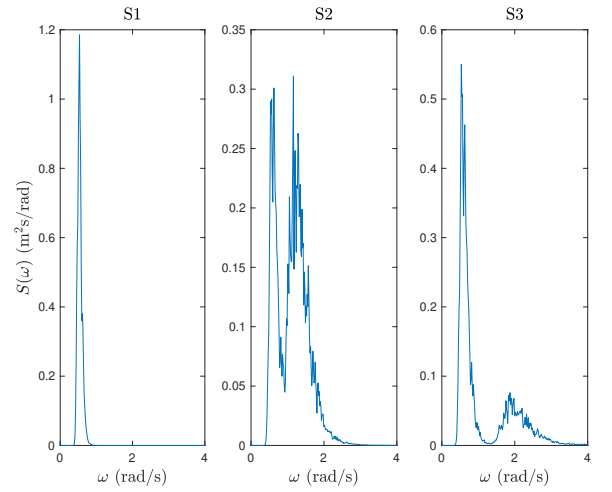Figure 3: Simulated wave spectra S1, S2 and S3.

The spectral density of the excitation force for the given sea states are shown in Figure 4. Comparing the wave spectra and the excitation force spectra, it can be seen that some of the higher frequencies in the wave spectra have been filtered out by $H_e(\omega)$.
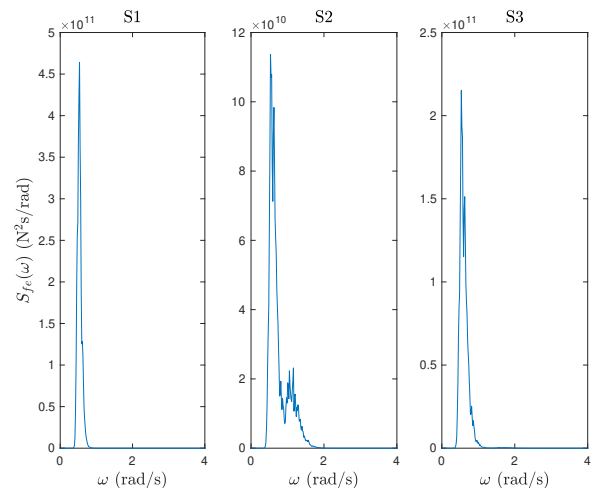

Figure 4: Spectral density of the excitation force for sea states S1, S2 and S3.

The heaving cylinder used in Garcia-Rosa et al. (2017) is also considered here. The main specifications of the electric PTO system are listed in Table 1, and the generator characteristics are shown in Table 2 (Sjolte et al. 2013).

Table 1: Main PTO specifications

Property	Value
DC-bus voltage, V_{max}	600 V
DC-bus current, I_{max}	481.2679 A
Angular to linear gear ratio, ρ_g	38.5 1/m
PTO maximum force	100 kN
PTO minimum force	10 kN

Table 2: Generator characteristics

Property	Value
Number of poles, n_p	28
Stator resistance, R_s	0.038 Ω
Stator inductance, L_s	1.4 mH
Permanent magnet flux linkage, Ψ_{PM}	0.257 Wb
Maximum q-current, $I_{qs,max}$	481.2679 A
Minimum q-current, $I_{qs,min}$	48.1268 A
Field weakening speed, ω_{rm}	561.1284 rpm

4.2 Hydrodynamic model

When running the hydrodynamic model only, the ratio between $\bar{P}_a$ with PC and $\bar{P}_a$ with PL becomes as shown in Table 3.

Table 3: Ratios between $\bar{P}_a(PC)$ and $\bar{P}_a(PL)$.

Ratio	S1	S2	S3
$P_a(PC)/P_a(PL)$	1.01	1.32	1.03

For all sea states, the output power is higher for PC than for PL tuned with ω_{1,f_e}, where the advantage of using PC and HHT frequency estimation is more evident for S2, a sea state with mixed waves spread over a wide band of frequencies. These results agree with previous results shown in Garcia-Rosa et al. (2017).

4.3 Wave-to-wire model

To verify the effect of the control methods on the electric output power, the average powers are split into positive and negative components, following the downward and upward motions of the body. Figure 5 shows the average electrical power and losses obtained with PL and PC for sea states S1, S2 and S3 over the 30-min simulation interval, while Table 4 shows the ratios between PC and PL powers.
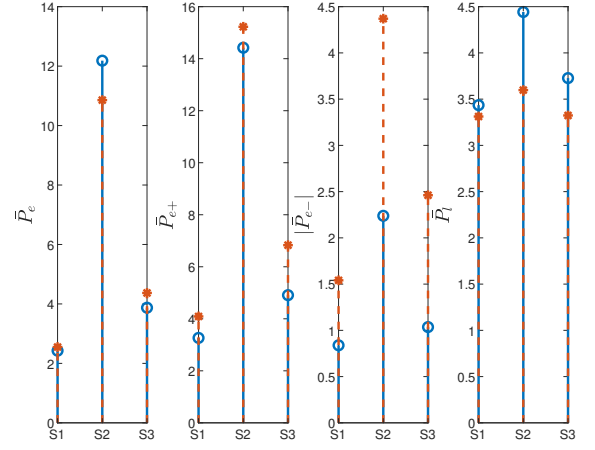

Figure 5: Average electrical power and average power losses (in kW) for PL (blue lines with circles) and PC (red dashed lines with stars).

Table 4: Ratios between average electric powers with PC and with PL, and ratios between power losses with PC and with PL.

Ratio	S1	S2	S3
$\bar{P}_e(PC)/\bar{P}_e(PL)$	1.05	0.89	1.13
$\bar{P}_{e+}(PC)/\bar{P}_{e+}(PL)$	1.25	1.06	1.39
$\bar{P}_{e-}(PC)/\bar{P}_{e-}(PL)$	1.83	1.95	2.38
$\bar{P}_l(PC)/\bar{P}_l(PL)$	0.96	0.81	0.89

Comparing the ratio for negative power in Table 4, it can be seen that using PC as the control method results in around twice as much negative power than for PL with ω_{1,f_e}, which means that more power flowing from the grid to the WEC would be required. At the same time, PC gives more positive electrical power than PL, and then, the power production is higher. The total electrical power output becomes almost the same, as shown in Figure 5 (at the left).

When comparing the simulation results of the wave-to-wire model, which includes a non-ideal PTO system, with the hydrodynamic model results, which assumes an ideal PTO, it can be seen that the pattern related to improvements of HHT over PL for wide-band spectra is not observed anymore.

As seen in Table 4, using PL with ω_{1,f_e} results in more power losses than using PC with HHT estimates. The power loss is found as shown in equation (21) and depends both on the generator speed ω_r and generator torque T_e. Since the torque values are raised to the fourth power, the losses are higher for cases with higher torques.

Furthermore, the losses are only calculated on the basis of the copper losses, but in a SMPMSM machine, iron losses is a significant fraction of the total losses (Meier 2002). It is also important to remember that a generator is designed to work in a very stationary mode with small variations. When passive control is applied to modify the damping on a wave-to-wave basis, the generator is forced to constantly change,

making it work in a way it has not been designed for. This may result in other losses related to wear and tear, and hence more maintenance might be required over time.

Figures 6-9 show samples of time-series simulation of the generator speed, torque, and electric currents for both PL and PC. The generator speed is shown in Figure 6 and the generator torque is plotted in Figure 7. The generator speed is very similar for PL and PC, while the generator torque exhibits different behaviour. For both control methods, the generator torque is very often at its maximum value, but when tuning the damping with ω_{1,f_e} the torque is more often at its maximum value than for tuning with HHT frequencies. This difference can especially be seen for sea state S3. The high torque values are related to the energy content of the sea state. Sea states with very high energy content results in a higher reference torque, as indicated by (18). As a result, the electric PTO system works on the limit of its capacity over a long period of time.

As indicated by equation (19), the q-axis current (i_{qs}) is proportional to the generator torque, and then, high torque references result in high current references. From Figures 8b and 9b, the same behavior observed for the generator torque can be seen for the i_{qs} current. It can also be noticed from Figures 8a and 9a that S2 is the only sea state that results in field weakening. Physically, a higher i_{qs} will also result in higher copper losses due to the increased stator current. This can be clearly seen in the power losses.

5 CONCLUSION

By assuming an ideal PTO, the greatest improvements of the HHT over constant damping are obtained for wideband spectra. However, many nonlinearities are added when the model of an electric PTO is included. For instance, for the two-peak wideband spectrum considered here, the field weakening region of the generator is activated, and then, the benefit of using a time-varying damping is reduced. Furthermore, even though HHT results in more electrical power than PL, it also requires more power from the grid in order to operate correctly, as the PTO requires the generator to operate as a motor during downwards motion of the WEC.

Simulation results with the wave-to-wire model showed that higher losses are obtained with PL (tuned at the mean centroid frequency of the excitation force spectrum) than with PC (tuned with HHT). In contrast to PL where the PTO damping is kept fixed throughout the simulation interval, the PTO damping of PC varies on a wave-by-wave basis, and the generator torque is less often constrained. Higher losses are derived from higher generator torques, and hence, higher stator currents. In the wave-to-wire model, the power losses are only found through the stator copper losses, even though the iron losses are also significant
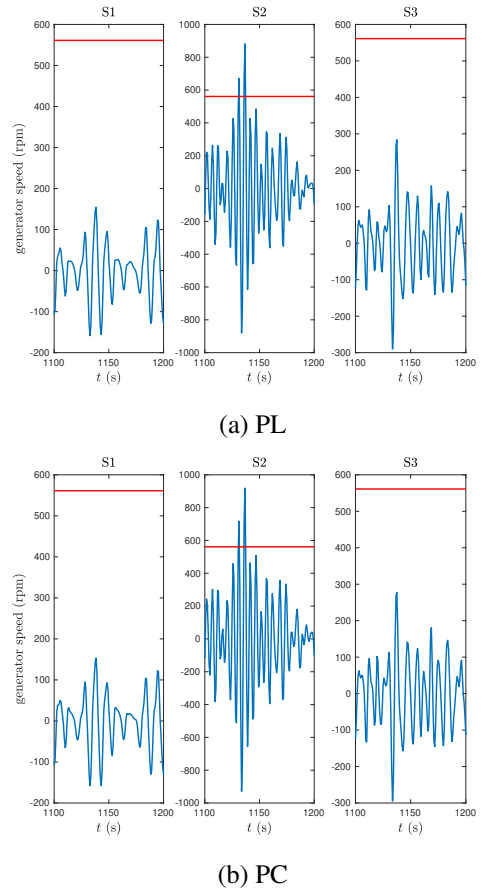

Figure 6: Time-series of generator speed for interval between 1100 s and 1200 s: (a) PL (b) PC. (Red line: field weakening speed).
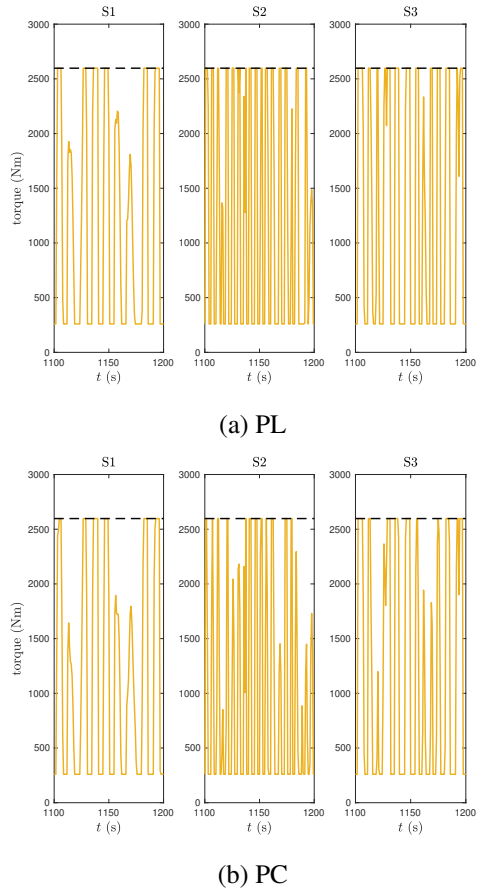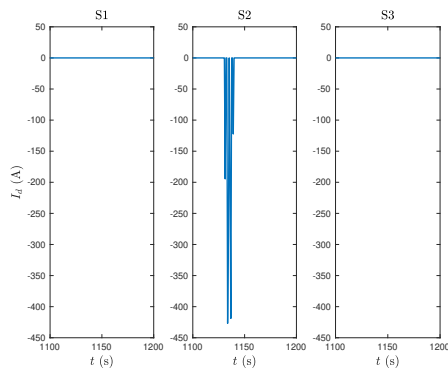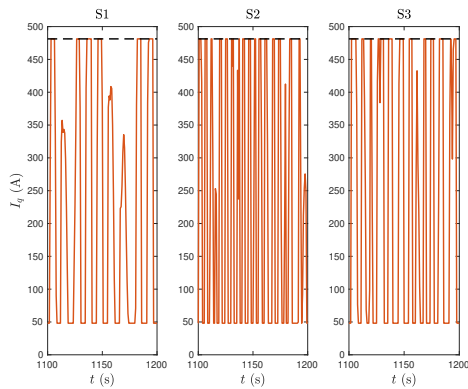

Figure 7: Time-series of generator torque for interval between 1100 s and 1200 s: (a) PL (b) PC.

(a) d-axis current

(b) q-axis current

Figure 8: Time-series of stator currents for interval between 1100 s and 1200 s when PL is applied; (a) d-axis current (b) q-axis current.
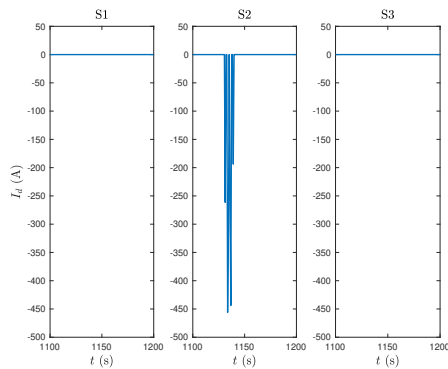

(a) d-axis current
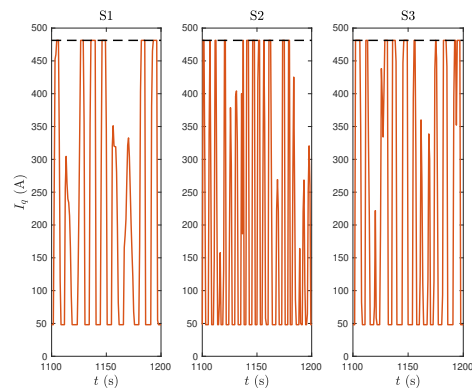

(b) q-axis current

Figure 9: Time-series of stator currents for interval between 1100 s and 1200 s when PC is applied: (a) d-axis current (b) q-axis current.

in a SMPMSM machine. By including the iron losses in the model, different results and a more clear picture on the total power losses related to each control method could be obtained.

Simulation results also showed that the electric PTO system operates at the boundary of its capacity over longer period of times for both control methods, which could result in other losses related to wear and tear over time.

REFERENCES

Cargo, C. J., A. J. Hillis, & A. R. Plummer (2016). Strategies for active tuning of wave energy converter hydraulic power take-off mechanisms. *Renewable Energy 94*, 32–47.

Ching-Tsai Pan & Jenn-Horng Liaw (2005). A robust field-weakening control strategy for surface-mounted permanent-magnet motor drives. *IEEE Transactions on Energy Conversion 20*(4), 701–709.

Cummins, W. E. (1962). The impulse response function and ship motions. *Schiffstechnik 47*(9), 101–109.

Falnes, J. (2002). *Ocean Waves and Oscillating Systems: Linear Interaction including Wave-Energy Extraction.* Cambridge University Press.

Garcia-Rosa, P. B., G. Kulia, J. V. Ringwood, & M. Molinas (2017). Real-time passive control of wave energy converters using the hilbert-huang transform. In *IFAC-PapersOnLine Volume 50(1), Proc. of the 20th IFAC World Congress*, pp. 14705–14710.

Garcia-Rosa, P. B., J. V. Ringwood, O. B. Fosso, & M. Molinas (2019). The impact of time–frequency estimation methods on the performance of wave energy converters under passive and reactive control. *IEEE Trans. on Sustainable Energy 10*(4), 1784–1792.

Greenhow, M. & S. P. White (1997). Optimal heave motion of some axisymmetric wave energy devices in sinusoidal waves. *Applied Ocean Research 19*(3), 141–159.

Huang, N. E., Z. Shen, S. R. Long, M. C. Wu, H. H. Shih, Q. Zheng, N.-C. Yen, C. C. Tung, & H. H. Liu (1998). The empirical mode decomposition and the Hilbert spectrum for nonlinear and non-stationary time series analysis. *Proc. Royal Society London 454*, 903–995.

Meier, S. (2002). Theoretical design of surface-mounted permanent magnet motors with field weakening capability. Master's thesis, Royal Institute of Technology.

Ochi, M. K. & E. N. Hubble (1976). Six-parameter wave spectra. In *Coastal Engineering 1976*, pp. 301–328.

Oskamp, J. A. & H. T. Özkan-Haller (2012, 09). Power calculations for a passively tuned point absorber wave energy converter on the oregon coast. *Renewable Energy 45*, 72–77.

Ricci, P., J.-B. Saulnier, A. Falcao, & M. Pontes (2008, 01). Time-domain models and wave energy converters performance assessment. In *Proceedings of the International Conference on Offshore Mechanics and Arctic Engineering - OMAE*, Volume 6.

Sjolte, J., C. Sandvik, E. Tedeschi, & M. Molinas (2013, 07). Exploring the potential for increased production from the wave energy converter lifesaver by reactive control. *Energies 6*, 3706–3733.

Vas, P. (1990). *Vector control of AC machines*, Volume 22 of *Monographs in electrical and electronic engineering*. Oxford: Clarendon Press.

Yavuz, H., T. J. Stallard, A. P. McCabe, & G. A. Aggidis (2007). Time series analysis-based adaptive tuning techniques for a heaving wave energy converter in irregular seas. *Proc. of the Inst. of Mech. Engineers, Part A: Journal of Power and Energy 221*(1), 77–90.

Martine Furnes Pettersen

NTNU

Norwegian University of
Science and Technology